

Linn Døvre

# Study on the long-term stability issues of the headrace tunnel of Ulset Hydropower Project

Master's thesis in Geotechnology  
Supervisor: Krishna Kanta Panthi  
June 2019







Linn Døvle

# Study on the long-term stability issues of the headrace tunnel of Ulset Hydropower Project



Master's thesis in Geotechnology  
Supervisor: Krishna Kanta Panthi  
June 2019

Norwegian University of Science and Technology  
Faculty of Engineering  
Department of Geoscience and Petroleum

 **NTNU**  
Norwegian University of  
Science and Technology





Your ref.: MS/N34T49/IGP/LDKKP

Date: 10.01.2019

**TGB4930 INGGEOL/BERGMEK - MSc thesis**

**for**

**Eng. geo. student Linn Døyle**

## **Study on the long-term stability issues of the headrace tunnel of Ulset Hydropower Project**

### **Background**

The candidate has written project work on engineering geological condition along the headrace tunnel of Ulset Hydropower Project. The project is located at Rennebu commune of Sør-Trøndelag region and is one of five projects developed by KVO (Kraftverkene i Orkla). The Ulset project is operated by Trønder Energi Kraft where water from Ya River and Falningsjø is utilized. The project consists of two regulated reservoirs (Falningsjø and Sverjesjø) and has a gross head of 320m. The 7km diversion tunnel brings water from Ya River to the Falningsjø reservoir and 8 km long headrace tunnel connects Falningsjø with the underground power plant. The project produces 135 GWh electrical energy annually. After many years of operation, an inspection along approximately 8 km headrace tunnel excavated by both D&B and TBM was carried by the main supervisor in 2017. It was observed during inspection that there are many block falls of small to medium scales at many locations of the inspected part of the headrace tunnel.

### **MSc thesis task**

During project work candidate has carried out fieldwork, mapped surface geology, collected data and information from the project and carried out laboratory investigations. With this solid base and additional information that will be available from the project, the candidate will focus her MSc thesis with following tasks:

- Literature review on the engineering geological and mechanical properties of the rock mass and instability assessment methodologies of tunnels and underground caverns.
- Theoretical review on the Norwegian design principles for unlined waterway systems.
- Discuss engineering geological and registered instability conditions along the headrace tunnel alignment.

- Systematise failures in different categories.
- Carry out stability assessment of different instabilities identified using both analytical and numerical modelling.
- Discuss the findings of stability assessment and highlight on the long-term instability issues of the headrace tunnel of Ulset hydropower project.
- Conclude the work with recommendations.

### **Relevant computer software packages**

Candidate shall use *roc-science package* and other relevant computer software for the master study.

### **Background information for the study**

- Relevant information about the project such as reports, maps, information and data received from the supervisors and collected by the candidate.
- The information provided by the professor about rock engineering and hydropower.
- Scientific papers and books related to international tunnelling cases.
- Literatures in rock engineering, rock support principles, rock mechanics and tunnelling.

### **Cooperating partner**

PhD Fellow Mr. Bibek Neupane will be the co-supervisor of this MSc thesis.

The project work is to start on January 10, 2019 and to be completed by June 11, 2019.

The Norwegian University of Science and Technology (NTNU)  
Department of Geoscience and Petroleum

January 10, 2019



Dr. Krishna K. Panthi  
Professor of geological engineering, main supervisor

---

# Abstract

The Norwegian hydropower industry is a result of over 100 years of experience in the development of design and construction of hydropower projects. The experience has resulted in a Norwegian speciality, the unlined high pressure tunnels and shafts. Unlined water tunnels have been possible due to a support philosophy which allows some rock fall during the operation time of the hydropower plant. Support is only applied in areas with very poor rock conditions.

A de-regulation of the power market in 1991 caused a change in the production scheme, from supply to demand driven, of some hydropower plants. The change results in higher frequencies of start-and-stop cycles of the turbines, which initiates pressure fluctuations along the tunnel system. This production pattern has been implemented at Ulset Hydropower Project, where an inspection in 2017 revealed various instability issues along the headrace tunnel. An assessment of the long-term stability of the tunnel has been carried out in this thesis. The focus has been on how water and pressure fluctuations, due to mass oscillations, impact the stability of the headrace tunnel.

Engineering geological conditions and instability issues along the headrace tunnel were studied through literature, tunnel inspection reports, field mapping and laboratory work during the Project work of fall 2018. This data together with new information were in this thesis used to identify the instabilities and failures experienced at Ulset, which were systematised into four categories. The categories are spalling, stress induced rock fall, structurally controlled rock fall and weakness zones. The major contributors to the rock falls are high horizontal stresses which are parallel to the foliation of a highly anisotropic quartzitic schist. The structurally controlled rock falls are restricted to the D&B part of the tunnel system.

Back analysis of the failures have been carried out. Spalling potential and depth have been evaluated through empirical methods. Assessment of block and wedge falls have been conducted with limit equilibrium analysis and the Rocscience software Unwedge. The stress induced rock falls are examined through numerical modelling in RS<sup>2</sup>. The worst case pressure increase due to mass oscillations have been calculated and incorporated in the analyses.

A timeline of the failures has been made, which reveals an increase in the number and size of rock falls in the headrace tunnel after the de-regulation of the power market. This trend suggests that the pressure fluctuations, due to mass oscillations, may have had and still have an impact on the long-term stability of the tunnel. However, the effect of pressure fluctuations is not well studied, and further research is necessary to understand the interaction between pressure fluctuations and the rock mass.

---

---

# Sammendrag

Den norske vannkraftindustrien er et resultat av over hundre år med erfaring fra utvikling av design og bygging av vannkraftprosjekter. Erfaringene har resultert i en norsk spesialitet, uførete trykktunneler og -sjakter. Uførete trykktunneler og -sjakter kommer av en sikringsfilosofi som godtar noe nedfall gjennom driftstiden til kraftverket. Sikring er bare installert i områder med ekstremt dårlig bergmassekvalitet.

En deregulering av energimarkedet i 1991 førte til en forandring av produksjonsmønsteret, fra kontinuerlig produksjon til effektivkjøring, av noen vannkraftverk. Denne forandringen gir opphav til en økning i antall start-og-stopp sekvenser av turbinene, som setter igang trykksvingninger langs tunnelsystemet. Det nye produksjonsmønsteret har blitt implementert hos Ulset Kraftverk, hvor en inspeksjon i 2017 avslørte mange ustabiliteter langs tilløpstunnelen. En vurdering av langtidsstabiliteten til tunnelen har derfor blitt gjennomført i denne oppgaven. Fokuset har vært på vann og trykksvingningers påvirkning på stabiliteten til tilløpstunnelen.

Ingeniørgeologiske forhold og ustabiliteter langs tilløpstunnelen har blitt studert gjennom litteratur, tunnelbefaringsrapporter, felttur og laboratorieundersøkelser i prosjektarbeidet gjennomført høsten 2018. Disse dataene, sammen med ny informasjon har blitt brukt i denne avhandlingen for å identifisere ustabilitetene i tilløpstunnelen til Ulset Kraftverk og systemisere disse i fire kategorier. Disse kategoriene er avskalling/sprak (spalling), nedfall pga. høye spenninger (stress induced rock fall), nedfall pga. strukturer (structurally controlled rock fall) og svakhetssoner. Hovedårsaken til mye av nedfallet i tunnelen er høye horisontalspenninger som virker parallellt med foliasjonen til en meget anisotropisk kvartsitisk skifer. Det struktur-genererte nedfallet er begrenset til den sprengte delen av tilløpstunnelen.

Stabilitetsvurdering av ustabilitetene har blitt utført. Potensialet for spraking og dens dybde har blitt evaluert gjennom empiriske metoder. Bedømmelse av sprekkeavløste blokker og kiler har blitt utført med likevektsberegninger og med programvaren Unwedge fra Rocscience. Spenningsrelaterte nedfall har blitt undersøkt gjennom numerisk modellering i  $RS^2$ . Den største teoretiske trykkøkningen fra massesvingninger er beregnet og inkorporert i analysen.

Det er laget en tidslinje over bruddene som har oppstått i tunnelen. Den avslørte at det har vært en økning i antall og størrelse av nedfall etter dereguleringen av energimarkedet. Denne trenden antyder at massesvingningene kan ha og fortsatt har innvirkning på langtidsstabiliteten til tunnelen. Denne påvirkningen er derimot ikke godt nok undersøkt, og videre forskning kreves for å forstå interaksjonen mellom trykksvingningene og bergmassen.

---



---

# Preface

This paper concludes the final work of a Master of Science degree in Geotechnology – Engineering Geology and Rock Mechanics. The thesis work started in January 2019 and was completed by June 2019. It is submitted to the Department of Geosciences and Petroleum at the Norwegian University of Science and Technology (NTNU).

The Master thesis is a continuation of the Project work "Engineering geological conditions along the headrace tunnel of Ulset HPP" conducted during the fall of 2018. The objective of the Project work was to gather information of Ulset HPP and the engineering geological conditions along the headrace tunnel. Chapter 2, 6 and 7 are as a result largely based on the findings from the Project work.

The main supervisor for the thesis has been Professor Dr. Krishna Kanta Panthi and PhD fellow Mr. Bibek Neupane has acted as the co-supervisor. I am very grateful for the advice and help I have been given through this work, and for the possibility to take on such an interesting and challenging assignment.

I would also like to thank Gunnar Vistnes and Laurentius Tjihuis for their help with laboratory testing. And Tor Harald Landløpet at Trønderenergi Kraft AS for inviting me to Berkåk, and helping me search through the old archives for information about Ulset HPP.

Finally I would like to thank my fellow graduates for making this year's study hall hours fun and unforgettable.

Trondheim 10.06.2019

Linn Døvle

---

# Table of Contents

|   |            |
|---|------------|
| <b>Abstract</b>   | <b>iii</b> |
| <b>Sammendrag</b>                                       | <b>v</b>   |
| <b>Preface</b>  | <b>vii</b> |
| <b>Table of Contents</b>                                | <b>xii</b> |
| <b>1 Introduction</b>                                   | <b>1</b>   |
| 1.1 Background of study . . . . .                       | 1          |
| 1.2 Scope of study . . . . .                            | 2          |
| 1.3 Methodology . . . . .                               | 2          |
| 1.4 Limitations . . . . .                               | 3          |
| <b>2 Norwegian Hydropower - An underground industry</b> | <b>5</b>   |
| 2.1 Introduction . . . . .                              | 5          |
| 2.2 Development of layout . . . . .                     | 6          |
| 2.3 Evolution of design criteria . . . . .              | 7          |
| 2.3.1 Criteria of confinement . . . . .                 | 7          |
| 2.3.2 Geological conditions in Norway . . . . .         | 9          |
| <b>3 Rock and Rock mass properties</b>                  | <b>11</b>  |
| 3.1 Discontinuities . . . . .                           | 11         |
| 3.1.1 Joints . . . . .                                  | 11         |
| 3.1.2 Shear strength of joints . . . . .                | 14         |
| 3.1.3 Faults and weakness zones . . . . .               | 14         |
| 3.2 Rock mass strength and deformability . . . . .      | 16         |
| 3.2.1 Intact rock strength . . . . .                    | 16         |
| 3.2.2 Rock mass strength . . . . .                      | 20         |
| 3.2.3 Rock mass deformability . . . . .                 | 21         |
| 3.2.4 Failure criteria . . . . .                        | 22         |

---

|          |  |           |
|----------|--|-----------|
| <b>4</b> | <b>Stability of tunnels</b>                              | <b>25</b> |
| 4.1      | Rock stresses . . . . .                                  | 25        |
| 4.1.1    | Redistribution of stresses . . . . .                     | 27        |
| 4.2      | Excavation method . . . . .                              | 28        |
| 4.3      | Stability issues . . . . .                               | 29        |
| 4.3.1    | Structurally controlled failure . . . . .                | 29        |
| 4.3.2    | Stress induced failure . . . . .                         | 30        |
| 4.4      | Classification methods . . . . .                         | 32        |
| 4.4.1    | Q-system . . . . .                                       | 32        |
| 4.4.2    | GSI . . . . .  | 32        |
| <b>5</b> | <b>The impact of water</b>                               | <b>35</b> |
| 5.1      | Watering and dewatering . . . . .                        | 35        |
| 5.2      | Hydraulic transients . . . . .                           | 36        |
| 5.2.1    | Water hammer and mass oscillations . . . . .             | 36        |
| 5.2.2    | The impact of hydraulic transients . . . . .             | 37        |
| 5.2.3    | Mass oscillations at Ulset HPP . . . . .                 | 37        |
| 5.3      | Rendalen and Svandalsflona HPPs - Case studies . . . . . | 40        |
| 5.3.1    | Rendalen Hydropower Project . . . . .                    | 40        |
| 5.3.2    | Svandalsflona Hydropower Project . . . . .               | 42        |
| 5.3.3    | Lessons learned from case studies . . . . .              | 44        |
| <b>6</b> | <b>Ulset Hydropower Project</b>                          | <b>45</b> |
| 6.1      | Project description and layout . . . . .                 | 45        |
| 6.1.1    | Falningsjøen and Sverjesjøen - Intake areas . . . . .    | 46        |
| 6.1.2    | Headrace tunnel . . . . .                                | 47        |
| 6.2      | Engineering geological setting . . . . .                 | 47        |
| 6.2.1    | Geology of project . . . . .                             | 47        |
| 6.2.2    | Jointing . . . . .                                       | 50        |
| 6.2.3    | Rock mass conditions . . . . .                           | 53        |
| 6.2.4    | In situ rock stress conditions . . . . .                 | 53        |
| 6.2.5    | Installed support . . . . .                              | 55        |
| 6.3      | Instabilities along the headrace tunnel . . . . .        | 55        |
| 6.3.1    | Timeline . . . . .                                       | 55        |
| 6.3.2    | Spalling . . . . .                                       | 56        |
| 6.3.3    | Stress induced failure . . . . .                         | 56        |
| 6.3.4    | Structurally controlled failure . . . . .                | 58        |
| 6.3.5    | Weakness zone . . . . .                                  | 58        |
| <b>7</b> | <b>Laboratory Work</b>                                   | <b>61</b> |
| 7.1      | Rock samples . . . . .                                   | 61        |
| 7.2      | Density and velocity . . . . .                           | 62        |
| 7.3      | Uniaxial compression test . . . . .                      | 62        |
| 7.4      | Point load index test . . . . .                          | 63        |
| 7.5      | Brazilian test . . . . .                                 | 64        |
| 7.6      | Tilt test . . . . .                                      | 65        |

---

---

|           |   |            |
|-----------|---|------------|
| 7.7       | XRD . . . . .   | 67         |
| <b>8</b>  | <b>Instability assessment methodologies</b>             | <b>69</b>  |
| 8.1       | Empirical methods . . . . .                             | 69         |
| 8.1.1     | Q-system approach . . . . .                             | 69         |
| 8.1.2     | Potential for rock spalling . . . . .                   | 70         |
| 8.1.3     | Spalling depth . . . . .                                | 71         |
| 8.2       | Block and wedge stability . . . . .                     | 71         |
| 8.2.1     | Limit equilibrium analysis . . . . .                    | 71         |
| 8.2.2     | Unwedge . . . . .                                       | 72         |
| 8.3       | Numerical modelling . . . . .                           | 72         |
| 8.4       | Input parameters for stability analysis . . . . .       | 75         |
| 8.4.1     | Rock mechanical parameters . . . . .                    | 75         |
| 8.4.2     | Post-peak behaviour . . . . .                           | 76         |
| 8.4.3     | Estimation of in-situ stress conditions . . . . .       | 77         |
| 8.4.4     | Joint parameters . . . . .                              | 78         |
| <b>9</b>  | <b>Stability analysis</b>                               | <b>81</b>  |
| 9.1       | Spalling . . . . .                                      | 81         |
| 9.1.1     | Potential for rock spalling . . . . .                   | 81         |
| 9.1.2     | Q-system approach and Spalling depth . . . . .          | 82         |
| 9.2       | Limit equilibrium analysis of block fall . . . . .      | 83         |
| 9.2.1     | Results . . . . .                                       | 85         |
| 9.3       | Unwedge analysis . . . . .                              | 86         |
| 9.3.1     | Model geometry and input parameters . . . . .           | 86         |
| 9.3.2     | Unwedge results . . . . .                               | 87         |
| 9.4       | Stress induced rock fall . . . . .                      | 88         |
| 9.4.1     | Model geometry . . . . .                                | 88         |
| 9.4.2     | Input parameters . . . . .                              | 89         |
| 9.4.3     | Results . . . . .                                       | 90         |
| 9.5       | Time dependent stress induced rock fall . . . . .       | 92         |
| 9.5.1     | Model geometry . . . . .                                | 92         |
| 9.5.2     | Input parameters . . . . .                              | 92         |
| 9.5.3     | Results . . . . .                                       | 94         |
| <b>10</b> | <b>Discussions</b>                                      | <b>97</b>  |
| 10.1      | Norwegian hydropower and hydraulic transients . . . . . | 97         |
| 10.2      | Stability assessments . . . . .                         | 98         |
| 10.2.1    | Timeline . . . . .                                      | 98         |
| 10.2.2    | Spalling potential . . . . .                            | 100        |
| 10.2.3    | Stress induced rock fall . . . . .                      | 100        |
| 10.2.4    | Structurally controlled rock fall . . . . .             | 102        |
| 10.2.5    | Weakness zone . . . . .                                 | 102        |
| 10.3      | Long-term stability . . . . .                           | 103        |
| <b>11</b> | <b>Conclusions and Recommendations</b>                  | <b>105</b> |

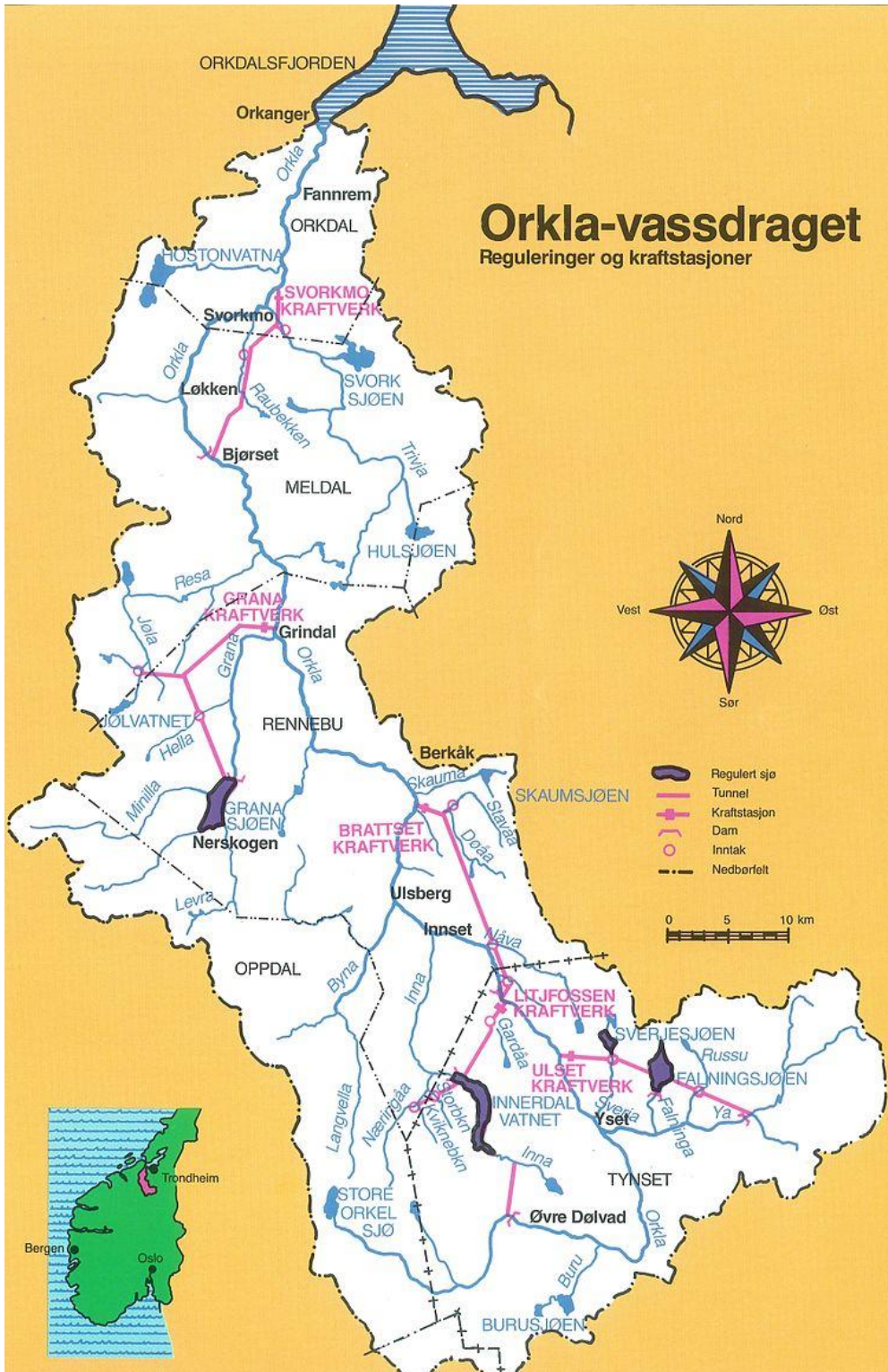
---

---

|   |            |
|---|------------|
| 11.1 Conclusion . . . . .                                       | 105        |
| 11.2 Recommendations . . . . .                                  | 106        |
| <b>Bibliography</b>   | <b>107</b> |
| <b>Appendices</b>   | <b>115</b> |
| A - Field work . . . . .  | 115        |
| B - Longitudinal profile of Ulset HPP . . . . .                 | 119        |
| C - Instabilities and failures in the headrace tunnel . . . . . | 121        |
| D - Laboratory work . . . . .                                   | 124        |

# Orkla-vassdraget

## Reguleringer og kraftstasjoner



# Introduction

## 1.1 Background of study

Norwegian hydropower is an underground industry. This statement can be made based on the fact that of the world's 600-700 underground power stations, 200 are located in Norway. From 1960-1990 an average of 100 km were excavated each year, and today more than 4000 km of underground tunnels have been excavated (Broch, 2013). Most Norwegian hydropower tunnels only have 2-4 % concrete or shotcrete lining, which means that most are unlined. This is the result of a support philosophy where some rock falls are accepted during the operation time of a hydropower tunnel (Broch, 1982).

Today's design criteria for hydropower tunnels are a result of over 100 years of experience in design and construction. The main design principle for unlined tunnels and shafts is to provide sufficient confinement in the rock mass, so that nowhere along the tunnel should the internal water pressure exceed the minor principle stress (Panthi, 2014*b*). In addition, certain geological conditions are unfavourable when excavating a tunnel or shaft and should be avoided. Such conditions are heavily jointed rock mass with open and intercommunicating joints, weakness zones, karstic areas, rocks with high porosity and impermeable layers which can cause high water pressure in critical locations (Nilsen and Thidemann, 1993).

In 1991 a de-regulation of the power market caused a change in the production scheme of hydropower stations. The production went from supply to demand driven, which means that the hydropower plant owner can alter the production based on demand and energy prices (Neupane and Panthi, 2018). This production pattern results in an increased frequency of start-and-stop cycles, which causes unsteady flows and pressure fluctuations in the waterway systems. These pressure fluctuations are not accounted for in the main design principle. In addition most water tunnels were built when the operation scheme was continuous with only a limited number of start-and-stop cycles. It is therefore of interest to look at the long-term effect of the new production pattern. Bråtveit et al. (2016) have



inspected some Norwegian water tunnels where the new operation scheme has been implemented and found that the frequency of rock falls has increased with a factor of 3.4 after the change.

The new operation scheme has also been implemented at Ulset Hydropower Project (HPP). Ulset HPP is situated in Tynset municipality in Hedmark county and is part of a system of five hydropower projects along the Orkla river system. An inspection of the headrace tunnel was conducted in 2017 and revealed many small to medium size block falls and some small scale collapses along the tunnel system. A study of the long-term stability issues of the headrace tunnel is therefore of interest, and to investigate how the new production pattern might have affected these instabilities.

## 1.2 Scope of study

The scope of study is given in the following:

1. Review on engineering geological and mechanical properties of the rock mass.
2. Review on the stability of water tunnels and instability assessment methodologies of tunnels and underground caverns.
3. Discussion of the engineering geological and registered instabilities along the headrace tunnel at Ulset HPP.
4. Systematise the instabilities and failures in different categories and after year of recorded failure.
5. Stability assessment of the recorded failures using empirical, analytical and numerical methods.
6. Discussion of the findings from the stability assessment and the long-term stability of the headrace tunnel at Ulset HPP.
7. Conclusion of the work with recommendations.

## 1.3 Methodology

The methodology used in this thesis can be categorised accordingly:

### 1. Literature study

Proceedings of "Fjellsprenningskonferansen" from The Norwegian Tunneling society (NFF), the search engine *Oria* and compendiums from different NTNU subjects have been the main source of information for the literature studies. The main topics of the literature studies can be divided into:

- I. Norwegian design principles for unlined waterway systems.
- II. Rock and rock mass properties and influencing factors
- III. Stability issues in underground tunnels and caverns.
- IV. Stability assessment methodologies of tunnels and underground caverns.

V. The introduction of water in tunnel systems and hydraulic transients.

## 2. Study of Ulset Hydropower Project

Information of Ulset HPP were gathered during the Project work, and have been used in the evaluation of the engineering geological conditions along the headrace tunnel. Geology of the project area was found through maps and field work, and rock mechanical properties were estimated through laboratory testing.

## 3. Identification and systematising of instabilities

Two reports and pictures from the tunnel inspection in 2017 are the basis for the instability assessment. Through archive exploration at Trønderenergi's offices at Berkåk, two more inspection reports from 1986 and 1992 were found. This made it possible to create a timeline of the failures and evaluate if the number of rock falls have increased after the implementation of the new operation scheme.

## 4. Stability assessment

Stability assessment of the identified failures/instabilities have been conducted by empirical, analytical and numerical methods. The techniques used are listed below:

I. Empirical method: Compressive and tensile strength approach (potential for rock spalling) after Diederichs (2007).

II. Empirical method: Q-system approach for potential to spalling from NGI (2015).

III. Semi-analytical method: Estimation of spalling depth according to Martin and Christiansson (2009).

IV. Analytical method: Limit equilibrium analysis of block fall (and Unwedge analysis, *Rocscience*).

V. Numerical methods: Finite element analysis with RS<sup>2</sup>, which is a computer program provided by *Rocscience*.

# 1.4 Limitations

The evaluation of instability issues in the headrace tunnel is based on a few inspection reports (1986, 1992 and 2017) and pictures, as the author did not participate in the tunnel inspection in 2017. Given a deviating quality of the pictures and notes, some locations and failure mechanisms might have been misinterpreted. The tunnel was also drained in 1987, but a report from this dewatering could not be found. This will have an impact on the timeline of the recorded failures.

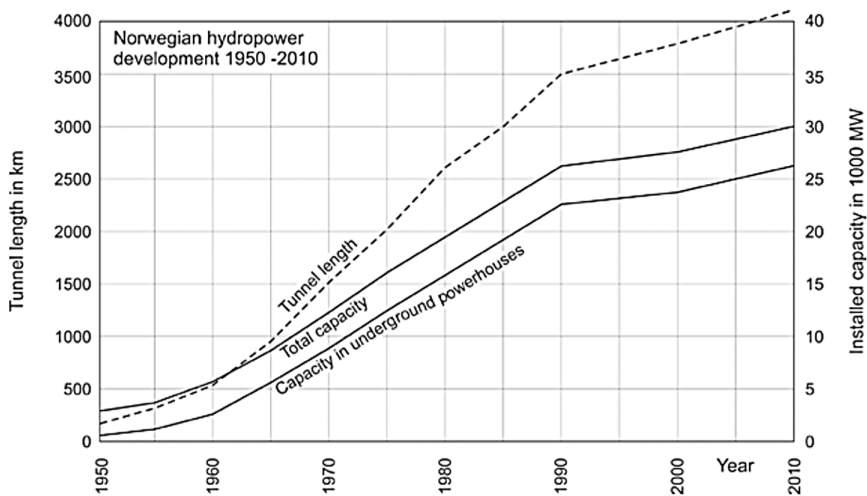
There have not been conducted any stress measurements or hydraulic fracturing test in connection with Ulset HPP. Therefore, stress measurements from the closest project and general stress orientations had to be adopted. The exact location of the trondhemite intrusions could not be determined through pictures and had to be assumed. As a result the overburden in the stability assessments is presumed to only consist of quartzitic schist.



# Norwegian Hydropower - An underground industry

## 2.1 Introduction

At the start of 2019 Norway had a mean yearly production of electric energy of 134.9 TWh, which constitutes 94 % of the country’s total energy production (NVE, 2019). The total installed capacity of Norwegian hydropower stations from 1950 to 2010 can be seen in Figure 2.1 (Broch, 2013).

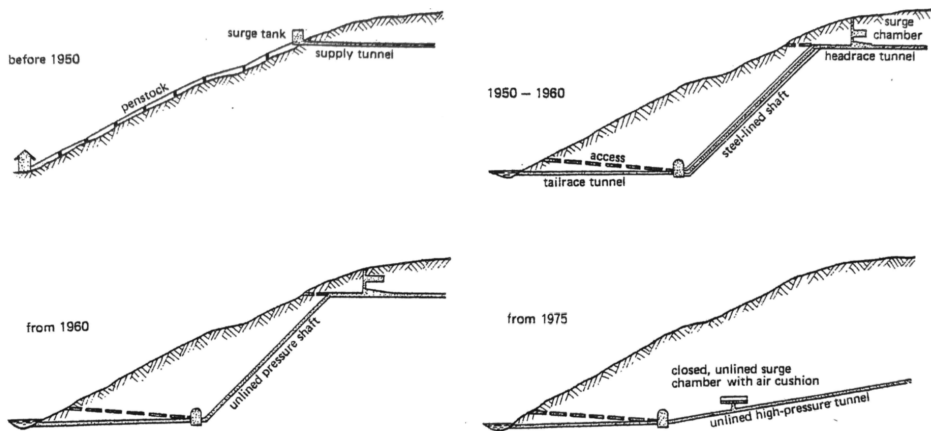


**Figure 2.1:** The total length of excavated hydropower tunnels from 1950 to 2010, together with the installed capacity from underground powerhouses and the total capacity from hydropower (Broch, 2013).

It shows that the capacity from underground powerhouses make up most of the energy production, and of the world's 600-700 underground powerhouses 200 of them can be found in Norway. From 1960-1990 an average of 100 km of tunnels were excavated each year. Today, 4000 km of underground water tunnels have been excavated. Based on these facts Broch (2013) states that the Norwegian electric industry is in fact an "underground industry".

## 2.2 Development of layout

The common layout for hydropower plants before 1950 can be seen in Figure 2.2 upper left. Water flowed from a horizontal supply or headrace tunnel to a surge tank placed on a valley side. The powerhouse was situated above ground beneath the surge tank, and water was conveyed to the station through a steel penstock. The outflow was then transferred to a river, lake or fjord (Broch, 1982).



**Figure 2.2:** Illustration of the development of layout of Norwegian hydropower plants (Broch, 1982).

In the 1950s the policy of placing stations underground was adopted. Myrset (1980) gives three reasons for why the industry was able to go underground:

1. An expansion in the electric power transmission network made it possible to transmit large quantities of electric power over great distances.
2. There had been an advance in blasting techniques.
3. An increased knowledge of rock masses and mechanical rock qualities.

The change from above ground to the underground gave security during wartime, required less maintenance and was better for the environment. Still the industry brought along the steel piping, and most pressure shafts from 1950 to 1960 were built with steel lining. This was not the first time the hydropower industry went underground. Between 1919 and 1921 four hydropower stations with unlined high pressure shafts were constructed with water head from 72-152 m. The reason was high steel prices and uncertain delivery, due

to a steel shortage after the First World War (1914-1918). Of these Svelgen hydropower station had the highest head of 152 m, and kept the record for almost 40 years. The record was not broken until 1958, when the Tafjord K3 was constructed with a water head of 286 m. This project gave the hydropower industry new-found confidence in unlined pressure shafts (Broch, 1985).

In 1973 the first unlined surge chamber with an air cushion was commissioned at Driva hydropower plant. The new design with an air cushion made it possible to replace the steep pressure shaft with a slightly inclined tunnel. The air cushion is a closed chamber constructed along the high-pressure tunnel, preferably close to the powerhouse. Compressed air inside the chamber acts as a cushion and reduces the water hammer effect on the water system and hydraulic machinery (Broch, 2006). The Norwegian specialities, unlined tunnels and high pressure shafts and air cushion chambers, have been the conventional layout of hydropower plants for the last decades.

## 2.3 Evolution of design criteria

Today's design criteria for hydropower plants is a result of many years of experience and evolution. According to Panthi (2014b) the hydropower plants with no major operation challenges have fulfilled two main design criteria. First is a suitable geo-tectonic environment or sufficient confinement in the rock mass, and secondly the required geological conditions. These two criteria, together with why the Norwegian geology is ideal for hydropower are described in the following.

### 2.3.1 Criteria of confinement

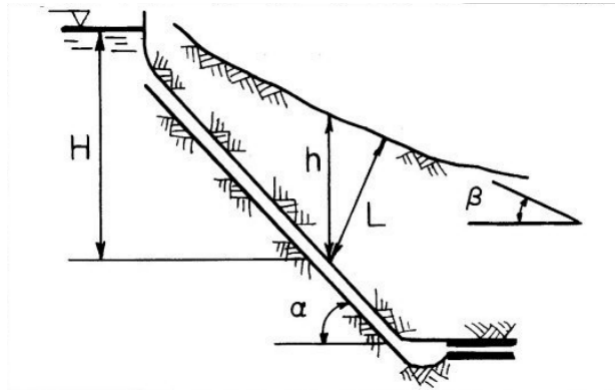
Before the 1970s different rule-of-thumbs were used in the planning and design for high pressure shafts. As new technology was developed, more advanced calculations could be done faster and easier. This resulted in design charts made from computer programs.

#### **Rule-of-Thumb**

The layout of hydropower tunnels in the 1960s until 1968 was the reason for the rule-of-thumb in the planning of the unlined pressure shafts, Figure 2.2. The rule can be expressed as (Broch, 1985):

$$h > c \times H \tag{2.1}$$

where  $h$  is the vertical depth of the point studied (m),  $H$  the static water head and  $c$  is a constant, which was 0.6 for valley sides with inclinations up to 35 degrees and increased to 1.0 for valley sides of 60 degrees. Figure 2.3 illustrates the definition of the parameters.



**Figure 2.3:** Illustration of the definition of parameters in the different rule-of-thumb (Broch, 2006).

A revised version of the rule-of-thumb was presented by Selmer-Olsen (1969) after failure in an unlined pressure shaft at Byrte . It had an inclination of 60 degrees and a water head of 300 m. This version would cover shafts with a higher inclination than 45 degrees, but not steeper than 60 degrees.

$$h > \frac{H \times \rho_w}{\rho \times \cos(\alpha)} \quad (2.2)$$

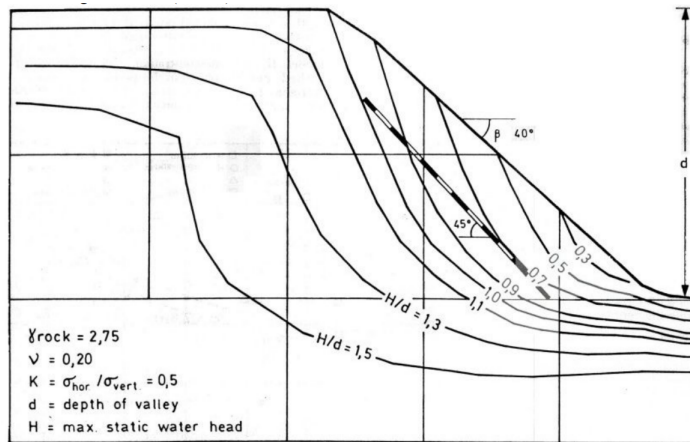
where  $\rho$  is the density of rock mass,  $\rho_w$  the density of water and  $\alpha$  the inclination of the shaft. A new rule-of-thumb was introduced in 1971 by Bergh-Christensen and Dannevig, after failure in an unlined tunnel at Askora hydropower project in fall 1970. This new rule took into account the inclination of the valley side (Broch, 1985).

$$L > \frac{\rho_w \times H}{\rho \times \cos(\beta)} \quad (2.3)$$

where  $L$  is shortest distance between point studied and surface and  $\beta$  is average inclination of the valley side. The definition of the parametes can be seen in Figure 2.3.

### Finite element method and design charts

As new and stronger computers became available a new design tool was introduced in 1971 - 1972. It uses computerised Finite Element Models which are based on strain analysis. Figure 2.4 illustrates the result from a finite element analysis presented in a design chart (Broch, 2006).



**Figure 2.4:** Design chart based on finite element model. The curves go through points where the internal water pressure in an unlined shaft or tunnel equals the minor principle stress in the rock mass (Broch, 2006).

Selmer-Olsen (1974) describes this design tool. The model can be adopted to any valley side, with different valley inclinations  $\beta$  and rock properties  $\rho$  and  $\nu$ . The stress situation is represented by the factor  $K$ , which is the ratio between the horizontal and vertical stress. The horizontal stresses, both tectonic and gravitational, are increasing linearly with depth.  $H$  is the maximum static water head and  $d$  the depth of the valley. The  $H/d$  ratio is defined as the static water head and is represented by the curves in the figure. These curves show where in the rock mass the water head equals the minor principle stress. They represent the minimum overburden required at different heights of the operation. A tunnel or shaft can then be drawn inside the chart so that the water pressure will not exceed the minor principle stress.

The idea behind the finite element models is to find where in the rock mass all parts of the shaft fulfills the following equation (Nilsen and Palmström, 2000; Panthi, 2014b):

$$\sigma_3 = H \times \gamma_w; \quad (2.4)$$

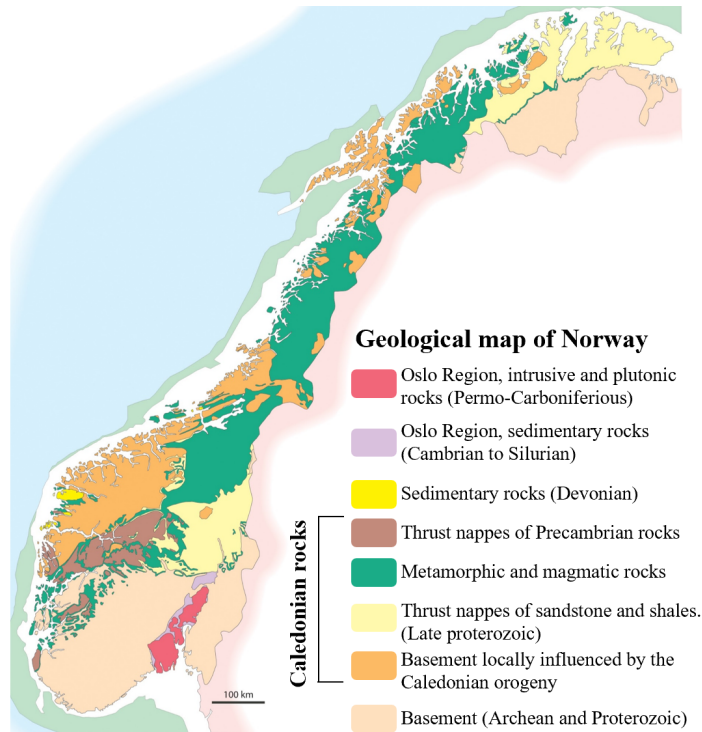
that the maximum water pressure in the tunnel should never exceed the minimum principal stress  $\sigma_3$ . This requirement is how the confinement criteria is commonly expressed today, and can easily be checked through numerical modelling (Panthi, 2014b).

### 2.3.2 Geological conditions in Norway

Norway is known as a hard rock province, where two thirds of the bedrock are Precambrian and the remaining one third is Paleozoic or Caledonian (Nilsen and Thidemann, 1993). Figure 2.5 shows the main geological areas of Norway. The Caledonian mountain range runs through the central part of Norway, where many rocks have undergone varying degree of metamorphosis due to the orogeny, such as schists, phyllites and greenstones.



Sandstones, shales and limestones are also a part of the mountain range together with other unmetamorphic rocks. The youngest Norwegian rock types can be found in the Oslo Region as Permian intrusives and extrusives. Unmetamorphic shales and limestones from Cambrian to Silurian ages are also typical for this region (Broch, 1982).



**Figure 2.5:** Geological map of Norway. Modified from (NGU, 2013).

The Caledonian orogenesis also lifted the Norwegian west coast approximately 1500 m. The ice during the later Quaternary glaciations wore away the weathered upper part of the rock mass, further developed valleys and fjords and exposed weakness zones. These processes gave the typically mountainous topography Norway is known for today, which is ideal for hydropower development. But the orogenesis also left the Norwegian rock mass anisotropic, heavily jointed and with high tectonic and residual stresses, that may lead to issues after and during construction of underground structures. It is therefore important to have knowledge of the geological conditions in an area before excavation, so that construction problems may be avoided or solved in an economical way. Even though, most Norwegian hydropower tunnels have only 2-4 % concrete or shotcrete lining. This is the result of a support philosophy where some rock falls are accepted during the operation time of a hydropower tunnel. If the rock falls don't develop into blockages, it will often not disturb the operation of the hydropower station (Broch, 1982).

# Rock and Rock mass properties

It is important to separate intact rock from a rock mass in engineering geology. A rock mass consists of intact rock, which has been separated by joints and other geological discontinuities into rock blocks and fragments (Nilsen and Palmström, 2000). The strength of the intact rock and the strength of discontinuities will therefore influence the strength of the rock mass, which again will influence the stability of an underground opening. In the crystalline rocks of Scandinavia, the importance of jointing can completely overshadow other rock properties (Nilsen and Thidemann, 1993).

## 3.1 Discontinuities

When a structural or geological feature changes or alters the homogeneity of a rock it is called a discontinuity. It is a general term for any mechanical discontinuity in a rock mass where the tensile strength is zero or close to zero. The mechanical behaviour of rock masses, particularly rock mass a few hundred meters from the surface, are largely influenced by discontinuities. A discontinuity could be a joint, weak bedding or schistosity planes, faults or weakness zones (ISMR, 1978; Nilsen and Palmström, 2000).

Discontinuities are mostly a result of tectonic activity, and the two main groups are joints and weakness zones. These will be described in the following sections.

### 3.1.1 Joints

ISMR (1978) defines a joint as a break of geological origin in the continuity of a body of rock along which there has been no visible displacement. Joints can be divided into different terms based on the size and composition of the joint, such as cracks, fractures and seams. They can also be divided based on the origin or the process which made it (Nilsen and Palmström, 2000):

*Bedding joints* - develops along the bedding planes in sedimentary rocks.

*Cooling joints* - forms during the cooling of a hot rock mass, such as igneous rocks.

*Exfoliation joints* - surface parallel joints as a result of chemical or physical forces. Can be a result of expansion and contraction due to temperature variations. Sheeted joints are also included in this group.

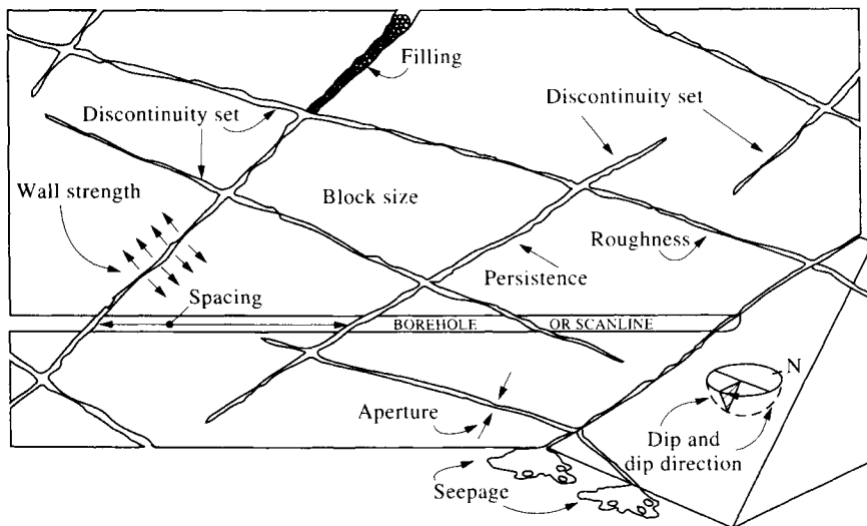
*Foliation joints* - develops along the foliation in metamorphic rocks.

*Sheeting joints* - develops along the surface typically in plutonic igneous intrusions, by unloading of the rock mass through erosion.

*Tectonic joints* - formed in a tensile stress field during uplift or lateral stretching of tectonic plates, or in regional tectonic compression.

A joint is often found accompanied by other parallel joints in a rock mass. These joints are referred to as joint sets. Joint sets intersect with other joint sets and form a joint system. In addition to the regular joint sets most rock masses have joints with irregular orientations known as random joints (Nilsen and Thidemann, 1993).

Figure 3.1 illustrates different geometrical and mechanical parameters which could be used to describe joints. According to Nilsen and Palmström (2000) the parameters which influence the joint shear strength and water flow through the rock mass are roughness, joint wall condition, filling material and the persistence of the joints.



**Figure 3.1:** Schematic representation of discontinuity characteristic in a rock mass (Hudson and Harrison, 1997).

### **Roughness**

The roughness will greatly effect the shear strength of the joint if there are only a small aperture (perpendicular distance between joint walls) and filling thickness. The roughness

can be represented by a large scale waviness and a small scale unevenness. When the discontinuity walls have high strength or the stress levels are low, both the waviness and unevenness will cause dilation when there is movement. If not, the unevenness will be sheared off. The roughness can be estimated during field mapping based on small scale (several cm) and intermediate scale (several meters) observations. The different roughness profiles can be seen in Figure 3.2. The intermediate scale is divided into three degrees, namely stepped, undulating and planar, and the small scale is again divided into rough, smooth and slickensided (ISMR, 1978).

| Relation between $J_r$ and $JRC_n$<br>Subscripts refer to block size (cm) |              | $J_r$ | $JRC_{20}$ | $JRC_{100}$ |
|---|--------------|-------|------------|-------------|
| I   | rough        | 4     | 20         | 11          |
|   | smooth       |       |            |             |
|   | slickensided |       |            |             |
| Stepped   |              |       |            |             |
| IV  | rough        | 3     | 14         | 9           |
|   | smooth       |       |            |             |
|   | slickensided |       |            |             |
| Undulating  |              |       |            |             |
| VII   | rough        | 1.5   | 2.5        | 2.3         |
|   | smooth       |       |            |             |
|   | slickensided |       |            |             |
| Planar  |              |       |            |             |

**Figure 3.2:** Typical roughness profiles. Relationship between  $J_r$  from the Q-system and  $JRC_n$ . Subscript refers to block size in cm (Barton, 1988).

Figure 3.2 also shows the relationship between the joint roughness  $J_r$  from the Q-system and the JRC from the Barton bandis criteria, which will be discussed in Sections 4.4.1 and 3.1.2 respectively.

### Wall strength and filling

When the walls in a discontinuity is in direct contact (unfilled joints), the compressive strength of the rock around the discontinuity is important for the shear strength (ISMR, 1978). If the surface of the walls are weathered or altered the roughness and frictional properties may be affected, which will change the strength of the joint walls.

Joints can have a coating (few mm) or filling material (larger than coating). Filling can be derived from breakage of the country rock due to movements, weathered materials or alteration products, deposited material and intrusions from igneous minerals and materials. Low friction material such as chlorite, talc, graphite and swelling clays can reduce the shear strength of joints. However, precipitation from hydrothermal solutions of calcite, quartz and other hard minerals may heal a joint, causing an increase in the shear strength (Nilsen and Palmström, 2000).

### Persistence

Persistence of a joint is the size, length and areal extent within a plane. It is one of the most important rock mass parameters, but the most difficult to quantify. Persistence can be divided into discontinuous joints, which terminate in massive rock mass, and continuous joints which end in other joints (Palmstrøm and Stille, 2010).

## 3.1.2 Shear strength of joints

The shear strength of a joint can be written as (Barton and Choubey, 1977):

$$\tau = \sigma_n \times \tan(\text{JRC} \times \log_{10}\left(\frac{\text{JCS}}{\sigma_n}\right) + \phi_r), \quad (3.1)$$

where  $\sigma_n$  is the normal stress acting on a plane, JRC is the joint roughness coefficient, JCS is the joint compressive strength and  $\phi_r$  is the residual friction angle. Barton and Choubey (1977) suggested that the residual friction angle could be estimated from:

$$\phi_r = (\phi_b - 20) + 20(r/R), \quad (3.2)$$

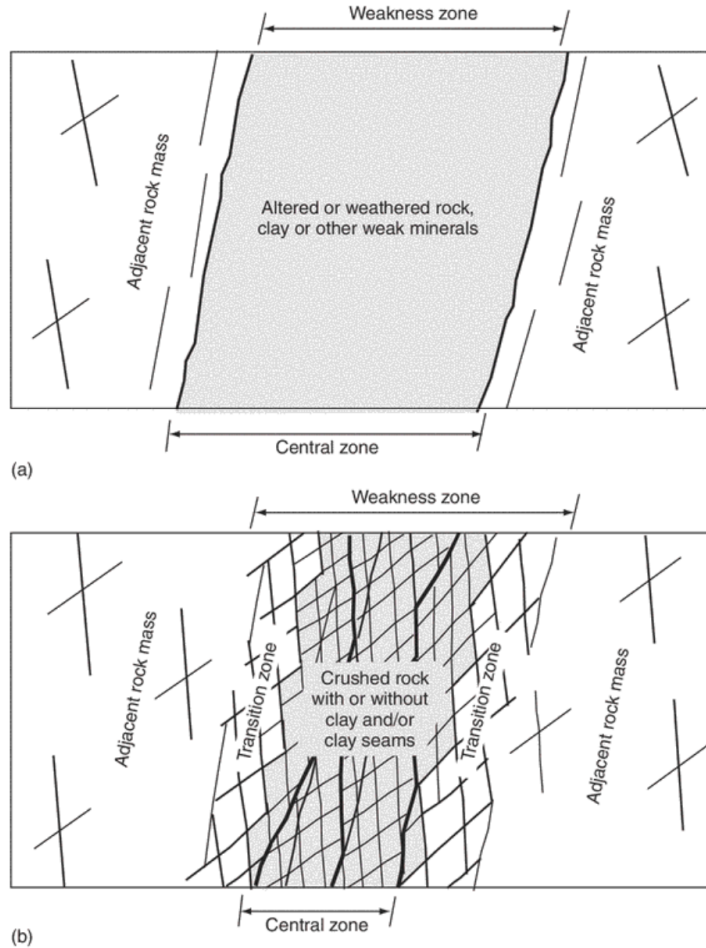
where  $\phi_b$  is the basic friction angle, r is the Schmidt rebound on wet joint surfaces and R the Schmidt rebound on dry weathered sawn surfaces.

## 3.1.3 Faults and weakness zones

Weakness zones can be seen as trenches or gorges at the earth's surface, and are often a problem in excavations as they can extend far into the rock mass. Weakness zones can be distinguished into two main categories illustrated in Figure 3.3 (Nilsen and Thidemann, 1993):

1. *Beds or layers of weak materials in sedimentary or metamorphic rocks.* Some layers in the rock mass might have a higher content of weak minerals such as weak clay minerals, mica, talc and graphite, which make them weaker than the adjacent layers. In mica schists, layers with a high content of mica will often be seen as a weak layer. Alteration of the rock can also lead to a weaker zone, as the strength of the binding material between grains can be reduced.

2. *Zones of crushed or altered rocks due to tectonic movements.* Faults and crushed zones are often a result of shear movement, and appear as parallel structures with the same characteristic features.



**Figure 3.3:** Weakness zone due to weak minerals or altered rock (a) and due to tectonic movements (b) (Palmström and Stille, 2010).

Fault and shear zones mainly consist of three parts, the central, transition and adjacent rock mass (Figure 3.3 b). The adjacent rock shows little influence of movement, but could be penetrated by seams that branch out from the zone. The transition part has a high degree of jointing, as it has been influenced by movement. It could also be exposed to some degree of alteration. Most movement has occurred in the central part of the zone, where the rock mass is heavily jointed or crushed. This allows hydrothermal activity and deposition of minerals to take place (Nilsen and Palmström, 2000).

### Filling and gouge material

Water can easily flow through a weakness zone, as the crushed part makes it highly permeable, and carry along different solutions, new minerals or alter existing minerals (Panthi, 2006). An overview of the different minerals and gouge materials that can be found in a weakness zone or fault is given in Table 3.1. For example can feldspar gradually be hydrolysed into clay minerals, which could reduce the strength of a weakness zone.

**Table 3.1:** Overview over filling and gouge material, which can be found in discontinuities. Modified after (Nilsen and Palmström, 2000).

| Filling or gouge material               | Properties of material  |
|---|---|
| Epidote, quartz and other hard minerals | Can have a healing or welding effect, which can increase stability.   |
| Sandy or silty materials                | Friction materials. May flow into immediately after excavation.   |
| Calcite                                 | Can be porous and flaky. May dissolve in water, leading to reduced shear strength.  |
| Gypsum                                  | Can exhibit the same properties as calcite.   |
| Inactive clay                           | Weak, cohesive materials with low friction.   |
| Swelling clay                           | Low friction (shear strength). Can swell with water present, which could lead to high swelling pressure if confined. Increase in instability. |
| Chlorite, talc or graphite              | Materials with very low friction, which can increase instability. Further increase if wet.  |

## 3.2 Rock mass strength and deformability

As described the rock mass strength depends on both the strength of the discontinuities and the intact rock blocks and fragments. In the following section the intact rock strength and influencing factors will be discussed, before the rock mass strength and deformability.

### 3.2.1 Intact rock strength

Rock is natural occurring, composed of one or more minerals. The composition of minerals and the binding forces between them, together with the shape, size and orientation of the minerals make up the properties of a rock. Some important physical properties of rocks are density, porosity and wave velocity. Rock strength and elasticity are examples of mechanical properties of intact rock (Nilsen and Thidemann, 1993).

Intact rock strength and deformability is normally determined through laboratory investigations or field tests (Nilsen and Palmström, 2000). The uniaxial compressive strength test is a common way of finding the uniaxial compressive strength  $\sigma_{ci}$ , Youngs modulus  $E$  and Poisson's ratio  $\nu$  of rocks, where cylindrical intact rock specimen are loaded until failure. The uniaxial compressive strength of intact rock is used in many different criteria

and classification system of rock masses. Factors that influence the intact rock strength will therefore also influence the rock mass strength. Such factors are saturation of the rock material, size of rock specimen for testing, weathering and alteration and rock anisotropy. These factors are described in the following.

### Saturation effect

Some rocks are weakened by the presence of water, where the strength of the rock may be reduced significantly. There are two effects water has on rocks, which are believed to be the reasons for the reduction in strength. Water can lead to a chemical deterioration of the cement or clay binder (Goodman, 1989). When rocks are in contact with water, the surface energy between grains will be reduced. The other reason is a reduction of the internal friction, as a result of a decrease in the effective stress due to pore and fissure water pressure (Broch, 1979; Goodman, 1989).

According to Broch (1979) isotropic magmatic rocks show no reduction in internal friction, and the reduction in strength is a result of chemical deterioration. However, in anisotropic gneisses there was a significant decrease in the internal friction and strength, which could be explained by a high content of micas. Table 3.2 shows the point load strength of a few water saturated rocks in percentage of strength for oven dry samples. Rocks such as basalt and quartzite had a slight increase in point load strength, while mica schist and gneisses had a significant decrease in point load strength.

**Table 3.2:** Point load strength of water saturated rock specimens in percent of strengths measured on oven dry specimens. Diametral testing on 32 mm cores. Re-produced from (Broch, 1979).

| Rock               | Era          | $I_{s(\text{sat.})}$ in percent of of $I_{s(\text{dry})}$ |                       | Mean value |
|--------------------|--------------|---|-----------------------|------------|
|                    |              | Normal to foliation                                       | Parallel to foliation |            |
| Basalt             | Permian      | 124   | 144                   | 134        |
| Quartzite          | Precambr.    | 94  | 106                   | 100        |
| Crystalline schist | Cambr.-Silur | 97  | 88                    | 92.5       |
| Mica Schist        | Cambr.-Silur | 119   | 44                    | 81.5       |
| Mica Schist        | Precambr.    | 89  | 58                    | 73.5       |
| Gneiss             | Precambr.    | 68  | 53                    | 60.5       |

Lajtai et al. (1987) conducted experiments to determine the effect of water on granite. Moisture in the testing environment caused more deformation and crack growth leading to lower ultimate long-term strength. In a few short-term experiments, when the environment was changed from dry to wet, the uniaxial compressive strength and fracture toughness of the granite were lowered by approximately 5 %. Time made the effect of water more substantial.

### Specimen size

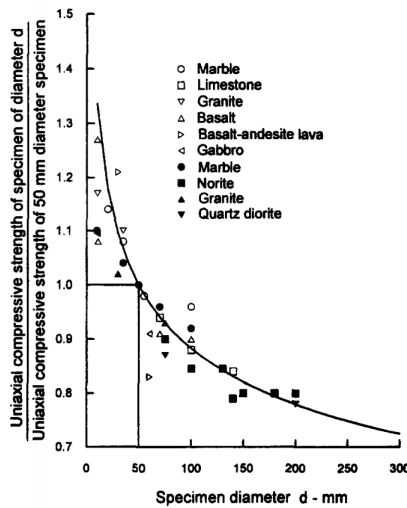
The uniaxial compressive strength decreases with the increasing size of the test specimen. Uniaxial compressive tests performed on smaller rock samples will therefore give too high strength values. Hoek and Brown (1980) have suggested a relationship to find the uniaxial



compressive strength of a 50 mm diameter rock core, if the test is performed on rock cores of another diameter:

$$\sigma_c = \frac{\sigma_{cd}}{\left(\frac{50}{d}\right)^{0.18}} \quad (3.3)$$

where  $\sigma_{cd}$  is the uniaxial compressive strength of a rock specimen with a diameter  $d$ . Figure 3.4 illustrates the data from which the relationship is based upon and the great influence the sample size has on the strength. The size dependency is also influenced by the degree of metamorphism. It is greater in highly schistose, foliated and deformed rocks, than in crystalline, unweathered rocks (Panthi, 2006).



**Figure 3.4:** Influence of the specimen diameter of rock cores on the uniaxial compressive strength of intact rock (Hoek and Brown, 1980).

### Weathering and alteration

Weathering is the mechanical disintegration or chemical decomposition of rocks at the earth's surface, while alteration is a change in rock composition caused by hydrothermal processes or chemical decomposition. Weathering and alteration affect the walls of discontinuities and lead to deterioration of the rock. The main results of the two processes are (ISMR, 1978; Nilsen and Palmström, 2000):

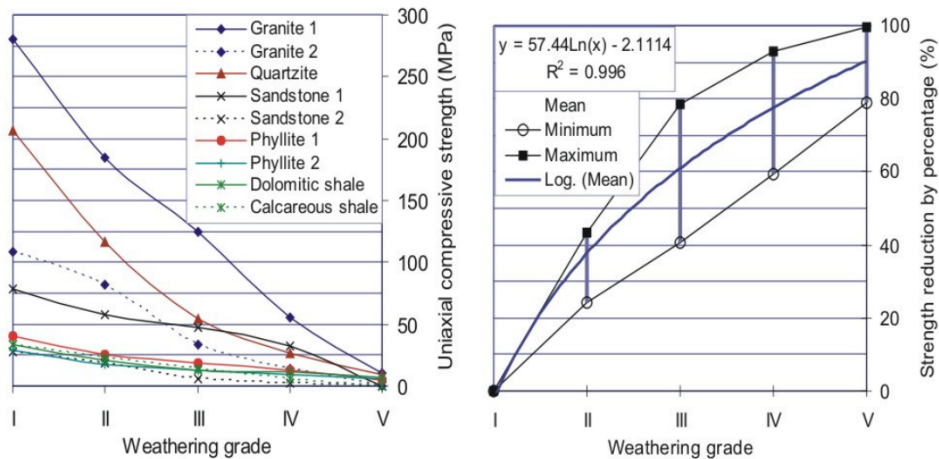
1. *Mechanical disintegration* or breakdown so that the rock loses its coherence. This process will not affect the composition of the rock, but lead to the opening of joints or formation of new joints due to rock fracture as grain boundaries are opened. It can also cause fracture of individual grains.
2. *Chemical decomposition* is the decay of the rock which leads to a change in the chemical and mineralogical composition, and will influence both the joint conditions

and the rock material. It can result in discoloration of the rock, decomposition of silicate mineral and leaching of calcite, anhydrite and salt minerals.

There are six different weathering classes defined by ISMR (1978) shown in Table 3.3. Weathering will reduce properties such as rock mass strength and deformability, and will influence the uniaxial compressive strength of various rock differently. Figure 3.5 indicates that the intact rock strength of sedimentary and meta-sedimentary rocks might be reduced by 40 percent by moderate weathering, and crystalline rocks may experience a reduction of 80 percent of the intact rock strength (Panthi, 2006).

**Table 3.3:** Classification of weathering grade according to ISMR (1978).

| Term                 | Description   | Grade |
|----------------------|---|-------|
| Fresh                | No visible sign of rock material weathering; perhaps slight discoloration on major discontinuity surfaces.  | I     |
| Slightly weathered   | Discoloration indicates weathering of rock material and discontinuity surfaces. All rock material may be discoloured by weathering and may be somewhat weaker externally than in its fresh condition. | II    |
| Moderately weathered | Less than half of the rock material is decomposed and/or disintegrated to a soil. Fresh discoloured rock is present either as a continuous framework or as corestones.                                | III   |
| Highly weathered     | More than half of the rock material is decomposed and/or disintegrated to a soil. Fresh discoloured rock is present either as a discontinuous framework or as corestones.                             | IV    |
| Completely weathered | All rock material is decomposed and/or disintegrated to a soil. The original mass structure is still largely intact.  | V     |
| Residual soil        | All rock material is converted to soil. The mass structure and material fabric are destroyed. There is a large change in volume, but the soil has not been significantly transported.                 | VI    |

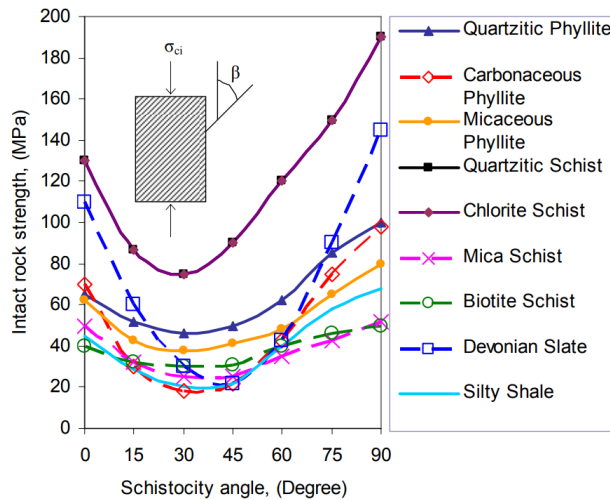


**Figure 3.5:** Uniaxial compressive strength (left) and strength reduction in percentage (right) as a function of weathering grade (Panthi, 2006).

**Rock anisotropy**

The degree of anisotropy in a rock is a result of the arrangement and amount of certain minerals. These minerals could be micas, chlorite, amphiboles and some pyroxenes. Anisotropy is greatest in sedimentary (layering and bedding planes) and metamorphic rock where the minerals can be found as parallel weak layers such as schistosity and foliation (Nilsen and Palmström, 2000).

The uniaxial compressive strength will be effected by the angle of loading to the weak layers in the rock. Figure 3.6 illustrates this effect, and shows that the rock strength is lowest when the loading direction is 30 degrees to the schistosity planes. The greatest strength is obtained when the planes are perpendicular to the loading direction (Panthi, 2006). It is important to have in mind the direction of these planes in rock samples, since testing at different angles may give different results.



**Figure 3.6:** The uniaxial compressive strength of different rocks with the schistosity planes at different angles to the loading direction (Panthi, 2006).

The degree of anisotropy can also be found through point load testing. It is found by first testing the point load strength normal and then parallel to the foliation of a rock.

**3.2.2 Rock mass strength**

The most common methods for strength testing of rocks are uniaxial compressive strength test, triaxial test and point load test. In these tests rock specimen, mostly rock cores, are loaded until failure (Nilsen and Thidemann, 1993). As a small rock specimen usually is strong and homogeneous, the strength of the rock specimen will not correctly represent the total rock mass strength. It is also difficult to directly measure the rock mass strength in the field or by laboratory testing (Panthi, 2006). Empirical formulas for estimating the rock mass strength  $\sigma_{cm}$  have therefore been suggested by different authors. Some of these formulas are presented in Table 3.4

**Table 3.4:** Empirical relationships for rock mass strength, where RMR is a rock mass characterization parameter,  $\gamma$  is the rock mass density ( $\text{g/cm}^3$ ) and Q is the Q-value.

| Proposed by       | Empirical relationship of rock mass strength  |
|-------------------|---|
| Bieniawski (1993) | $\sigma_{cm} = \sigma_{ci} \times e^{\left(\frac{\text{RMR}-100}{18.75}\right)}$    |
| Barton (2002)     | $\sigma_{cm} = 5\gamma \times \left(Q \frac{\sigma_{ci}}{100}\right)^{\frac{1}{3}}$ |
| Panthi (2006)     | $\sigma_{cm} = \frac{\sigma_{ci}^{1.5}}{60}$ , for schistose rock mass              |
| Panthi (2018)     | $\sigma_{cm} = \frac{\sigma_{ci}^{1.6}}{60}$ , for brittle rock mass                |

### 3.2.3 Rock mass deformability

Deformability is one of the most important parameters in rock engineering, and could be a better parameter for stability assessment than stress. Stress is a fictional physical parameter and cannot be measured directly or seen, while deformation can be measured directly. Deformability can be represented by a modulus, which gives the relationship between applied load and the resulting deformation. In-situ tests of the modulus of deformation is possible, but expensive and time consuming (Bieniawski, 1978). As a result many empirical relationships for the modulus of deformation  $E_m$  have been suggested from other classification systems and tests, such as uniaxial compressive test. Some of these are given in Table 3.5.

**Table 3.5:** Empirical relationships for rock mass deformability modulus, where GSI is the Geological Strength Index.

| Proposed by            | Empirical relationships of rock mass deformation modulus  |
|------------------------|---|
| (Bieniawski, 1978)     | $E_m = 2 \text{ RMR} - 100$   |
| (Hoek and Brown, 1997) | $E_m = \sqrt{\frac{\sigma_{ci}}{100}} \times 10^{\frac{\text{GSI}-10}{40}}$                                 |
| (Barton, 2002)         | $E_m = 10 \times Q_c^{\frac{1}{3}} = 10 \times \left(\frac{Q \times \sigma_{ci}}{100}\right)^{\frac{1}{3}}$ |
| Panthi (2006)          | $E_m = E_{ci} \times \frac{\sigma_{cm}}{\sigma_{ci}}$   |

### 3.2.4 Failure criteria

Several criteria to be able to predict when rock will fail have been developed in engineering geology. Two such criteria are the Mohr-Coulomb and Hoek-Brown failure criterion. A *criterion of failure* is the variations of peak stress  $\sigma_1$  with confining pressure  $\sigma_3$ . The peak stress of rock under deviatoric loading will increase as the rock is confined (Goodman, 1989).

#### Mohr-Coulomb failure criterion

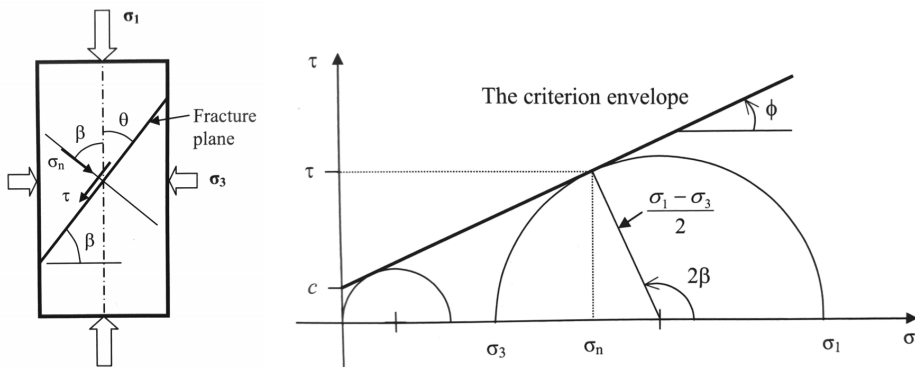
In 1773 Coulomb proposed a failure criterion based on his experiments into friction, which assumes that failure in a rock is due to a shear stress  $\tau$  acting along a plane (Jaeger et al., 2007). The Coulomb failure criterion is still widely used today and is as follows:

$$\tau = c + \sigma_n \tan \phi \tag{3.4}$$

where  $c$  is the cohesion,  $\sigma_n$  is the normal stress acting on the plane and the  $\phi$  is the internal friction angle.

A rock core is loaded until failure as illustrated in Figure 3.7 (left). The peak stress and confining pressure can then be presented in a  $\sigma - \tau$  diagram (right). The strength of the rock is given by the criterion envelop and are at low values approximately linear. The shear failure of the rock can be described by Equation 3.4. The internal friction angle is related to the fracture angles  $\beta$  and  $\theta$  as (Li, 2017b):

$$\beta = \frac{\pi}{4} + \frac{\phi}{2}, \theta = \frac{\pi}{4} - \frac{\phi}{2} \tag{3.5}$$



**Figure 3.7:** Rock core under deviatoric loading with stress components on the fracture plane (left) and graphical presentation of the Mohr-Coulomb failure criterion (right) (Li, 2017b).

The Mohr-Coulomb criterion is most suitable at high confining pressures, when the material fails through the development of shear planes. It is significant and valid for discontinuities and discontinuous rock masses (Hudson and Harrison, 1997).

### Hoek-Brown failure criterion

Rocks behave nonlinearly when the confining stress varies in a large span. Therefore, the nonlinear Hoek-Brown failure criterion would be better at capturing a realistic behaviour of rocks than the linear Mohr-Coulomb criterion (Li, 2017b). The original Hoek-Brown criterion was published by Hoek and Brown (1980). It has been updated by information gathered from its use in projects, and Hoek et al. (2002) published a *Generalised Hoek-Brown criterion* for jointed rock masses given by:

$$\sigma_1' = \sigma_3' + \sigma_{ci} \left( m_b \frac{\sigma_3'}{\sigma_{ci}} + s \right)^a \quad (3.6)$$

where  $\sigma_1'$  and  $\sigma_3'$  are the major and minor effective stresses at failure,  $m_b$  is a reduced value for the material constant  $m_i$  for intact rock and  $s$  and  $a$  are constant for the rock mass:

$$m_b = m_i \exp \left( \frac{GSI - 100}{28 - 14D} \right) \quad (3.7)$$

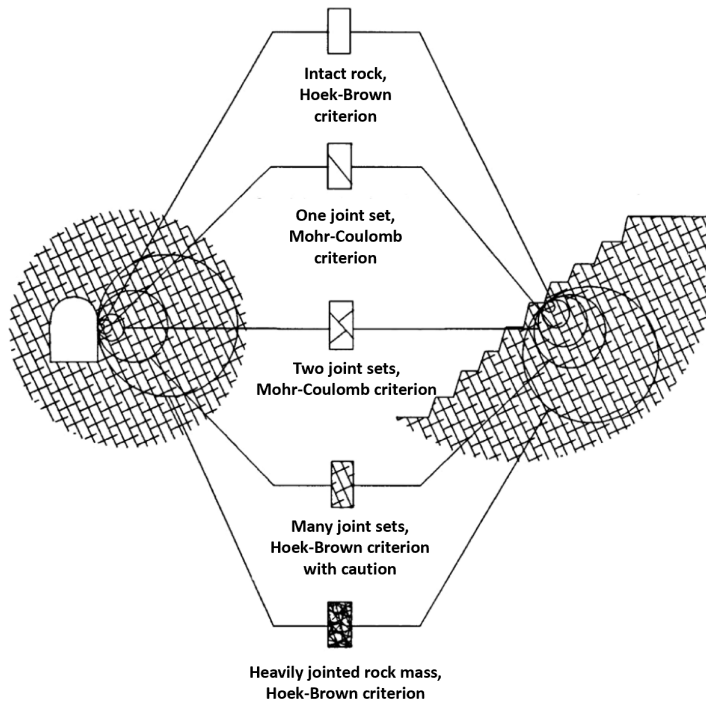
$$s = \exp \left( \frac{GSI - 100}{9 - 3D} \right) \quad (3.8)$$

$$a = \frac{1}{2} + \frac{1}{6} \left( e^{-GSI/15} - e^{-20/3} \right) \quad (3.9)$$

where GSI is the Geological Strength Index and D is the disturbance factor, which varies upon the degree of disturbance the rock mass has been subjected to by blast damage and stress relaxation. It lies between 0 for undisturbed rock masses to 1 for very disturbed rock masses (Hoek et al., 2002).

### Selecting failure criteria

The Hoek-Brown failure criterion should only be used for rock masses with closely spaced discontinuities, with similar surface characteristics. It should not be used when one of the discontinuities are weaker than the other's or the block size is as large as the analysed structure. Figure 3.8 illustrates the suitability of the to failure criteria.



**Figure 3.8:** How to select failure criteria according to rock mass conditions. Modified from Hoek (2007b).

# Stability of tunnels

According to Panthi (2006) the stability of a tunnel is a function of two features, rock mass quality and mechanical processes. The rock mass quality can be described by rock mass strength, rock mass deformability, strength anisotropy, discontinuities, weathering and alteration, which were explained in the previous chapter. The mechanical processes can be divided into rock stresses and ground water. This chapter will focus on rock stresses, how these are redistributed around an opening after excavation, the damage caused by excavation methods and stress related stability issues. In addition two different methods of classifying a rock mass, which have been used in this thesis, will be described.

## 4.1 Rock stresses

The in-situ or virgin stresses are the natural stress state in a rock mass prior to an excavation. It is composed of (Nilsen and Palmström, 2000):

*Gravitational stresses* - the weight of a rock mass, when the surface above an evaluated point is horizontal

*Topographic stresses* - when the surface is not horizontal there will be stress concentrations in valleys and stress relief in ridges

*Tectonic stresses* - because of tectonic movement. The activity along the margin of the 20 tectonic plates that make up the earth's outer shell

*Residual stresses* - remnant stresses which have been locked into the rock material

At any point in the rock mass, the resultant of these stresses can be represented by the *principal stresses*. The principal stresses can be defined the following way. At any point in the rock mass three planes exist, where there are only normal stresses and the shear stresses are zero. These normal stresses are the principal stresses. They are called the major  $\sigma_1$ , the moderate  $\sigma_2$  and the minor  $\sigma_3$  stresses, and can be measured (Li, 2017b).



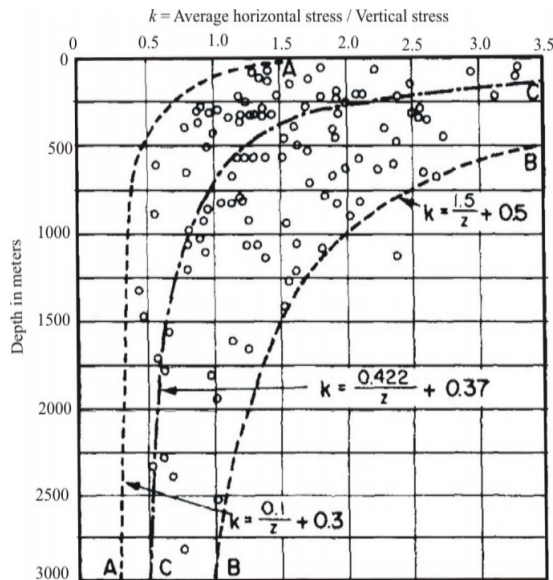
Gravity induces stresses in two directions in the ground, one vertical and one horizontal. At any depth  $z$  in the rock mass, where the surface above is horizontal, the vertical gravitational stress  $\sigma_v$  is

$$\sigma_v = \sigma_z = \rho g z, \tag{4.1}$$

where  $\rho \times g$  is the specific gravity  $\gamma$  of the rock. This is a generalisation and the vertical stress may deviate from this equation. The horizontal gravitational stress  $\sigma_h$  is often assumed to be proportional to the vertical stress and are defined by a constant  $k$ . It is the ratio of the average horizontal in-situ stress to the vertical, and can be expressed through the Poisson's ratio  $\nu$ .

$$\sigma_h = k\sigma_v = \frac{\nu}{1 - \nu} \sigma_v \tag{4.2}$$

Figure 4.1 shows how the  $k$  factor changes from above 1 to a lower constant value at depth. The average horizontal stress must therefore be influenced by plate tectonic movements (Panthi, 2006).



**Figure 4.1:** Variation in the horizontal to vertical stress ratio  $k$  (From (Panthi, 2006), after (Hoek and Brown, 1980)).

### 4.1.1 Redistribution of stresses

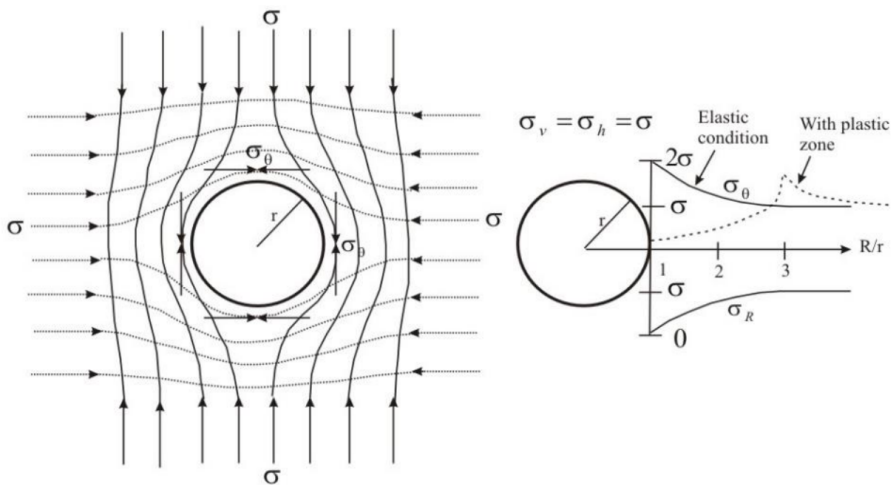
The in-situ or virgin stresses are disturbed when a tunnel or cavern is excavated. All principal stresses in vicinity of the excavation will be redistributed and vary based on the geometry of the opening and magnitude of the principal stresses (Nilsen and Palmström, 2000).

#### Circular tunnels

In an elastic material under isostatic stress conditions the redistributed stresses around a circular opening can be expressed according to *Kirsch solution* (Panthi, 2006), which is illustrated in Figure 4.2. In this situation the tangential stress at the boundary of the excavation is twice the principal stress and the radial stress is zero. Further from the opening, as the ratio between the radial distance and radius of the opening increases, the stresses will normalize. The magnitude of the tangential  $\sigma_\theta$  and radial  $\sigma_r$  stresses are given by Equation 4.3 and 4.4.

$$\sigma_\theta = \sigma \left( 1 - \frac{r^2}{R^2} \right) \quad (4.3)$$

$$\sigma_r = \sigma \left( 1 + \frac{r^2}{R^2} \right) \quad (4.4)$$



**Figure 4.2:** Stress trajectories in rock mass around an circular opening (left) and tangential and radial stresses under elastic and non elastic conditions (right) (Panthi, 2006).

When the situation is not isostatic, the major and minor principle stresses will result in variations in the tangential stress. *Kirsch solution* then states that the maximum tangential

stress  $\sigma_{\theta_{max}}$  and minor tangential stress  $\sigma_{\theta_{min}}$  will be where the major and minor principal stresses are tangent with the opening, respectively. They can then be calculated by the following equations:

$$\sigma_{\theta_{max}} = 3\sigma_1 - \sigma_3 \tag{4.5}$$

$$\sigma_{\theta_{min}} = 3\sigma_3 - \sigma_1 \tag{4.6}$$

which are valid for homogeneous, isotropic and elastic rock masses.

**Non-circular openings**


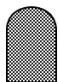







The equations presented above are not valid for non-circular tunnels. Non-symmetrical geometry and sharp corners will greatly affect the tangential stresses (Nilsen and Palmström, 2000).

Hoek and Brown (1980) suggest a way to estimate the tangential stresses around openings with different shapes in massive rock. The magnitude of the tangential roof stress  $\sigma_{\theta_r}$  and tangential wall stress  $\sigma_{\theta_w}$  can be found by:

$$\sigma_{\theta_r} = (A \times k - 1)\sigma_z \tag{4.7}$$

$$\sigma_{\theta_w} = (B - k)\sigma_z \tag{4.8}$$

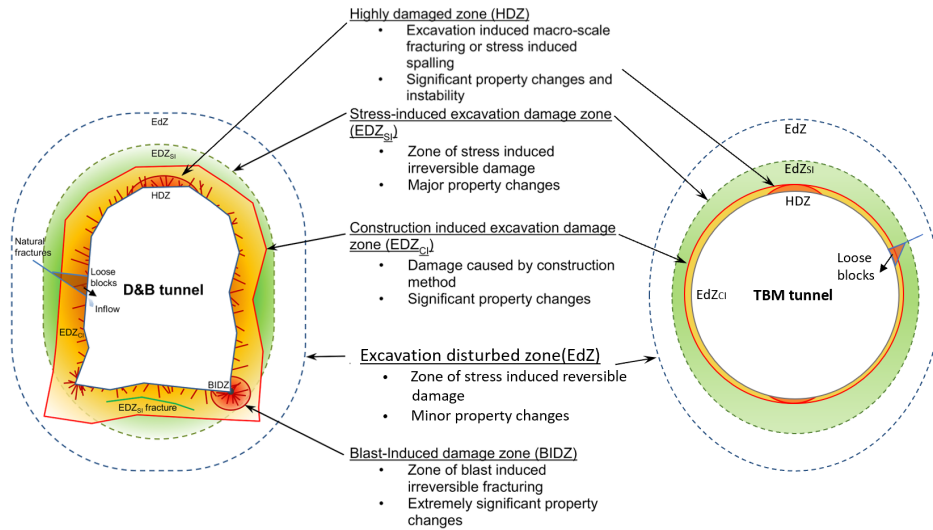
where A and B are wall factors for various tunnel shapes, which can be found in Figure 4.3.  $\sigma_z$  is the vertical in-situ stress.

| TUNNEL SHAPES |   |   |   |   |   |   |   |   |   |
|---------------|---|---|---|---|---|---|---|---|---|
|               |  |  |  |  |  |  |  |  |  |
| A             | 5.0   | 4.0   | 3.9   | 3.2   | 3.1   | 3.0   | 2.0   | 1.9   | 1.8   |
| B             | 2.0   | 1.5   | 1.8   | 2.3   | 2.7   | 3.0   | 5.0   | 1.9   | 3.9   |

**Figure 4.3:** Values for A and B for different shapes of underground openings (re-produced from (Hoek and Brown, 1980)).

**4.2 Excavation method**

Excavation of an opening will influence the surrounding rock mass as seen in Figure 4.4. Siren et al. (2015) divide the influenced area into five different zones based on tunnelling method. The two most common techniques in rock tunnelling are excavation by D&B (Drill-and-Blast) or TBM (Tunnel Boring Machine).



**Figure 4.4:** Excavation damage divided into different zones. Modified from (Siren et al., 2015).

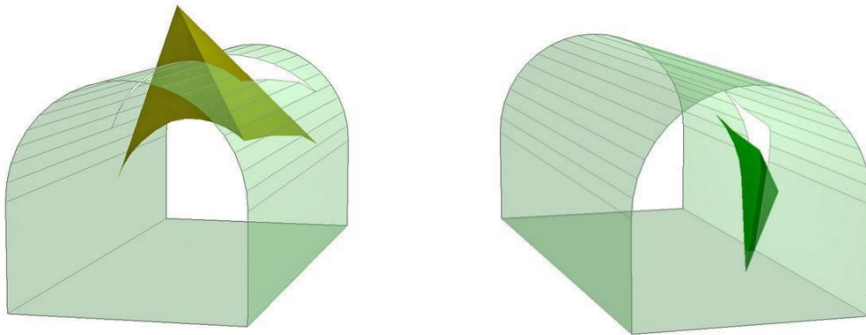
The major difference between the tunnelling methods is the so called construction induced Excavation Damage Zone ( $EDZ_{CI}$ ), which will be greater for a D&B tunnel. This is the result of the blasting, which will induce cracks and fractures weakening the rock mass. The weakened rock mass will no longer be able to carry the rock stresses, which will result in high tangential stresses in the stress-induced Excavation Damage Zone ( $EDZ_{SI}$ ). The Excavation Disturbed Zone (EdZ) is the furthest zone around an opening in which reversible changes caused by stress redistribution have occurred. The zone can reach far from the opening (Siren et al., 2015).

## 4.3 Stability issues

As described in the previous sections, after excavation of a tunnel or cavern the in-situ stresses will be disturbed and redistributed around the opening as induced stresses. This may cause stress concentrations or stress relief at the boundary of the opening. The most common types of failure in hard rock excavations are falling or sliding of wedges or blocks as a result of gravity. In massive hard rock subjected to very high stresses, failure of the rock mass is the most common failure mode (Hammett and Hoek, 1981).

### 4.3.1 Structurally controlled failure

At shallow depths the most common type of failures are wedge/block fall or sliding from the periphery of the tunnel. To form a wedge, three weak planes need to present. Such planes could be structural features or discontinuities (bedding planes or joints) in the rock mass. The fourth plane is the periphery of the excavation as illustrated in Figure 4.5. If the restraint from the surrounding rock mass is too small, these wedges may fall from the roof or slide along planes in the walls (Hoek, 2007a).



**Figure 4.5:** Wedges formed by three intersecting structural features in the roof (left) and the wall (right). These wedges may fall or slide if the restraint around the opening is too small (Hoek, 2007a).

If the wedges or blocks are allowed to fall or slide, the stability of the opening may worsen rapidly. Failed wedges will create a reduction in restraint and interlocking of the jointed rock mass and a free face for other wedges to fall and slide from. Additional wedge fall will then continue until the opening is full of material or a natural arc is created around the opening (Hoek, 2007a).

### 4.3.2 Stress induced failure

If the induced stresses around an excavated opening exceed the rock mass strength, the rock may fail in two different modes (Panthi, 2006):

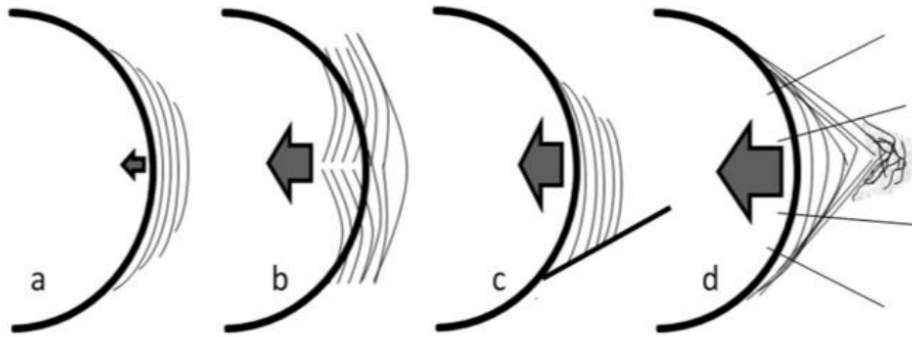
1. Rock spalling or rock bursting in hard, strong and brittle rock masses
2. Squeezing or deformation in weak rock masses

The rock masses located at Ulset HPP are strong and massive and will therefore fail according to the first mode, which will be explained in the following.

#### **Rock spalling and rock burst**

According to Diederichs (2014) rock burst can be classified according to the mechanism that triggered the rock burst. The three different classes are rock buckling due to fracturing, rock ejection due to seismic energy transfer and rockfalls induced by seismic shaking. The instabilities registered in the headrace tunnel at Ulset HPP are not believed to be a cause of seismic energy, which will therefore not be discussed further.

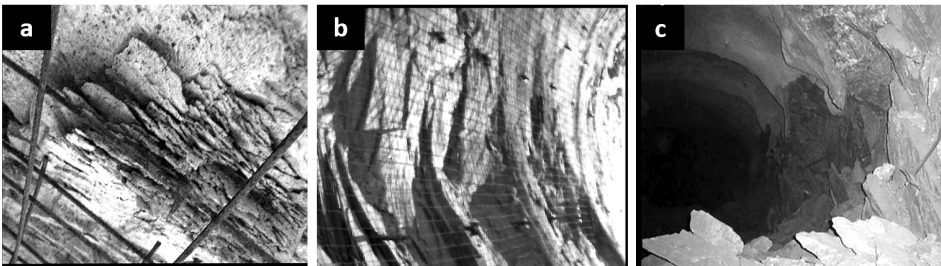
Rock buckling due to fracturing or strain burst is a sudden stress induced rock failure (Diederichs, 2014). Strain bursting is the violent rupture of rock under high stresses. In rock prone to spalling, extension fractures (spalling) may develop before the failure evolves into the strain burst or rockburst. The development of different stress induced failures in brittle rock mass is illustrated in Figure 4.6. In unsupported conditions and in an anisotropic stress situation, spalling may form notch geometries which often are confused with wedge failure (Diederichs, 2007).



**Figure 4.6:** Propagation of stress induced failure in a brittle rock mass. a) Non-violent spalling b) bursting through buckling c) spalling intersecting with structure and d) dilational yield (Diederichs, 2014).

Under compressive loading, visible extension fractures may develop as spalling in a violent or non-violent manner. High rock stresses induce fractures parallel to the tunnel boundary, and if the spalling-plates are thicker than a few centimetres the failure is called slabbing (Li, 2017b). These surface-parallel induced fractures can be seen in Figure 4.6 a. If the spalling is not allowed to be released, it may evolve into a buckling instability. Here the energy and volume of the slabs are large enough to be called a rock burst (Figure 4.6 b). In a discontinuous rock mass, the induced fracturing may reach a structure such as a joint, and the result will be a structurally controlled strain burst, Figure 4.6 c. Figure 4.6 d illustrates the development of a full rock burst, where the initial fracturing is being restrained. The fracturing propagates further into the rock mass, where a combination of fracturing and dilation can lead to a sudden rupture and release of rock mass (Diederichs, 2014).

Figure 4.7 shows different degrees of spalling damage in underground openings. From minor spalling in roof to strain-bursting of a notch shape spalling zone.



**Figure 4.7:** Increased level of spalling. a) minor surface parallel spalling in crown, b) release of 50 cm of spalled ground in TBM tunnel and c) strain-burst of a notch shape spalling zone in deep mine drift. Modified from (Diederichs, 2007).

## 4.4 Classification methods

The two rock mass classification methods used in this thesis are described in the following.

### 4.4.1 Q-system

The Q-system was developed by Barton et al. (1974a) at the Norwegian Geotechnical Institute (NGI), and has been updated over the last decades with the advancements in support philosophies and -technologies. It is a system for classification of rock masses, which also can be related to the stability of an underground excavation (NGI, 2015). The  $Q$ -value gives a description of the rock mass quality and can be calculated from six different parameters (Barton et al., 1974a):





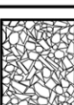
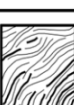
$$Q = \frac{RQD}{J_n} \times \frac{J_r}{J_a} \times \frac{J_w}{SRF}, \quad (4.9)$$

where  $RQD$  is the degree of jointing (rock quality designation),  $J_n$  is the joint set number,  $J_r$  the joint roughness number,  $J_a$  the joint alteration number,  $J_w$  the joint water reduction factor and  $SRF$  is the stress reduction factor.

These parameters can be determined through geological mapping using tables given by NGI (2015). Together they make up three main factors which describe the stability of an underground opening.  $\frac{RQD}{J_n}$  describes the degree of jointing or block size, and the stability will decrease with the increase in joint set number and smaller spacing between joints.  $\frac{J_r}{J_a}$  is the joint friction or inter-block shear strength, where rough joints or joints with thin hard filling will be favourable for the stability. The active stress,  $\frac{J_w}{SRF}$ , describes the stresses in the rock mass and usually moderate stress situations are preferred.

### 4.4.2 GSI

The Geological Strength Index (GSI) can be used to evaluate the reduction in rock mass strength for different geological settings. Both the properties of the intact rock and the single block's ability to move and rotate make up the strength of a jointed rock mass (Hoek and Brown, 1997). The GSI-value is based on visual impression of the rock mass in terms of blockiness and surface conditions of the discontinuities (joint roughness and alteration) (Nilsen and Palmström, 2000). The GSI-value is one parameter required in numerical modelling, with the use of RS<sup>2</sup> (Phase2).

| <p><b>GEOLOGICAL STRENGTH INDEX FOR JOINTED ROCKS (Hoek and Marinos, 2000)</b></p> <p>From the lithology, structure and surface conditions of the discontinuities, estimate the average value of GSI. Do not try to be too precise. Quoting a range from 33 to 37 is more realistic than stating that GSI = 35. Note that the table does not apply to structurally controlled failures. Where weak planar structural planes are present in an unfavourable orientation with respect to the excavation face, these will dominate the rock mass behaviour. The shear strength of surfaces in rocks that are prone to deterioration as a result of changes in moisture content will be reduced is water is present. When working with rocks in the fair to very poor categories, a shift to the right may be made for wet conditions. Water pressure is dealt with by effective stress analysis.</p> |   | <p><b>SURFACE CONDITIONS</b></p> <p>VERY GOOD<br/>Very rough, fresh unweathered surfaces</p> <p>GOOD<br/>Rough, slightly weathered, iron stained surfaces</p> <p>FAIR<br/>Smooth, moderately weathered and altered surfaces</p> <p>POOR<br/>Slickensided, highly weathered surfaces with compact coatings or fillings or angular fragments</p> <p>VERY POOR<br/>Slickensided, highly weathered surfaces with soft clay coatings or fillings</p> <p>DECREASING SURFACE QUALITY →</p> |     |    |     |     |
|---|---|---|-----|----|-----|-----|
| <p><b>STRUCTURE</b></p>   |   | <p>DECREASING INTERLOCKING OF ROCK PIECES ↓</p>   |     |    |     |     |
|    | <p>INTACT OR MASSIVE - intact rock specimens or massive in situ rock with few widely spaced discontinuities</p>   | 90  |     |    | N/A | N/A |
|   | <p>BLOCKY - well interlocked undisturbed rock mass consisting of cubical blocks formed by three intersecting discontinuity sets</p>                     | 80  | 70  |    |     |     |
|    | <p>VERY BLOCKY- interlocked, partially disturbed mass with multi-faceted angular blocks formed by 4 or more joint sets</p>                              |   | 60  |    |     |     |
|    | <p>BLOCKY/DISTURBED/SEAMY - folded with angular blocks formed by many intersecting discontinuity sets. Persistence of bedding planes or schistosity</p> |   | 50  | 40 |     |     |
|    | <p>DISINTEGRATED - poorly interlocked, heavily broken rock mass with mixture of angular and rounded rock pieces</p>                                     |   |     | 30 | 20  |     |
|    | <p>LAMINATED/SHEARED - Lack of blockiness due to close spacing of weak schistosity or shear planes</p>  | N/A   | N/A |    | 10  |     |

**Figure 4.8:** Characterisation of rock mass based on blockiness and joint conditions ((Hoek and Brown, 1997) found in (Hoek, 2007b)).





## The impact of water

This chapter will focus on the issues that arises when water is introduced to a tunnel. In addition a new way of operating hydropower stations was implemented in 1991, where the operation scheme was changed from supply to demand driven, resulting in an increase in start-and-stop cycles. This introduces higher frequencies of pressure fluctuations along the tunnel system, which could worsen instabilities. Two case studies have been conducted to understand the effects water and pressure fluctuations have on the stability of a tunnel or shaft.

### 5.1 Watering and dewatering

When a tunnel is excavated groundwater will leak through pores and joints in the tunnel contour, and the leakage will after some time be reduced to an even flow. During the first watering (filling) of the tunnel the drained pores and joints will be filled with water again, which will give rise to a water pressure. The water pressure, if large enough, can lead to deformation of the rock mass (Palmstrøm and Schance, 1987). The result could be hydraulic fracturing if the pressure exceed the minor principal stress. The first watering of a tunnel or pressure shaft should therefore be performed with care. Palmstrøm and Broch (2017) suggest to fill a tunnel in steps or intervals of 10 to 30 hours. Measurements of the water level should be conducted during the intervals to evaluate potential leakage.

Monitoring of the hydropower station is vital in the first months of operation, as an increase in head loss can be a sign of stability problems in the tunnel system. Serious fall-outs of rock masses can give an increase of a few centimetres, while an increase of 1 m may indicate a collapse (Palmstrøm and Broch, 2017). As discussed previously, the strength of rocks and shear strength of joints will be reduced with the introduction of water, this will normally lead to block fall over time. According to Bruland and Thidemann (1991) there has also been an increase in block falls during dewatering as rocks, which have loosened over time, will fall down when the pressure the water exerts on the tunnel periphery is removed. Discussions with supervisor Dr. Krishna Kanta Panthi (18.02.2019) reveal another

problem with dewatering. The emptying of water from a tunnel system will also lead to draining of the joints. If the time it takes to drain the joints is longer than draining the tunnel, an increased water pressure will act on the joints. At the same time there is no longer a pressure from the water acting on the tunnel contour. This increased water pressure could further aggravate any instability in the tunnel system. The worst case scenario would be a pressure from both the static head and mass oscillations, which will be described in the following.

## 5.2 Hydraulic transients

There is a steady water flow in the tunnel system of a hydropower plant during continuous operations. When the steady water flow is disturbed, by for example opening or closing of valves, unsteady motions will occur in the form of hydraulic transients. These motions can be divided into two (Guttormsen, 2006):

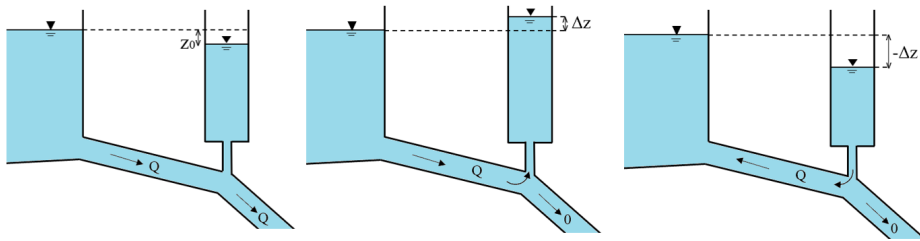
1. Water hammer
2. Mass oscillations

### 5.2.1 Water hammer and mass oscillations

The water hammer is a phenomenon that appears in pressure tunnels when there is change in water discharge, such as a rapid opening or closing of a valve or start and stop of turbines and pumps (Popescu et al., 2003). At first the water flowing through the tunnel system has a constant velocity, but when the valve closes the water velocity just upstream of the valve will change to zero. This leads to a pressure increase as the kinetic energy of the water changes to potential energy. The pressure will act as a wave and propagate towards a free water surface, such as the reservoir. At the free surface the wave will be reflected and sent back towards the valve. This continues until the pressure wave dampens out. The amplitude of the pressure wave needs to be minimised, as it can cause severe damage on turbines, valves and the water system. This can be accomplished by installing a surge tank or an air cushion chamber, which will reduce the travel distance of the pressure wave (Guttormsen, 2006).

By installing the surge chamber another problem is introduced, namely mass oscillations. Because of the surge chamber the water hammer will only appear in the penstock, while mass oscillations are slow variation in the water flow between the surge chamber and the reservoir (Popescu et al., 2003). A simple illustration of how mass oscillations develop is given in Figure 5.1.

Under continuous operations the water will flow from the reservoir to the turbines, with a constant water discharge  $Q$ . A water level difference  $z_0$  between the reservoir and the surge tank will develop because of the headloss in the tunnel (left). When the valve closes the water will be forced up into the surge tank, and the water level will rise until the pressure is high enough to stop the water in the tunnel (right). Water will then flow from the surge tank to the reservoir as a result of a pressure difference, until the water reaches a certain level in the surge tank (right). This process continues until the mass oscillations are dampened out by friction in the tunnel system (Rasten, 2014).



**Figure 5.1:** Simple illustration of mass oscillations in hydroelectric power plant with surge tank. Continuous operation (left), closing of regulation valve (middle) and acceleration of water back towards the reservoir (right) (re-produced from (Popescu et al., 2003; Rasten, 2014)).

When the valve again opens the turbines will retrieve water from the surge tank and set the water in the upper tunnel system in motion. The reservoir will feed the turbines, at the same time as water flows back into the surge tank. This will set in motion the same kind of oscillations as for the valve closing, but smaller as the water also flows to the turbines (Rasten, 2014).

## 5.2.2 The impact of hydraulic transients

While there have been some studies conducted on the effects of water hammers, studies on mass oscillations are harder to find. Helwig (1987) investigated the effect of transient water pressure from water hammer on the rock mass, and concluded that the effect can only be found in the rock mass close to the tunnel periphery. Also, the duration of water hammers are too short to have any major impact on the pore water pressure. Mass oscillations last for a longer period and could have a greater effect on the rock mass around a tunnel.

Bråtveit et al. (2016) have conducted an investigation on the effect of *hydropeaking* in some unlined Norwegian hydropower tunnels. Tunnels subjected to hydropeaking are tunnels with the new operation scheme. Their study concluded that in these tunnels rock falls had increased with a factor of 3.4, but the relative size of the rock falls had decreased. Most of the major failures in the tunnels had occurred in or close to weakness zones containing swelling clay.

The effect pressure fluctuations may have on instabilities has been studied at Brattset hydropower project by Halseth (2018). After the change in production pattern the number of instabilities in the headrace tunnel had increased, and it was concluded that the pressure fluctuations could be a reason for this trend. The period of one cycle of mass oscillation at Brattset HPP is almost five minutes, which is 200 times longer than for the water hammer wave. Leading to the belief that the long period of mass oscillations may have the potential to affect the stability of the tunnel system.

## 5.2.3 Mass oscillations at Ulset HPP

Hydraulic transients in hydropower tunnels have been discussed by Guttormsen (2006); Jaeger (1977); Popescu et al. (2003); Rasten (2014). The reader is referred to these literature's for detailed explanation of theory and deriving of formulas.

### Formulas

As the penstock at Ulset HPP is steel lined, only the rock mass between the air cushion chamber (ACC) and reservoir will be affected by mass oscillations. The maximum amplitude  $\Delta z$  for mass oscillations in a tunnel system with a surge chamber is given by

$$\Delta z = \Delta Q \sqrt{\frac{\sum l/a}{gA}}, \quad (5.1)$$

where  $\Delta Q$  is the change in water discharge,  $l$  is the tunnel length between the air cushion chamber and the reservoir,  $a$  the tunnel cross sectional area and  $A$  is the cross sectional area of the surge chamber.

An air cushion chamber behaves like an open shaft, where the cross section decreases with surge elevation. Therefore the calculations for an open shaft surge chamber can be used for an air cushion chamber with any geometry, when an equivalent shaft area  $A_{eq}$  is substituted for the surge chamber area in equation 5.1 (Goodall et al., 1988).

$$A_{eq} = \frac{1}{\frac{1}{A_o} + \frac{n \cdot h_{p0}}{V_o}} \quad (5.2)$$

where  $A_o$  is the area of the water surface inside the air cushion chamber,  $n$  polytropic index,  $h_{p0}$  absolute air pressure in meter (water head) and  $V_o$  is the air volume of the air cushion chamber.

The period of mass oscillations  $T$  is given by:

$$T = 2\pi \sqrt{\left(\sum \frac{l}{a}\right) \frac{A_{eq}}{g}} \quad (5.3)$$

### Calculations

The tunnel system at Ulset HPP, between the air cushion chamber and the reservoir, can be divided into three sections. The TBM-section is 4877 m long with a cross sectional area of 16 m<sup>2</sup>, the sand trap is 65 m with an area of 35 m<sup>2</sup> and the drill and blast section is 2296 m with an area of 22 m<sup>2</sup>.

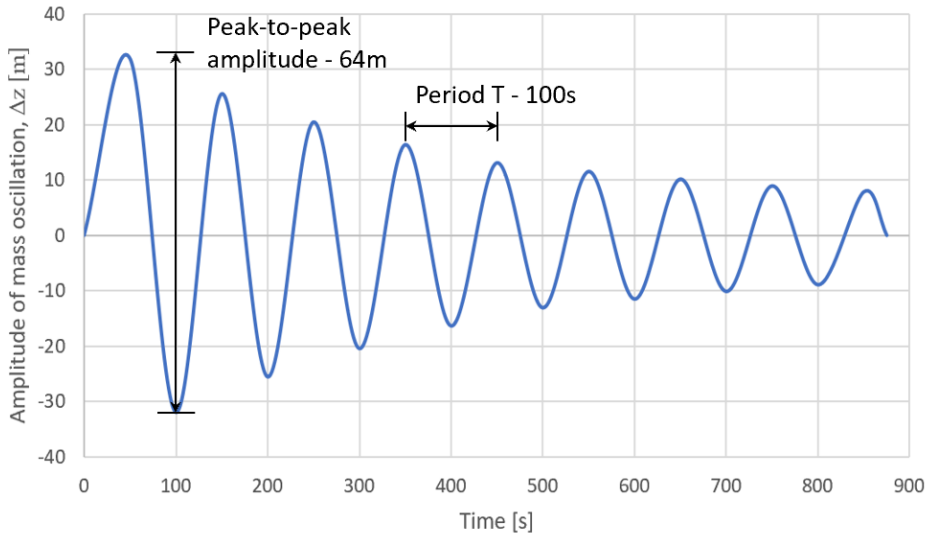
According to Dahlø et al. (1988) the frictional head loss is less than 2 m and the measured air pressure inside the ACC is approximately 2.8 MPa. The theoretical air pressure is given by the difference in water level from the reservoir to the water surface in the ACC and the head loss. The absolute air pressure is: 872.5 m - 599 m - 2 m + 10.33 m (atmospheric pressure) = 281 m  $\approx$  2.76 MPa. The measured and calculated air pressure are approximately the same and a  $h_{p0}$  of 281 m will be used. The maximum water discharge at Ulset HPP is assumed to be approximately 17 m<sup>3</sup>/s (Personal communication at Trønderenergi's offices at Lerkendal, Trondheim , 18. mars 2019).

All parameters and calculations conducted to find the amplitude and period of the mass oscillations are given in Table 5.1.

**Table 5.1:** Values used in the calculation of amplitude and period of the mass oscillations at Ulset HPP.

| Description                            | Parameter  | Value                  | Source               |
|--|------------|------------------------|----------------------|
| Maximum change in discharge            | $\Delta Q$ | 17 m <sup>3</sup> /s   | -                    |
| Sum of length / area of tunnel         | $\sum l/a$ | 293 m <sup>-1</sup>    | Appendix B           |
| Surface area of water inside ACC       | $A_0$      | 544.3 m <sup>2</sup>   | (Dahlø et al., 1988) |
| Air volume of ACC                      | $V_0$      | 3400 m <sup>3</sup>    | (Dahlø et al., 1988) |
| Polytropic index(air)                  | $n$        | 1.4                    | -                    |
| Absolute air pressure in ACC           | $h_{p0}$   | 282 m                  | (Dahlø et al., 1988) |
| Equivalent shaft area                  | $A_{eq}$   | 8.5 m <sup>2</sup>     | Equation 5.2         |
| Maximum amplitude of mass oscillations | $\Delta z$ | 32.0 m                 | Equation 5.1         |
| Period of mass oscillations            | T          | 100 s $\approx$ 1.67 m | Equation 5.3         |

Figure 5.2 illustrates the amplitude and the period of the mass oscillations. The peak-to-peak amplitude is  $2\Delta z = 64$  m. It is twice the maximum amplitude, since the pressure increase is a result of the upsurge and then the downsurge wave as was explained in Section 5.2. The amplitude decreases with time as it will be dampened out by friction along the tunnel periphery. The dampening due to friction is not of interest, since the maximum peak-to-peak amplitude is the worst case pressure increase the tunnel system might experience. It is only added in the plot for illustrative purposes.



**Figure 5.2:** Plot of the peak-to-peak amplitude and period of mass oscillation. The decrease in amplitude is a result of friction along the tunnel periphery.

### 5.3 Rendalen and Svandalsflona HPPs - Case studies

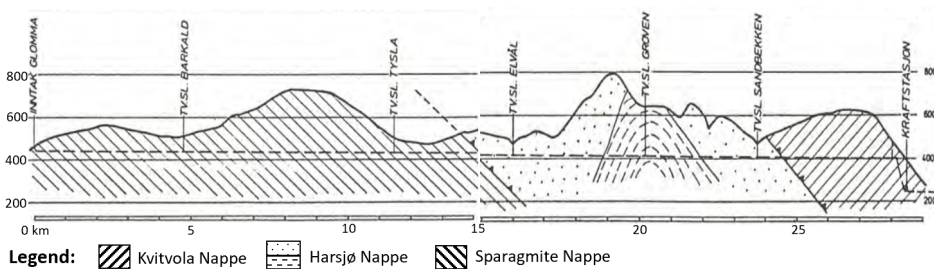
Two cases of failure in Norwegian hydropower water systems will be reviewed in the following, to take a closer look at the effects of water and pressure fluctuations in the tunnel system. The first case, Rendalen HPP, had not been subjected to hydropeaking when it was first dewatered for inspection in 1985. The second case, Svandalsflona HPP, had been subjected to the new operation scheme before the failure in 2008.

#### 5.3.1 Rendalen Hydropower Project

Rendalen hydropower project (HPP) is located by Otnes in Rendalen in Hedmark county. Water is lead from the reservoir by Høyegga through a 29 km long headrace tunnel to the outlet in the river Rena (Trønderenergi, 2019). The hydropower project was commissioned in 1971, and was continuously operated for 14 years before it was dewatered in the summer of 1985. Kjølbjerg (1985) describes the geological conditions and failures along the headrace tunnel, which will be rendered in the following.

#### Geology

The first 15 km of the tunnel runs through a grey, red sandstone (sparagmite Nappe), before passing a fault and entering the Harsjø Nappe. See Figure 5.3. The Harsjø Nappe is made up of a light quartzitic rock and changes into a darker sandstone downstream. These rocks are folded over an anticlinal consisting of a dark slate, limestone and conglomerate. The last 4 km of the tunnel is situated in the Kvitvola Nappe, where the rock is a light reddish highly bedded sandstone (sparagmite). The rock mass conditions, at the time, were characterised as the worst encountered in Norwegian hydropower history. This resulted in that approximately 46 % of the headrace tunnel had to be supported with shotcrete and 29.5 % with cast concrete lining. A total of 11 000 bolts were installed.



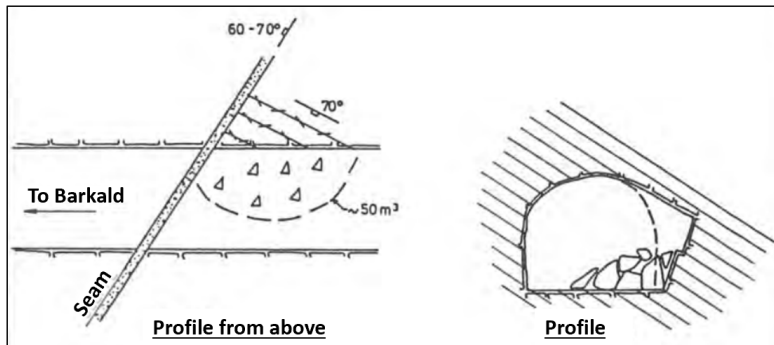
**Figure 5.3:** Geological profile along the headrace tunnel at Rendalen HPP. Water is transferred through a 29 km long headrace tunnel from the intake (inntak) in glomma to the powerhouse (kraftstasjon) area. Modified from (Kjølbjerg, 1985).

#### Tysla and Sandbekken collapses

The tunnel system was first dewatered after 14 years of continuous operations (constant water pressure), and the inspection revealed two larger collapses in addition to several block falls of size 0.5-5 m<sup>3</sup>. The total size of the block falls were estimated to 130-150 m<sup>3</sup>, which was the same as for the two larger collapses combined. All failures had fallen

during the dewatering, except from one of the larger collapses.

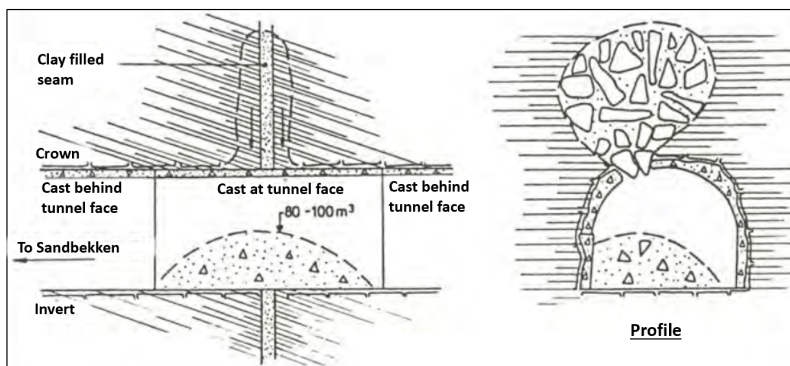
The Tysla collapse was located 2.3 km upstream of the crosscut (tv.sl) Tysla, where  $50 \text{ m}^3$  of rocks had fallen out as blocks of 3-4  $\text{m}^3$  during dewatering. The cause of the failure was a 20 cm clay filled seam which intersected the tunnel at an angle of  $45^\circ$ , see Figure 5.4



**Figure 5.4:** Illustration of the Tysla collapse. Modified from (Kjølberg, 1985).

The zone was washed out to 0.5 – 2.0 m depth. Several clay filled joints were found in the left wall downstream of collapse. The same kind of joints are believed to be the cause of the failure, from where rocks fell into the tunnel during dewatering. Further development of the failure did not seem likely, and no repair attempt was undertaken.

The Sandbekk collapse occurred 800 m downstream of the crosscut (tv.sl) Sandbekken, where a total of 80 – 100  $\text{m}^3$  of material had fallen from the crown. The material showed signs of age, as only an insignificant amount of fines could be found. The tunnel was supported by cast concrete lining, and the material had fallen through two holes which had developed in the concrete. These holes were barricaded by two larger blocks, see Figure 5.5.



**Figure 5.5:** Illustration of the sandbekken collapse. Modified from (Kjølberg, 1985).



The cast concrete lining was deformed and ruptured into smaller pieces, which was believed to be the cause of an increased load on the concrete after dewatering. When examining excavation reports after the inspection in 1985, an almost vertical clay filled zone was determined to be the cause of the collapse. The zone was described as dry in the reports. The collapse most likely happened during the first watering of the tunnel system, when the clay filled zone became water saturated. Repairs of the failed area were conducted.

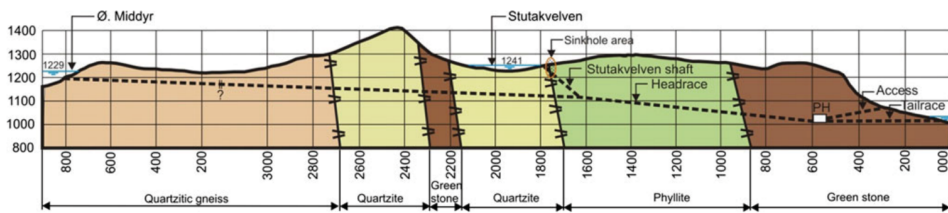
### 5.3.2 Svandalsflona Hydropower Project

In May 2008 a collapse in a weakness zone resulted in blockage of the Svandalsflona pressure shaft. During removal of deposited material at the bottom of the shaft, a sudden burst debris flood swept through the shaft which resulted in the loss of two workers. Geology of the area and investigation of the cause of the burst flood is described by Panthi (2014a). The effect pressure fluctuation might have had on the stability of the weakness zone is postulated by Neupane and Panthi (2018). A review is given in the following.

#### Project description and geology

Svandalsflona HPP is situated southwest in Norway in Hordaland county. It is part of the Røldal/Sundal hydropower scheme, and was commissioned in 1978. The project exploits a gross head of 227 m, where the water level at vestre (west) and østre (east) Middyr lake reservoirs can be regulated 40 m.

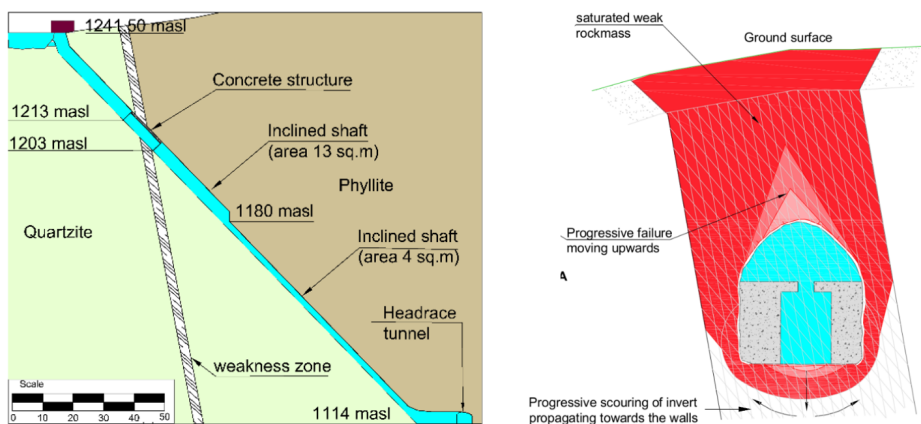
The approximately 4000 m long tunnel system passes through a complex geological set-up, see Figure 5.6. The underground powerhouse, access tunnel, tailrace tunnel and the last 900 m of the headrace tunnel are situated in greenstone and green schist of Precambrian basement rocks. The Stutakvelven shaft is intersected by the weakness zone between the quartzite and phyllite of Cambro-Silurian age, which lies between chainage 900-2750 m. A small band of greenstone has intruded the section of quartzite. The headrace tunnel runs through a quartzitic gneiss (overthrust basement rocks) upstream of chainage 2750 m (Panthi, 2014a).



**Figure 5.6:** Longitudinal profile and geology of the water system at Svandalsflona HPP. The weakness zone between the quartzite and phyllite intersects the Stutakvelven shaft, the sinkhole is indicated by a red circle (Panthi, 2014a).

### Failure of weakness zone

The Stutakvelven shaft was excavated in 1978 from bottom to the top using Alimak raise climber. When the weakness zone was reached this excavation method became too difficult, and they had to excavate the last 40 m from top to bottom by shaft sinking method. The weakness zone was highly fractured containing clay, silt and sand, and possibly highly permeable. The rock mass in the zone had very low frictional and cohesion properties, which gave the rock mass a poor self supporting capacity. The zone was supported by concrete lining in the side wall and roof, see Figure 5.7 (left).



**Figure 5.7:** Profile of Stutakvelven shaft showing the collapsed area (left) and possible failure sequence of the weakness zone and concrete support (right) (Neupane and Panthi, 2018).

The constant water flow through the shaft saturated the weakness zone and further reduced the frictional and cohesion properties of the rock. In May 2008, after almost 30 years of operations, the zone failed leading to the blockage of the Stutakvelven shaft (Panthi, 2014a).

### Pressure fluctuations

Neupane and Panthi (2018) have hypothesized how mass oscillations may have affected the weakness zone. In addition to being a brook intake, the Stutakvelven shaft acts as a surge shaft for the project. As described earlier in this chapter, this would have caused the water level in the shaft to fluctuate rapidly during mass oscillations. The starting point of failure for the weakness zone is most likely the invert and then the failure progressed to the walls. There were only a thin layer of shotcrete at the invert, and pore pressure variations from surge shafting could have caused the shotcrete to crack. Wash-outs of infilling material and opening of joints could be a result of the dynamic effect of water during mass oscillations. The change in pore pressure will cause a reduction of effective stresses, and the frequency of these changes could have destabilised rock blocks. The failure then propagated towards the walls, where the contact between the rock wall and concreted structure was lost, and the structure collapsed due to weakening of the foundation over time. The reader is referred to Neupane and Panthi (2018) for a more detailed explanation.

### 5.3.3 Lessons learned from case studies

Rendalen HPP had been operated continuously (constant water pressure) for 14 years before the dewatering in 1985. The first major failure was believed to be the Sandbekken collapse, which was a result of the saturation of a clay filled seam during the first watering of the tunnel system. According to Kjølberg (1985) the seam was not properly supported due to difficult conditions during construction. The Sandbakken collapse illustrates how the rock mass strength might be reduced from saturation, and how the first watering of a hydropower tunnel can reveal any instabilities. The Tysla collapse and many block falls show how failures can develop when the pressure the water exerts on the tunnel periphery is removed. The stability issues in the headrace tunnel at Rendalen HPP coincide with the discussion in Section 5.1.

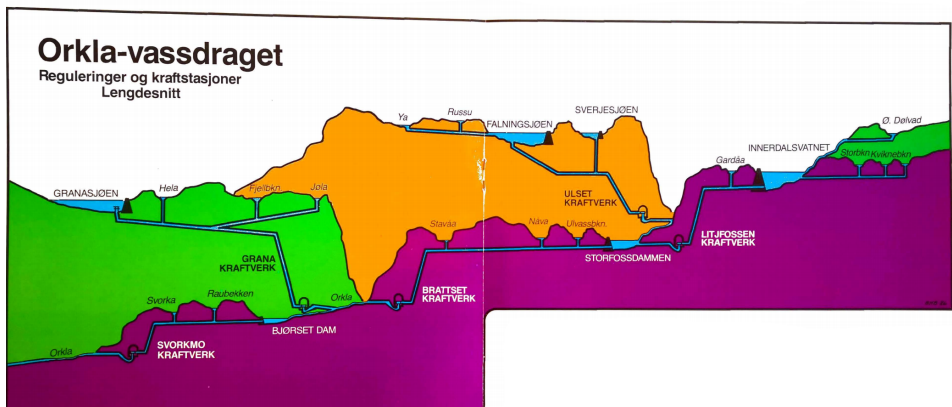
However, according to Panthi (2014a) many of the collapses in hydropower systems over the last decade happened during operation. As the rock mass conditions in unlined water tunnels change over time, the new way of operating hydropower stations (with a higher frequency of pressure fluctuations due to frequent start-and-stop sequences) may aggravate already existing instabilities and lead to failure. From the case of Svandalsfona shaft, Neupane and Panthi (2018) concluded that these pressure fluctuations might have a significant impact on the long-term stability of unlined water tunnels, but further research is necessary to understand the interaction between pressure fluctuations in hydropower tunnels and the response of the rock mass.

The effect water has on the rock mass and the destabilising effect pressure fluctuations might have on water tunnels will be further studied at Ulset HPP, which will be presented in the next chapter.

# Ulset Hydropower Project

## 6.1 Project description and layout

Ulset Hydropower project (HPP) is part of a system of five hydropower projects along the Orkla river system, see Figure 6.1. Ulset HPP started its operations in 1985, and the daily operations are controlled by TrønderEnergi. The annual production is 140 GWh. It was developed by KVO (Kraftverkene i Orkla), and is located in Tynset municipality north in Hedmark county. Statkraft owns 48.6 % of KVO, together with TrønderEnergi Kraft (35 %), Eidsiva (12 %) and NØK (4.4 %) (Trønderenergi, 2018).



**Figure 6.1:** Overview of the five hydropower projects along Orkla river. Ulset is located highest up in the river system followed by Litjfosse, Brattset, Grana and Sverkmo Hydropower plant (Eiken et al., 1986).

### 6.1.1 Falningsjøen and Sverjesjøen - Intake areas

Water is retrieved from two intake areas at Ulset HPP, Falningsjøen and Sverjesjøen reservoirs, and from the rivers Ya and Russa. Falningsjøen is the main reservoir and is raised 25.5 m by an embankment dam with an impervious core of moraine material. The river Ya is transferred to Falningsjøen through a tunnel, and the side river Russa is connected to this tunnel through a shaft (Eiken et al., 1986). The water elevation at Falningsjøen can be regulated between 872.5 m and 825.0 masl, yielding a storage capacity of 125 million m<sup>3</sup> of water (Trønderenergi, 2018).



**Figure 6.2:** Falningsjøen embankment dam seen from the reservoir on the left side.

Sverjesjøen is raised 4.8 m, between 872.5 and 867.5 masl, by a concrete buttress dam as can be seen in Figure 6.3. This gives the reservoir a storage capacity of 7 million m<sup>3</sup> (Eiken et al., 1986). Water is led to the headrace tunnel through a 60° steep shaft. Sverjesjøen intake functions as a submerged intake when the water elevation in Falningsjøen exceeds 867.7 masl. It acts as a brook intake when the water elevation at Falningsjøen drops below 867.7 masl (Dahlø et al., 1988).



**Figure 6.3:** Sverjesjøen buttress dam seen from the right side of the reservoir.



### 6.1.2 Headrace tunnel

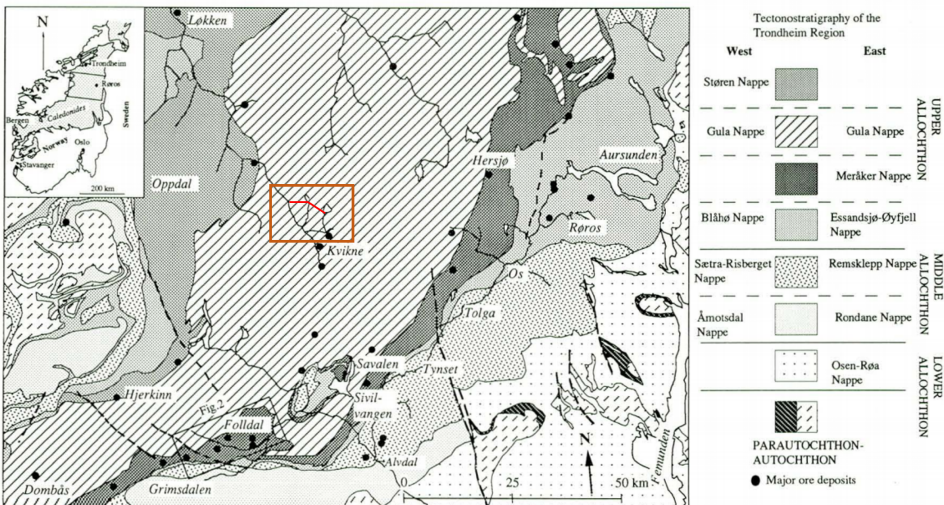
The total length of the headrace tunnel is 7.6 km. The first 2439 m were excavated by drill and blast with an approximate area of 22 m<sup>2</sup>. The last 1629 m of this part of the tunnel have an inclination of 12° and an alignment of N293E. A 65 m long sand trap is located at the end of the drill and blast section. The next 4877 m were excavated by a 4.5 m diameter (15.9 m<sup>2</sup>) tunnel boring machine (TBM), with an inclination of 0.5° and alignment of N273E. The last 325 m of the headrace tunnel, before the steel lined pressure tunnel, were again excavated through drill and blast (Dahlø et al., 1988).

## 6.2 Engineering geological setting

The engineering geological conditions along the headrace tunnel at Ulset HPP have been investigated through desk study and field work. Field observations and an engineering geological map of the project area with field locations, can be found in Appendix A. The findings will be presented below. A longitudinal profile over the project layout and geology can be found in Appendix B.

### 6.2.1 Geology of project

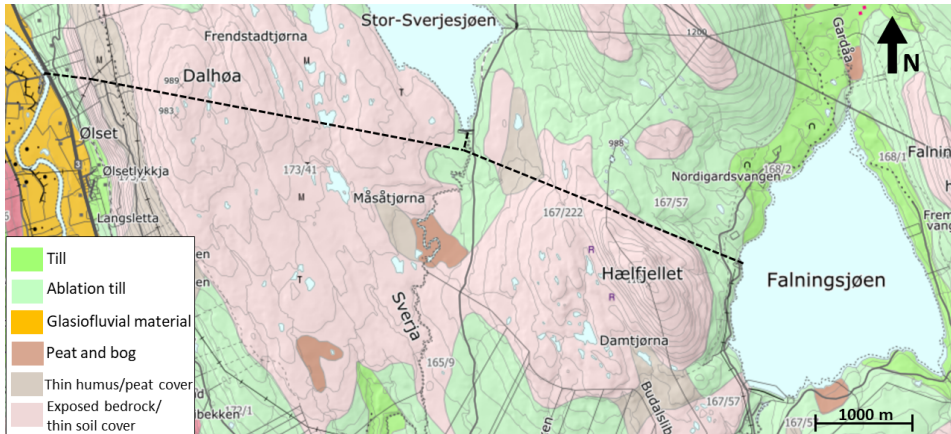
Ulset HPP is located in the central part of the Scandinavian Caledonides in the southern Trondheim Region, see Figure 6.4. The Caledonian mountain range was a result of a continent-continent collision between Laurentia and Baltica, and it extends from Rogaland in the southwest of Norway to Finnmark county. It is composed of bedrock overlaid by allochthons, which are thrust sheets from the formation of the Caledonides. Ulset HPP can be found in the upper allochthon in the Gula Nappe (Nilsen and Wolff, 1989).



**Figure 6.4:** Stratigraphic map of southern part of the Trondheim Region. The project area is located within the orange rectangle north of Kvikne in the Gula Nappe. The red line illustrates the headrace tunnel of Ulset HPP. Modified from (Bjerkegård and Bjørlykke, 1994; Nilsen, 1988).

### Quaternary geology

Figure 6.5 shows the quaternary geology of the project area, where the bedrock is sparsely covered with till deposits. Small lakes and peat bogs occupy some depressions in the landscape, which can be an indication of a watertable close to the groundsurface. The area shows signs of northwestward glacial movements, and deposits of glasiofluvial materials can be found along the Orkla river.



**Figure 6.5:** Quaternary geological map of project area. The dotted black line represents the tunnel system. Modified from NGU (2019).

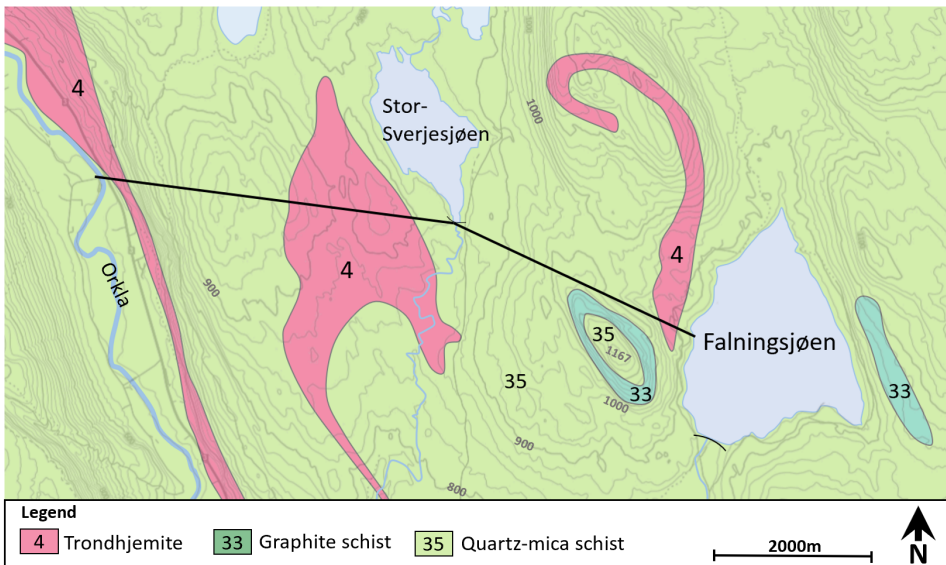
Lineaments in the terrain with a trend of N140-160°E have been found through inspection of 3D maps from *Norge i bilder* (Kartverket, n.d.).

### Rock types

According to Nilsen and Wolff (1989) there are three rock types in the project area, a massive quartz-mica schist, graphite schist and intrusions of trondhjemite, as can be seen in Figure 6.6. During field mapping two of these rocks were encountered. From laboratory investigations presented in Chapter 7 the quartz-mica schist has been determined to be a quartzitic schist based on the high content of quartz. However, there are observed some variations in the quartzitic schist from Falningsjøen towards the powerhouse area.

#### *Quartzitic schists*

By Falningsjøen the quartzitic schist is observed along road cuts and by the access tunnel. Here the rock mass has only been exposed to the elements since 1980, and appears massive and medium strong. The rock mass is grey in colour and has a brown/red coating. It is fine grained with a distinct foliation. Towards Falningsjøen and the powerhouse area the quartzitic schist is more weathered, with an even more distinct schistosity. The difference can be seen in Figure 6.7.



**Figure 6.6:** Geological map of the project area. The black line represents the water system at Ulset HPP. Re-produced from Nilsen and Wolff (1989).

The quartzitic schist by the powerhouse area is referred to by Dahlø et al. (1988) as a mica gneiss.



**Figure 6.7:** Quartzitic schist by Falningsjøen at location 1 (left) and more weathered with schistosity at location 8 by Sverjesjøen (right).



### *Trondhjemite*

The trondhjemite was easily distinguished from the quartzitic schist by the light color and massive appearance. It has a white or beige color with medium coarse grains.



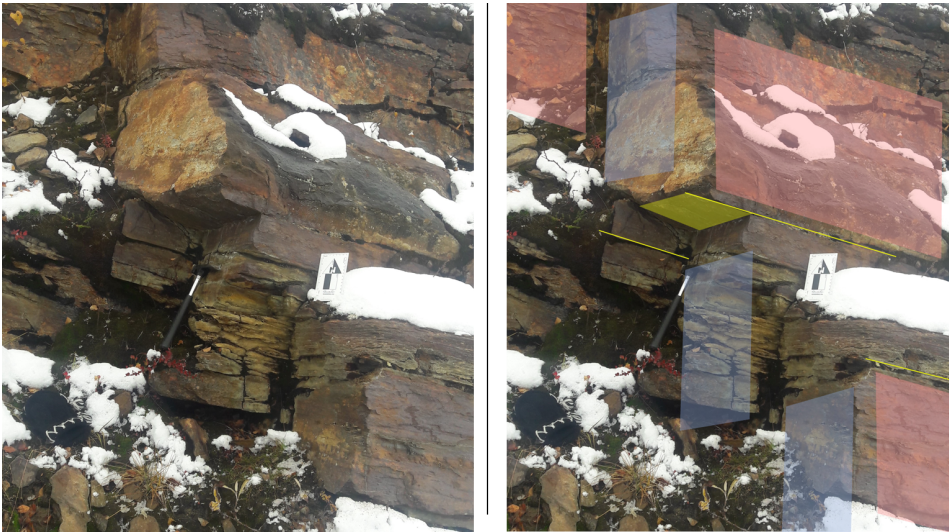
**Figure 6.8:** Trondhjemite over quartzitic schist at location 7 Sverjesjøen (left) and 14 powerhouse area (right). The trondhjemites are from different intrusions.

## 6.2.2 Jointing

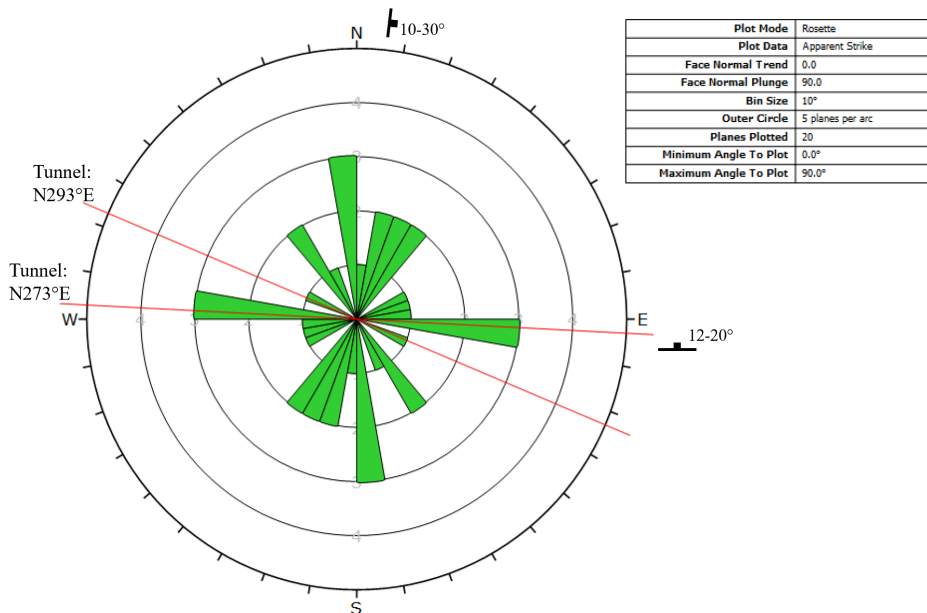
Joint measurements have been carried out during field mapping, and in the headrace tunnel by SINTEF in connection with the tunnel excavation and a tunnel inspection in 1986.

The quartzitic schist by Falningsjøen has a distinct foliation, and joints have developed along the foliation planes. These joints can be seen in Figure 6.9 as yellow planes. The average strike/dip is N098°E/16°N, and the general spacing is 0.5 - 1 m. The joint planes are irregular and undulating. In addition to the foliation joints, two other joint sets were observed (red and blue). In Figure 5.4 the joints illustrated with blue planes had a strike/dip of N105E/70S and the red N047E/82SE. These had a smooth undulating surface with spacing of 0.3 - 0.7 m.

The foliation is almost horizontal and changes through the project area. All foliation joint measurements are given in the rosette plot in Figure 6.10. In general the foliation dips towards north by Falningsjøen and changes to east at Sverjesjøen. The change in dip is believed to be from folding during the orogeny.

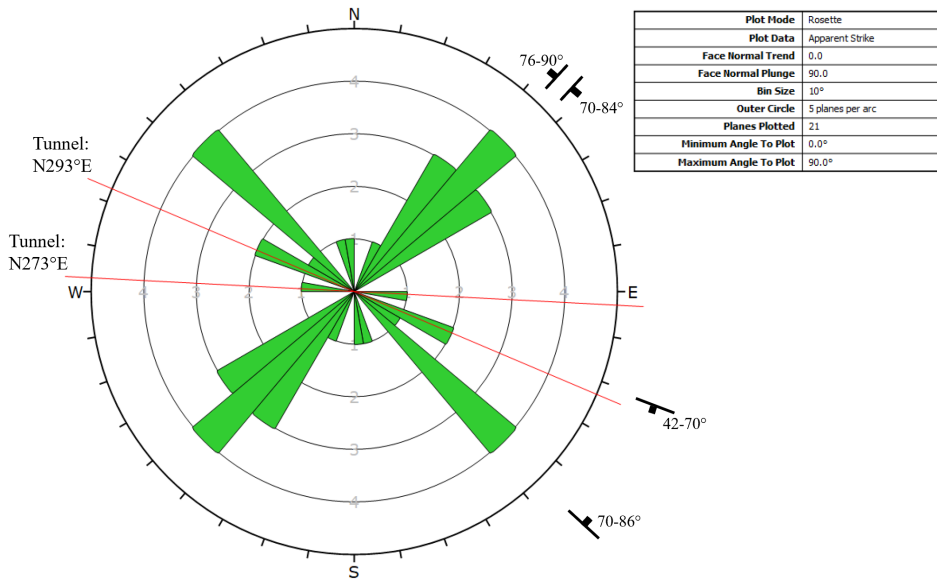


**Figure 6.9:** Grey quartzitic schist by Falningsjøen, with a brown/red coating. To the right the joint planes are illustrated with colour: foliation joints (yellow) and crossjoints (red and blue).

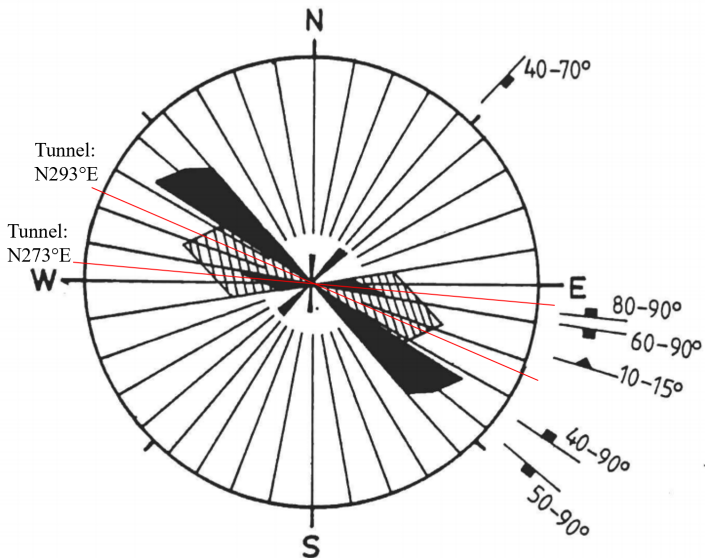


**Figure 6.10:** Rosette plot of foliation joints from the project area.

The rosette plot of the cross joint measurements from field work are presented in Figure 6.11. Joint measurements from the headracetunnel can be found in Figure 6.12.



**Figure 6.11:** Rosette plot of cross joint measurements from the project area.



**Figure 6.12:** Rosette plot of joint measurements from the headrace tunnel. The solid black represents cross joints, while the striped area represents foliation (Modified from (Dahlø et al., 1988)).

In addition to the foliation joints, the jointing at Ulset HPP can be divided into the following joint sets:

1. The dominant joint set in the last part of the headrace tunnel is oriented N120-145E with a steep dip, normally to the NE. Some clay filling occurs, and most water leakage follow this joint set (Dahlø et al., 1988).
2. The dominant joint set at the surface is oriented N040-050E with a steep dip to SE and NW.
3. Joints oriented N80-105E tend to occur, with a dip of 40-90 ° mostly to the south.

### 6.2.3 Rock mass conditions

Q-values were estimated at three different locations and calculated after Equation 4.9. They are given in Table 6.1. The rock mass quality description was found from Appendix A.2. The parameters were given a value after the table with input values for the Q-system given in Appendix A.3 during field mapping.

**Table 6.1:** Estimated Q-values for rock units during field mapping

| <b>Location</b>      | 1           | 7           | 14           |
|----------------------|-------------|-------------|--------------|
| <b>Rock type</b>     | Mica schist | Mica schist | Trondhjemite |
| <b>RQD</b>           | 80-90       | 10          | 90-100       |
| <b>J<sub>n</sub></b> | 9           | 3           | 4            |
| <b>J<sub>r</sub></b> | 3           | 1.5         | 3            |
| <b>J<sub>a</sub></b> | 4           | 1           | 2            |
| <b>J<sub>w</sub></b> | 1           | 1           | 1            |
| <b>SRF</b>           | 1           | 1           | 1            |
| <b>Q-value</b>       | 6.67-7.5    | 5           | 33.8-37.5    |
| <b>Description</b>   | Fair        | Fair        | Good         |

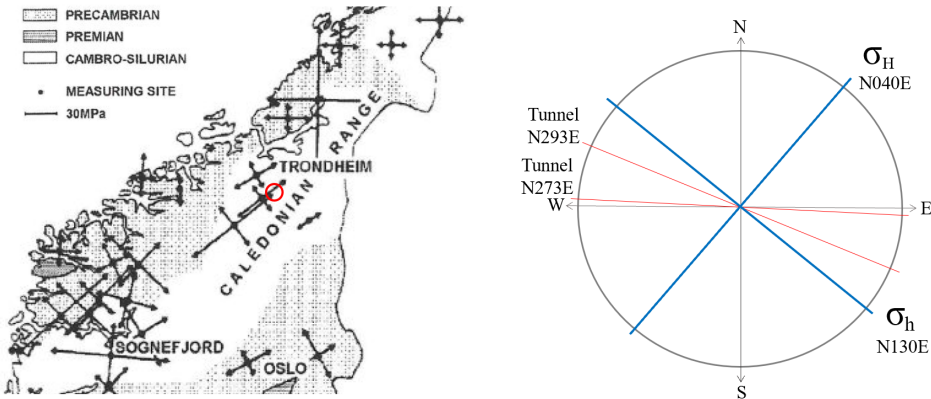
### 6.2.4 In situ rock stress conditions

There are not performed any stress measurements or hydraulic fracturing test in connection with the excavation of Ulset HPP. The closest known measurements are conducted in connection with the air cushion chamber at Brattset HPP. Here, both a hydraulic splitting test and 3D overcoring tests were preformed (Hansen and Hanssen, 1988). The measured values are given in Table 6.2.

**Table 6.2:** Average in-situ stresses and shut-in pressure from measurements performed at Brattset HPP (Hansen and Hanssen, 1988).

| Measured stress/pressure | Value [MPa] |
|--------------------------|-------------|
| $\sigma_v$               | 5.7         |
| $\sigma_1$               | 15.6        |
| $\sigma_2$               | 6.1         |
| $\sigma_3$               | 2.7         |
| $P_s$ (shut-in pressure) | 5.1         |

As there are no information about the direction of the measured stresses, the orientation in the stress map of Norway given by Myrvang (2001) will be adopted. Figure 6.13 shows the location of Ulset HPP with a red circle, and the assumed direction of the major and minor principal stresses together with the tunnel alignments.



**Figure 6.13:** Orientation of the horizontal in-situ stresses in Norway, with the location of Ulset HPP marked by a red circle (left, modified after (Myrvang, 2001)). Orientation of the major and minor principal stresses together with the tunnel alignments (right).

In addition a high tectonic stress axis dipping towards N060W has been suggested, based on observations of spalling in the powerhouse cavern (Dahlø et al., 1988). The powerhouse area is close to the valley side, which indicates that the horizontal stresses are affected by the topography. There is also observed high shear stress along the foliation plane. According to Dahlø et al. (1988) the quartzitic schist is relatively impermeable. However, the northwest trending fracture system can be water conducting in areas of low confinement. These fractures were water bearing up to 190 m from the penstock, but dry after a distance of 340m.

### 6.2.5 Installed support

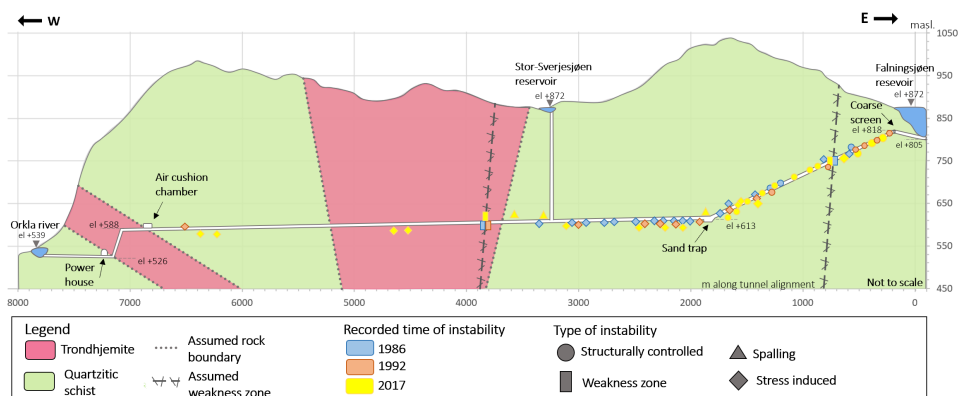
The installed support in the headrace tunnel corresponds to the Norwegian support philosophy. The tunnel is unlined with support only applied during excavation in areas of instability. In the drill-and-blast part of the tunnel there is 20 m with cast concrete lining and 30 m with shotcrete. Locally there are distances with three to four rock bolts per m. The tunnel above the sand trap is systematically bolted, to avoid fallout of rocks during excavation of the trap. For the TBM excavated tunnel there are 25 m with shotcrete, 35 m locally bolted. Steel straps have in some areas been used in addition with the shotcrete and bolts. The pressure tunnel differs from other Norwegian pressure tunnels, as it is steel lined (Dahlø et al., 1988).

## 6.3 Instabilities along the headrace tunnel

During the inspection of the headrace tunnel in 2017, many small to medium scale block falls and small collapses were observed. A timeline of the registered failures have been made and the different failures have been systematised into different categories, which are given in the following.

### 6.3.1 Timeline

Two tunnel inspection reports by Bardal and Bruland (1986) and Forodden (1992), together with notes and pictures from Neupane (2017) and notes from Midtlyng (2017), have been used in the identification of the different failures and instabilities in the headrace tunnel. A timeline of registered failures, based on the inspection reports, is presented in Figure 6.14. A larger example of the figure can be found in Appendix C, together with a list of all the failures. The place and time are approximate, as there are discrepancies in the numbering of niches in the different reports. The mechanisms behind the failures are interpreted from pictures and simple notes, therefore some interpretations might be wrong.



**Figure 6.14:** Overview and timeline of the different instabilities/failures in the headrace tunnel. The different shapes represents the failure category and the colours represent the year the failure was registered.

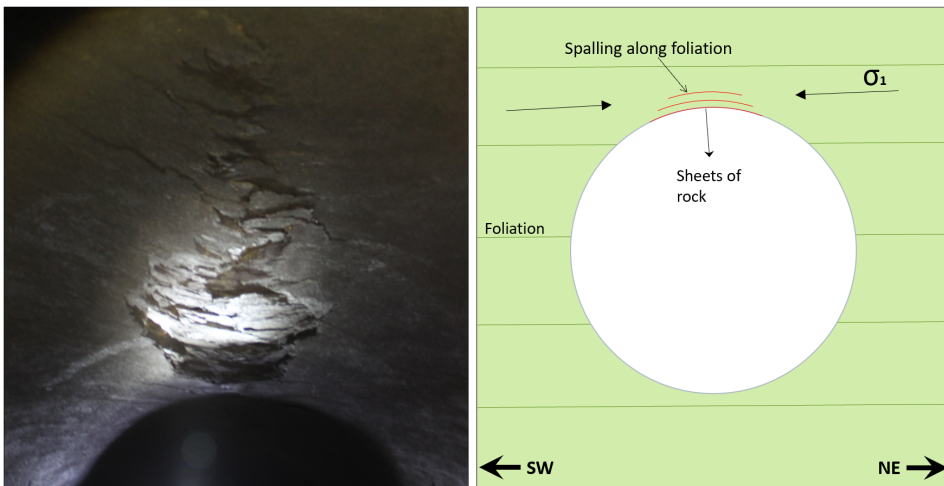


In Figure 6.14 the years of registered failures are presented with blue (1986), orange (1992) and yellow (2017) colours. The failures have been systematised into four categories:

- Spalling (triangle)
- Stressed induced (square)
- Structurally controlled (circle)
- Weakness zone (rectangle)

### 6.3.2 Spalling

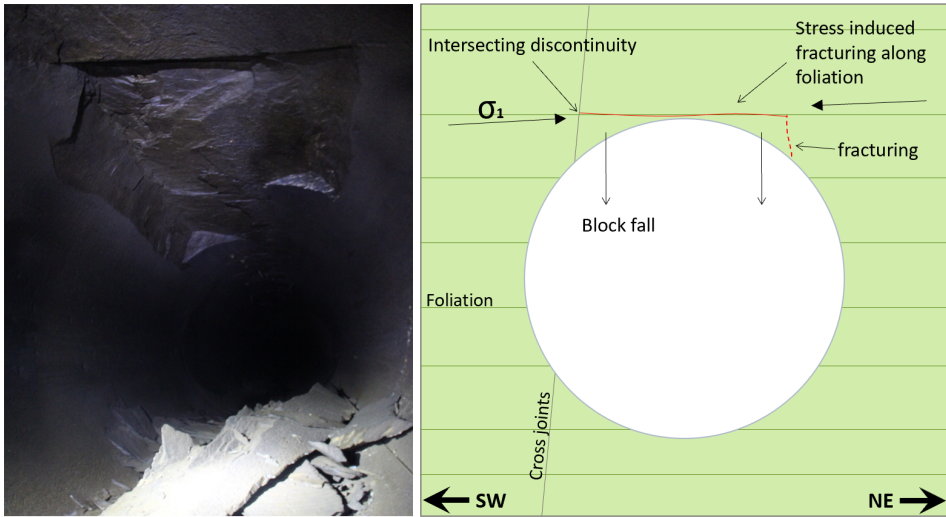
Slight spalling can be found in the roof downstream of the Stor-Sverjesjøen shaft and in the roof above the sand trap. No reports of spalling prior to the inspection in 2017 have been found in these locations. It can therefore be assumed that a decrease in the rock mass strength has taken place since the commission in 1985, causing the spalling. If the spalling develops further into the rock mass more severe instabilities can take place.



**Figure 6.15:** Spalling in the roof of the TBM tunnel at approximately 400 m downstream of the Stor-Sverjesjøen shaft (left), caused by high rock stresses parallel with the foliation (right).

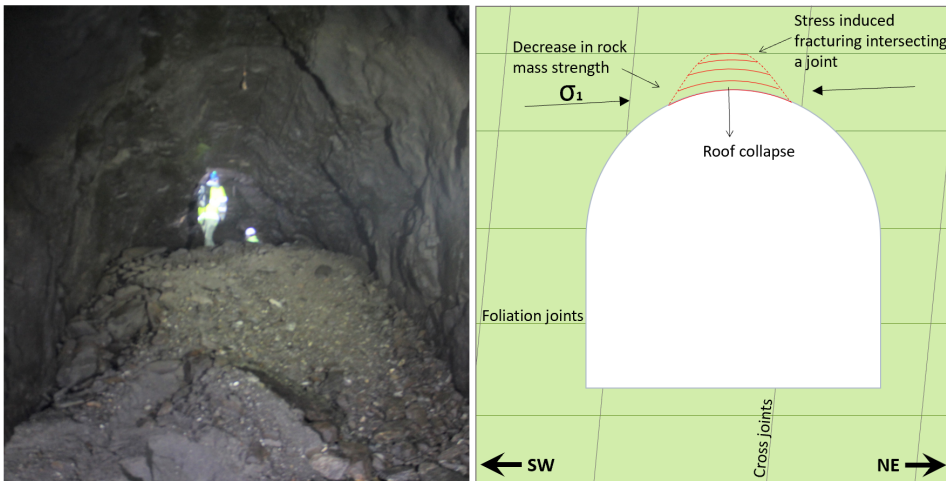
### 6.3.3 Stress induced failure

The reported failures from (Bardal and Bruland, 1986) share the same characteristic shape, long thin flakes or sheets. They occur all along the tunnel alignment from the coarse sediment screen to the second intake (shaft at Sverjesjøen), but are more distinct in the TBM tunnel. Notches are left in the roof as can be seen in Figure 6.16. The major stress induced fractures are along the foliation plane, which either intersect a joint causing block fall, or the weight of the block leads to fracturing of the rock bridge and eventually block fall.



**Figure 6.16:** Notches left in the roof from stress induced failure at 2585 m from the coarse sediment screen (left).

Stress induced failure is also believed to be the cause of some small scale collapses in the D&B tunnel, Figure 6.17. The spalling/induced fracturing propagated into the rock mass, as explained in Section 4.3.2, due to a decrease in the rock mass strength from saturation and weathering effect of water. The induced fracturing eventually intersected a weak discontinuity and failed.

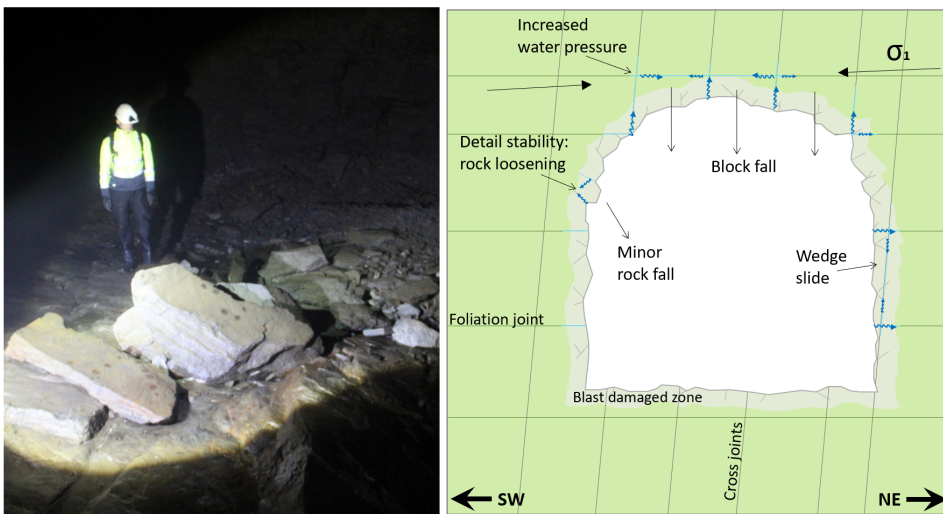


**Figure 6.17:** Material from roof collapse causing sediment to be deposited, which leads smaller and medium scale blockages in the D&B tunnel (left). Fracturing induced by high stresses propagates into the rock mass, as the rock mass strength decreases, finally intersecting a foliation joint causing a roof collapse (right).



### 6.3.4 Structurally controlled failure

The larger ( $>0.1\text{m}^3$ ) structurally controlled failures, block fall and slide from roof and walls, are plotted in Figure 6.14. The fallen blocks have a characteristic shape as seen in Figure 6.18. They are a result of horizontal foliation joints and cross joints, which divide the rock mass into rectangular blocks. In the walls smaller and larger wedges, often thin and long in shape, have slid along the almost vertical cross joints. Reduction in shear strength of the joints and an increased water pressure (possibly from mass oscillations) could be reason for the block and wedge failures.



**Figure 6.18:** Block fall at 229 m downstream of the coarse sediment screen (left).

Smaller rock falls in the D&B tunnel are very common, and the frequency of smaller and larger rock falls seems to increase over the last decades. The smaller rock falls are a result of failure in the detail stability, as the contour of a D&B tunnel are damaged from blasting leaving a rougher surface.

### 6.3.5 Weakness zone

Approximately 600 m downstream of the Sverjesjøen shaft is a distinct zone in the rock mass. The zone is 1 - 1.5 m in length and consists of crushed rock. It differs from the side rock which is more massive, as can be seen in Figure 6.19. According to Bardal and Bruland (1986) this zone is small, almost vertical and strikes the tunnel with an angle of  $45^\circ$ . This gives the zone a strike of N140E which corresponds to lineaments at the surface. At the time they concluded that zone did not cause any stability issues, as there were only some fallout from the zone.



**Figure 6.19:** Weakness zone in the headrace tunnel 650 m downstream of the Sverjesjøen shaft.

The red dotted lines in Figure 6.20 illustrate lineaments found in the surface terrain. The red line corresponds to the weakness zone described above. The red line to the right illustrates another distinct lineament which cuts the tunnel. At this location the tunnel is supported by a cast concrete lining. Material from behind the concrete have in some areas been washed away, indicating that the material had to be crushed or fragmented which is common for weakness zones.



**Figure 6.20:** Black line illustrates the tunnel system and the red dotted lines represent possible weakness zones found in the tunnel.



## Laboratory Work

Rock mechanical testing was carried out by Gunnar Vistnes and the author, except for the tilt-test which Bibek Neupane and the author conducted. Laurentius Tjihuis and the author performed the XRD-analysis.

The method applied and results from the laboratory testing will be presented in this chapter. The rock mechanical testing is performed according to ISMR's suggested methods, and the reader is referred to these for theory.

### 7.1 Rock samples

Two rock samples, quartzitic schist and trondhjemite, were collected during field work for testing. Both samples can be seen in Figure 7.1.



**Figure 7.1:** Rock core extraction from the quartzitic schist (left) and trondhjemite (right) samples.

The quartzitic schist sample was found by the access tunnel at Falningsjøen, marked as location 1 in the engineering geological map in Appendix A. The trondhjemite was collected from the access tunnel by the powerhouse area at location 14. The schist sample had a red coating, but the proper color of the rock can be seen in the grey bore water. When boring cores from the quartzitic schist some of the cores were divided into parts, because of a few weak foliation layers in the samples. The trondhjemite sample was rounded, and there was a slight discoloring of the trondhjemite approximately two centimeters into the cores from the surface layer. Both samples had indications of weathering, which can have an impact on the test results.

## 7.2 Density and velocity

The 10 rock cores prepared for UCS testing were first measured and weighed. The density  $\rho$  was then calculated from Equation 7.1, where  $m$  is weight of rock specimen and  $V$  is the volume.

$$\rho = \frac{m}{V} \quad (7.1)$$

The sound velocity was found by sending high frequency waves through the rock cores with an apparatus called Pundit. The travel time for each core was registered and the simple relationship given in Equation 7.2 was used to find the velocity  $v$ .

$$v = \frac{s}{t} \quad (7.2)$$

The travel time and weight were first determined on dry rock cores, before being found again after submerging the cores in water for 7 days. All measurements and results are given in Appendix D. The mean values together with standard deviations are listed in Table 7.1.

**Table 7.1:** Results from density and sound velocity tests given in mean values with standard deviation.

| Rock type         | Density<br>[g/cm <sup>3</sup> ] | Velocity<br>[m/s] |                 |
|-------------------|---------------------------------|-------------------|-----------------|
|                   |                                 | Unsaturated       | Water saturated |
| Quartzitic schist | 2.69 ± 0.01                     | 4265 ± 251        | 5193 ± 104      |
| Trondhjemite      | 2.62 ± 0.003                    | 3519 ± 41         | 5272 ± 53       |

## 7.3 Uniaxial compression test

A uniaxial compression test (UCS-test) was performed to find the strength and deformability of the rocks (ISRM, 1979). The rock cores were bored perpendicular to the foliation plane in the quartzitic schist. No clear foliation could be seen in the trondhjemite sample,

but after preparation a slight foliation could be seen in the rock cores. The foliation had an approximate angle of  $36^\circ$  to the core axis.

The test was carried out with a GCTS Rapid Triaxial Test System (RTR-4000) on five rock cores of each rock type. The rock cores had an approximately 40.5 mm diameter and 105 mm length. The applied pressure from the RTR-4000 was controlled by a constant strain velocity. For the quartzitic schist the strain velocity was -300 mstrain/min and -800 mstrain/min for the Trondhjemite. The axial and radial deformations were registered. The uniaxial compressive strength  $\sigma_{ci}$ , Young's modulus  $E$  and Poisson's ratio  $\nu$  were calculated by software and are given in Appendix D, together with the stress-strain curves. The post peak behaviour after yielding is removed in these curves. The mean values together with standard deviation are given in Table 7.2. Since the test was performed on cores with diameter 40.5 mm Equation 3.3 is used to find the corresponding strength for cores of 50 mm, which is the recommended size of test samples.

**Table 7.2:** Mean values together with standard deviation for uniaxial compressive strength, Young's modulus and Poisson's ratio.

| Rock type                   | Average $\pm$ standard deviation    |                       |                 |
|-----------------------------|-------------------------------------|-----------------------|-----------------|
|                             | Uniaxial compressive strength [MPa] | Young's modulus [GPa] | Poisson's ratio |
| Quartzitic schist (40.5 mm) | $189 \pm 31.2$                      | $51.8 \pm 4.8$        | $0.27 \pm 0.03$ |
| Trondhjemite (40.5 mm)      | $179 \pm 3.0$                       | $57.1 \pm 1.1$        | $0.41 \pm 0.02$ |
| Quartzitic schist (50 mm)   | 182                                 | -                     | -               |
| Trondhjemite (50 mm)        | 173                                 | -                     | -               |

According to ISRM (1977) a uniaxial compressive strength between 100 - 250 MPa is that of a very strong rock. Both the quartzitic schist and the trondhjemite can be found in this range. Two of the quartzitic schist cores failed in shear, with an approximate mean failure angle of  $26^\circ$ . The other three cores seemed to fail in a manner of axial extension fracture, which is normal for hard and brittle rocks (Li, 2017b). There were no clear failure planes in the trondhjemite cores after testing. Rather the cores had been crushed, indicating a very brittle rock.

The Poisson's ratio for the trondhjemite is very high, and can be found at another place on the stress-strain curve (Appendix D) for a lower number.

## 7.4 Point load index test

The point load index test can be used for classification of a rock material's strength, by the point load index  $I_s$ . It can also give an indication of the anisotropy of a rock through the Strength anisotropy Index  $I_{s(50)}$  (ISRM, 1985).

Rock cores were loaded until failure in a GCTS Point Load Tester (Enerpac PLT-100), with a constant increase in load of 0.2 kN/s. A total of 44 tests were performed on the

quartzitic schist, 18 of these were conducted diametrically (parallel with the foliation) and the rest axially (perpendicular to the foliation). Only five diametral tests and one axial test were performed on the trondhjemite. This was due to a slight foliation in the rock cores where the failure plane formed along, which left too few cores to perform the test on.

All test results and calculations according to ISRM (1985) are given in Appendix D. The mean diametral and axial point load indexes are given in Table 7.3 together with the standard deviation.

**Table 7.3:** Results from point load index test with mean size-corrected values and anisotropy index. \*Trondhjemite values are not valid due to too few test samples.

| Rock Type         | Mean ± Std.dev.    |                |                     |
|-------------------|--------------------|----------------|---------------------|
|                   | Diametral<br>[MPa] | Axial<br>[MPa] | Anisotropy<br>index |
| Quartzitic schist | 4.3 ± 0.6          | 11.4 ± 1.5     | 2.64                |
| Trondhjemite      | 7.7 ± 1.3*         | 5.5*           | 1.39*               |

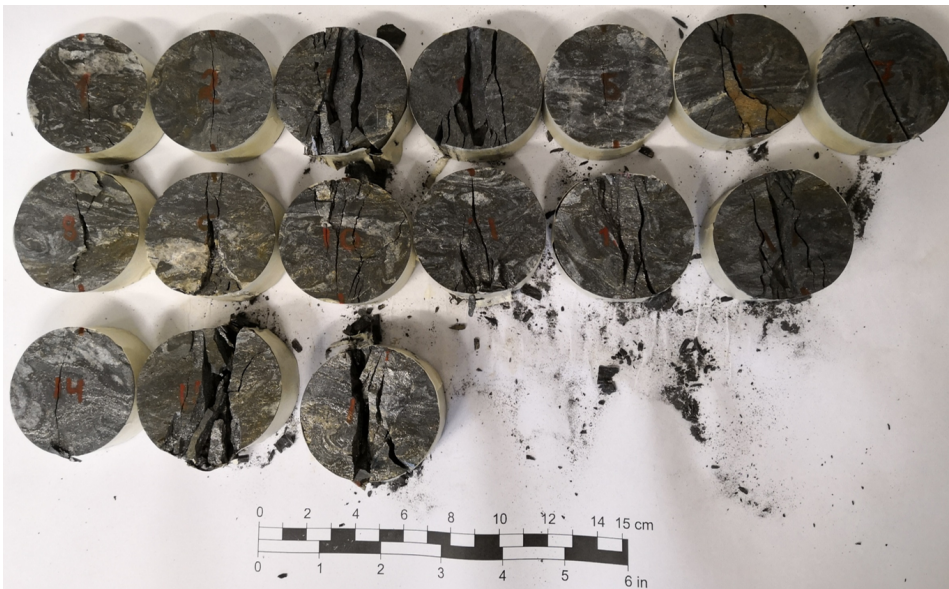
The result for the testing on the trondhjemite is included, even though it is not valid. This is to show that there is some anisotropy in the trondhjemite. The quartzitic schist is highly anisotropic, and is very strong normal to the foliation plane.

## 7.5 Brazilian test

Another rock mechanical parameter of interest is the tensile strength, which can be determined indirectly by the Brazilian test. The test and calculations were performed according to ISRM (1978).

Disc formed test samples with a diameter of approximately 50 mm and thickness half of the diameter were prepared. These were placed in a GCTS Point Load Tester (Enerpac PLT-1000), where the two spherically truncated conical platens for the point load test were replaced with two steel loading jaws. A pressure of 0.2kN/s was applied manually until failure. The quartzitic schist failed in an explosive manner, leaving crushed rock discs and finer particles as seen in Figure 7.2. This indicates a remarkably strong rock.





**Figure 7.2:** The disc formed test samples after failure, the quartzitic schist samples failed in a explosive manner.

A total of 16 tests were carried out for the schist and 15 for the trondhemite. Only one test for each rock type was not valid. The measured values, calculations and results can be found in Appendix D. The average tensile strengths and deviations are listed in Table 7.4.

**Table 7.4:** Results for the Brazilian test with average tensile strength and standard deviation.

| Rock type   | Tensile strength, $\sigma_t$ |
|-------------|------------------------------|
| Mica schist | $20.6 \pm 3.9$               |
| Trondhemite | $9.9 \pm 1.15$               |

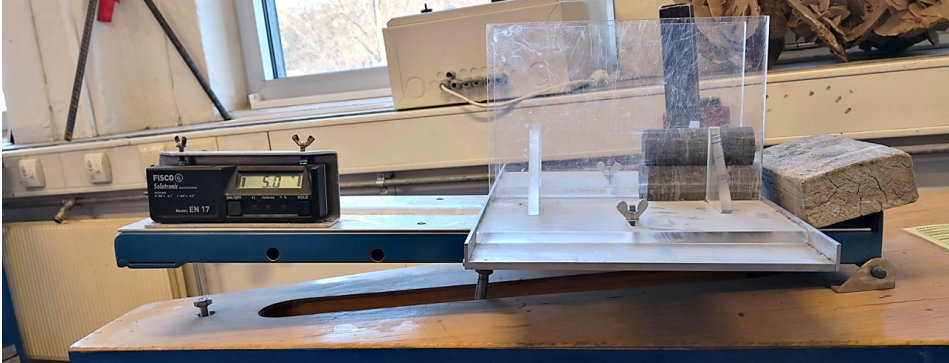
The rock cores used were bored normal to the foliation, which means that the tensile strength were tested normal as well. Probably will the tensile strength parallel with the foliation be lower.

## 7.6 Tilt test

The basic friction angle is an important parameter in estimating the shear strength of discontinuities. It can be found through tilt testing. The procedure followed is proposed by Alejano et al. (2018), where five tilt test are recommended for each specimen. To get a more correct value, the tilt test was performed 12 times for every core. The equation for the basic friction angle had to be changed accordingly.



The tilt-test arrangement used was the three-core-set-up, as can be seen in Figure 7.3. The cores were first used for the tilt-testing before the UCS-test. The see-through walls fastened the two bottom cores, while the one on the top could move freely. The tilting table was operated through compressed air, and the inclination was increased until the top core slipped. The inclination was registered manually and noted. The procedure was performed 12 times on each core, three times on four sides of the cores.



**Figure 7.3:** Apparatus used in the tilt testing. The cores slide less than 10% of the length onto a wood plank to minimise the wear of the rock surface.

The equation used for calculating the median basic friction angle for the three-core-set-up can be found in (Alejano et al., 2018). All measurements and calculations can be found in Appendix D, while the median basic friction angles with the variation for each core are listed in Table 7.5.

**Table 7.5:** The median basic friction angle for quartzitic schist and trondhjemite with variation.

| Rock type         | Core number | Median basic friction  | Variation in basic              |
|-------------------|-------------|------------------------|---------------------------------|
|                   |             | angle, $\phi_b$<br>[°] | friction angle, $\phi_b$<br>[°] |
| Quartzitic schist | 3           | 25.7                   | 24.4-27.5                       |
|                   | 4           | 27.4                   | 23.6-29.9                       |
|                   | 5           | 26.3                   | 24.3-27.8                       |
| Trondhjemite      | 1           | 29.4                   | 27.8-30.5                       |
|                   | 2           | 29.3                   | 27.7-30.8                       |
|                   | 3           | 28.3                   | 27.0-31.1                       |

## 7.7 XRD

The X-ray diffraction method (XRD) is used to determine the mineralogy of rocks. It is based on the diffraction of X-ray waves on a mineral's crystal lattice. For theory behind the method the reader is referred to (Lavina et al., 2014).

XRD-analysis was performed on the quartzitic schist, trondhjemite and a red substance. The red substance accumulated in the water used to saturate the schist samples (Figure 7.4). The same kind of substance is believed to be found on joint surfaces and as a coating on the rock mass described in Section 6.2.1.



**Figure 7.4:** Red substance accumulated in water used to saturate the test samples(left). The same red substance was found on a weak plane which divided the rock cores during drilling.

Representative rock pieces were grounded into a fine powder, and together with the red substance, placed into three sample holders. The samples were then placed in the X-ray apparatus. The intensity of the diffracted waves are recorded and a XRD-plot is the result. By comparing peak positions in the XRD-plots with reference patterns the mineral compositions was found. The plots can be found in Appendix D. The mineralogical content of the quartzitic schist and trondhjemite is given in Table 7.6 and 7.7.

**Table 7.6:** Mineralogy of quartzitic schist found by XRD-analysis.

| <b>Mineral/<br/>mineral group</b> | <b>%</b> |
|-----------------------------------|----------|
| Quartz                            | 86       |
| Plagioclas                        | 2        |
| Mica                              | 9        |
| Pyrrhotite                        | 3        |
| Chlorite                          | <1       |

**Table 7.7:** Mineralogy of trondhjemite found by XRD-analysis.

| <b>Mineral/<br/>mineral group</b> | <b>%</b> |
|-----------------------------------|----------|
| Quartz                            | 20       |
| Plagioclas                        | 62       |
| Feldspar                          | 6        |
| Mica                              | 8        |
| Chlorite                          | 2        |
| Diopside                          | 2        |

The quartzitic schist had a very high content of quartz, and could be a result of badly chosen rock pieces. For example if the pieces were taken from a part of the rock mass with veins or lenses of quartz. The quartz content in the mica gneiss close to the powerhouse is 18-23 % according to Dahlø et al. (1988). Only an identification of the mineral composition was performed for the red substance. Quantification was too difficult to accomplish from the intensity plot. Identified minerals are given in Table 7.8.

**Table 7.8:** Minerals found from XRD-analysis of red substance.

| <b>Mineral/<br/>mineral group</b> |
|-----------------------------------|
| Quartz                            |
| Mica                              |
| Clinochlore                       |
| Lepidocrocite                     |

Lepidocrocite (FeO(OH)) is a weathering or oxidation product from other iron-bearing minerals, and can be found in soils, mineral deposits and as a precipitate from ground water (Anthony, 1990). It has a reddish-brown rusty look, and is probably the reason for the red substance together with other iron oxides. Quartz is also found, and quartz particles on the joint surfaces can lead to an increase in shear strength of joints.

# Instability assessment methodologies

The most common ways of evaluating tunnel stability are from mathematical or analytical analysis, empirical methods and numerical modelling (Rahmani et al., 2012). Rock mass properties and information about structural geology is required in the use of empirical methods. Also many empirical methods allow the use of empirical rating systems. For numerical modelling rock mechanical parameters for the intact rock is necessary, which are often time consuming and difficult to acquire.

In this chapter the stability assessment methods used in the analyses will be described, together with required input parameters.

## 8.1 Empirical methods

Several empirical methods for predicting rock spalling or rock burst failure have been developed over the years. Some of these methods will be presented in this section.

### 8.1.1 Q-system approach

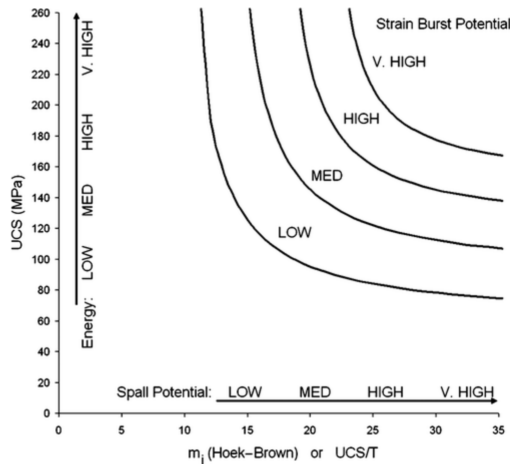
The Q-system developed by Barton et al. (1974b), presented in Section 4.4.1, gives a way of assessing stress induced instabilities through the SRF parameter (Strength Reduction Factor). To find the SRF and the corresponding stress condition presented in Table 8.1, the uniaxial compressive strength  $\sigma_{ci}$ , the major principal stress  $\sigma_1$  and the maximum tangential stress  $\sigma_{\theta max}$  are needed. The ratio between the different parameters can then be calculated and the corresponding stress condition can be found (NGI, 2015).

**Table 8.1:** Description of potential stress induced stability in competent rock mass, from the Q-system handbook (NGI, 2015).

| Competent, mainly massive rock, stress problems  | $\sigma_{ci}/\sigma_1$ | $\sigma_{\theta max}/\sigma_{ci}$ | SRF       |
|--|------------------------|-----------------------------------|-----------|
| Low stress, near surface, open joints  | >200                   | <0.01                             | 2.5       |
| Medium stress, favourable stress condition   | 200 - 10               | 0.01 - 0.3                        | 1         |
| High stress, very tight structure.<br>Usually favourable to stability.<br>May be unfavourable depending on orientation compared to jointing/weakness planes. | 10 - 5                 | 0.3 - 0.4                         | 0.5 - 5   |
| Moderate spalling and/or slabbing after >1 hour  | 5 - 3                  | 0.5 - 0.65                        | 5 - 50    |
| Spalling or rock burst after a few minutes   | 3 - 2                  | 0.65 - 1                          | 50 - 200  |
| Heavy rock burst and immediate dynamic deformation   | 2                      | 1                                 | 200 - 400 |

### 8.1.2 Potential for rock spalling

Diederichs (2007, 2014) proposes an approach for predicting spalling failure potential in intact rock, based on compressive and tensile strength. The UCS together with the brittleness indicator, ratio of USC and tensile strength, provide a simple tool for predicting strain burst potential as can be seen in Figure 8.1.



**Figure 8.1:** Potential for rock spalling/rock burst based on compressive and tensile strength of intact rock. (Diederichs, 2007).

The method assumes that in hard, strong and brittle rock masses under compression, the crack initiation (spalling, extension fractures) occurs as a result of internal heterogeneities and strain anisotropy. Also, that the tensile strength will greatly influence the crack initi-

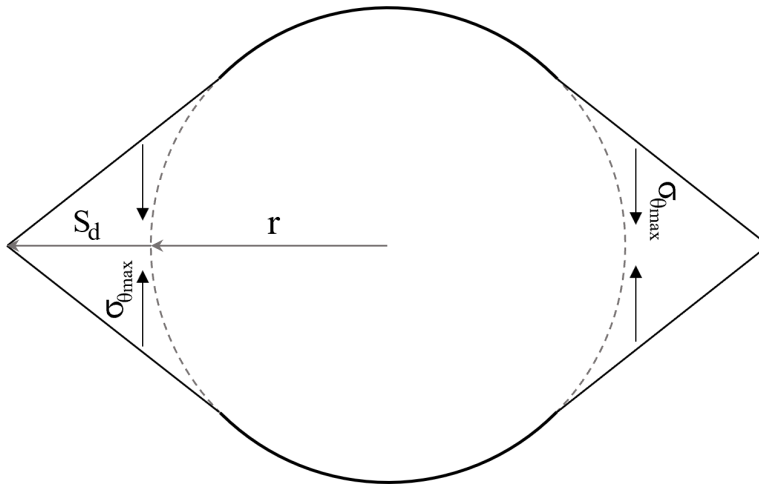
ation (Panthi, 2018). The method does not take into account any structures or stresses in the rock mass.

### 8.1.3 Spalling depth

The two methods above give a qualitative indication whether or not spalling will occur. In addition it is of interest to find out how far into the rock mass the spalling propagates. Martin and Christiansson (2009) offer a way to calculate the spalling depth  $S_d$  of rock spalling around a circular tunnel:

$$S_d = r \times \left( 0.5 \times \frac{\sigma_{\theta_{max}}}{\sigma_{sc}} - 0.52 \right) \quad (8.1)$$

where  $r$  is the radius,  $\sigma_{\theta_{max}}$  is the maximum tangential stress and  $\sigma_{sc}$  the rock mass spalling strength. The spalling depth impact is measured from the boundary of the tunnel as illustrated in Figure 8.2.



**Figure 8.2:** Illustration of depth of spalling due to high tangential stress (re-produced after (Martin and Christiansson, 2009)).

There are several suggestions of what the spalling strength for different rocks could be. Diederichs (2014) suggests that the spalling strength is 0.4 - 0.6 times the laboratory tested strength. Panthi (2018) suggests that the rock mass spalling strength is the same as the rock mass strength and can be found with the equations listed in Table 3.4.

## 8.2 Block and wedge stability

### 8.2.1 Limit equilibrium analysis

Limit equilibrium analysis is a much used method in engineering geology to determine the stability of blocks and wedges around a tunnel periphery. To use the method a simplified

model of the block or wedge is made, usually in two dimensions. For an example see Figure 9.2. The forces acting on the block are then divided into driving forces and stabilising forces. The stability of the block can be represented by a safety factor  $SF$ :

$$SF = \frac{\text{Resisting forces}}{\text{Driving forces}} \quad (8.2)$$

where a safety factor of  $SF \leq 1$  means the block will fail, but it will be stable if  $SF > 1$  (Li, 2017b).

The driving forces are the forces acting in the direction of movement of the block, such as the weight of the block, water pressure in the joints and seismic activity (Nilsen, 2016). The resisting forces counteracts the driving forces, and are mostly a result of the frictional resistance of the joint surfaces and applied support. The frictional resistance of a joint can be described by the shear strength of the joint.

### 8.2.2 Unwedge

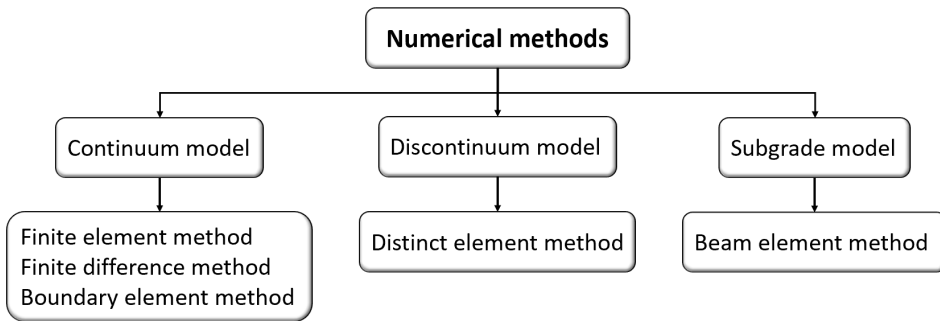
Making a simplification of a block situation is not always possible, as joint sets and the tunnel contour can divide the rock mass into wedges and blocks of countless shapes and sizes. Three-dimensional calculations of such a problem is possible, but it is more efficient to utilise computer programs. One such program is Unwedge (Hoek, 2007b).

Unwedge is a quick and simple 3D tool for analysing geometry and stability of wedges in a rock mass divided by discontinuities, around underground openings. The software uses Goodman and Shi's block theory to determine wedges that can be formed from three intersecting joints and the excavation. In addition, Barton and Bandis' joint strength model and the ability to resize wedges have been incorporated. Equilibrium calculations are used to find a factor of safety for the possible wedges (Rocscience, n.d.b).

## 8.3 Numerical modelling

Today numerical methods are considered as the most flexible and complex methods of design, and according to Trinh and Holmøy (2012) have many advantages over empirical and analytical methods. Numerical methods are better at dealing with complicated situations, for example complex geological conditions, profiles and construction procedures. Further, it is suited for projects with lack of information from similar projects, and it gives more detailed information about rock and rock support performance.

In civil and rock engineering the numerical methods can normally be classified as shown in Figure 8.3. Theory and discussion of strength and weaknesses of the different methods are explained by Sinha (1989) and Jing (2003).



**Figure 8.3:** Classification of numerical methods in civil and rock engineering (re-produced after (Sinha, 1989)).

The two main categories for numerical modelling are continuous models and discontinuous models (Nilsen and Thidemann, 1993). Continuous models consider the rock mass as a continuous medium, where only a limited number of discontinuities are present, such as joints, faults, etc. The Finite Element Method (FEM) and the Boundary Element Method (BEM) are commonly used. Discontinuous models use a system of single blocks to model the rock mass, which are free to move along the edges. The Universal Distinct Element Code (UDEC) is one example.

### RS<sup>2</sup> (Phase2)

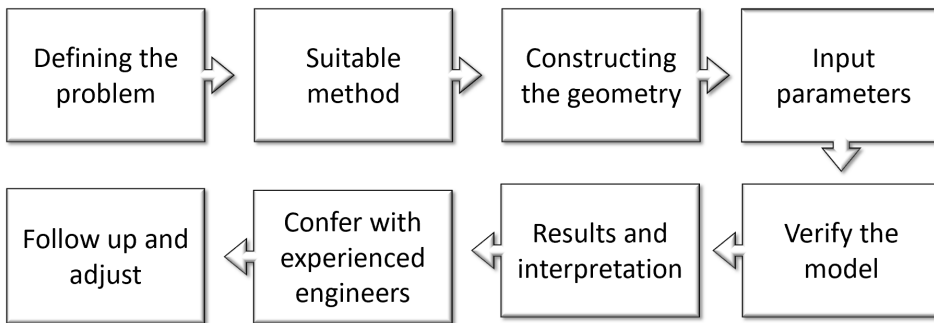
RS<sup>2</sup>, formerly Phase2, is a two-dimensional finite element program, with a wide applicability. It can be used for both soil and rock engineering problems, and can analyse tunnel and support design, underground excavations, groundwater seepage and more (Rockscience, n.d.a).

The rock mass, in an RS<sup>2</sup> analysis, is divided into a number of finite elements and each element is given rock properties, such as density, rock strength and deformation modulus. The elements make up a mesh inside an external boundary and are interconnected in node points. The computer program uses a set of equations to calculate forces and deformations in the nodes (Nilsen, 2016). The rock mass can be considered as an elastic or plastic material. In an elastic analysis the rock strength is divided by the induced stress in each node in the mesh, which gives a strength factor *SF*. A failure of the rock material is represented by a *SF* less than 1. A plastic material will be allowed to yield and a zone of yielded elements can give an indication of the extent of failure (Edelbro, 2010).

### Procedure of numerical analysis

Trinh and Holmøy (2012) recommend a procedure for numerical analysis, in order to get the most out of the results and reduce uncertainties. The procedure follows eight steps, which are illustrated in Figure 8.4 and described in the following.





**Figure 8.4:** Recommended procedure for numerical analysis.

1. **Defining the problem.** The problem for analysis needs to be defined. Such problems can be stability of hard rock tunnels and caverns, tunnelling in poor rock mass, stability in jointed rock mass, etc. This will identify the target for the analysis.
2. **Suitable method.** When the problem is correctly defined an engineer must select a suitable analysis method. All methods explained previously have its own limitations, advantages and disadvantages. A continuous model would be appropriate for tunnelling in extremely poor rock. Also, the problem could require a static or dynamic, or 2D or 3D analysis, or the different methods have to be combined to find a solution.
3. **Constructing the geometry.** A simplified geometry of the problem area has to be incorporated into the program, as the actual geometry is often too complicated. The tunnel periphery of a drill and blast tunnel is uneven and differs, and a simplified model has to be adopted. It is also important to model the excavation procedure as it is planned, or how it was completed, depending on whether the analysis is conducted in the planning phase or at a later stage.
4. **Input parameters.** The quality of the results of the analysis is dependent on the quality of the input parameters. Great effort should be put into finding good quality input parameters, from reference projects, site investigations, field mapping, and both in-situ and laboratory testing.
5. **Verify the model.** The results from the model should be compared with observations made in-situ during excavation for verification, or run with known situations to see if they are reasonable. This step could also be implemented in step four to evaluate the quality of the input parameters. If the model does not correspond to the observations/in-situ measurements, it has to be improved by reviewing the input parameters.
6. **Results and interpretations.** Different results can be extracted from different numerical analysis. The most common are contour plots of stress distribution, yielded zone, displacement, distribution of pore pressure, etc. Interpretation of results require considerable practical experience from engineering projects, as well as from numerical modelling. A presentation of the result should be clear and easy to understand, without "numerical modelling language".

7. Confer with experienced engineers. Discussing the results with experienced rock engineers can be another way of verifying the results. This can be a good way to minimise uncertainties in the analysis.

8. Follow up and adjust. Even after obtaining the results, they might not be the final conclusion. As there are uncertainty in numerical modelling, the results should always be followed up, reviewed and improved if necessary. Monitoring the behaviour of the rock mass could be necessary in complicated and critical situations.

## 8.4 Input parameters for stability analysis

Rock mechanical properties and other input parameters to be used in the stability assessments have been found through laboratory testing, literature and field work. Some will be discussed in this section, together with other parameters needed for the different stability assessment methods.

### 8.4.1 Rock mechanical parameters

For the trondhjemite only the uniaxial compressive strength of 173 MPa and tensile strength of 9.9 MPa were needed. The input parameters for the quartzitic schist can be found in Table 8.2. The uniaxial compressive strength of the quartzitic schist was tested normal to the foliation. The point load test revealed that the rock is highly anisotropic, and the measured 182 MPa would be an overestimation of the rock strength. The anisotropy index was used to calculate the corresponding strength parallel with the foliation. In the analyses a uniaxial compressive strength of 69 (parallel) and 126 (mean) MPa is used.

The Mohr-Coloumb parameters used for the failure criteria in RS<sup>2</sup> can be found through the software RocData, by the Hoek-Brown parameters  $GSI$ ,  $m_i$  and  $D$ . The GSI value was estimated according to Figure 4.8. The quartzitic schist is blocky and the joint surface is slightly weathered with an iron coating, which gives a GSI value of  $70 \pm 5$ . As no good  $m_i$  value for a quartzitic schist can be found in literature, the mean value of a quartzite(20) and schist(12) recommended by RocData was chosen. The disturbance factor was set to 0, since the tunnel being analysed was excavated by TBM.

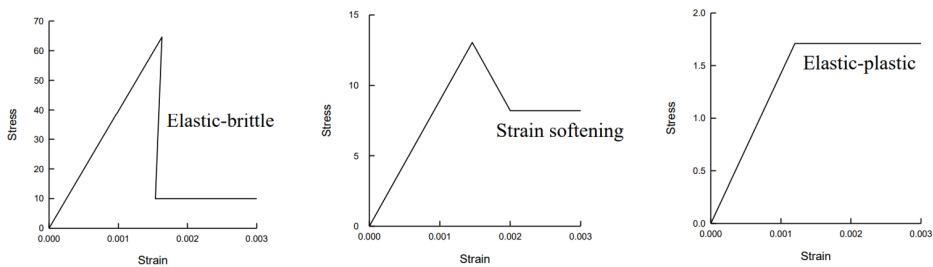
RS<sup>2</sup> also requires a dilation angle. The dilatancy is a measure of the volume increase in a material during shearing (Edelbro, 2010). According to Hoek and Brown (1997) the dilation angle is 1/4 of the peak friction angle  $\phi$  for a good quality rock mass. (Rocscience, n.d.a) suggests a dilation angle of 0.333 of the peak friction angle for soft rock masses and 0.666 times the friction angle for hard rock masses. The dilation angle was chosen to be half the friction angle.

**Table 8.2:** Rock mechanical parameters for quartzite schist

| Parameter     | Description                 | Value | Unit              | Source                                   |
|---------------|-----------------------------|-------|-------------------|--|
| $\sigma_{ci}$ | Intact rock strengt, mean   | 126   | MPa               | Laboratory work<br>Section 7.3           |
|               | and parallel with foliation | 69    | MPa               | Intact rock strength<br>divided by $I_a$ |
| GSI           | Geological strength index   | 70    | -                 |  |
| $m_i$         | Material constant           | 16    | -                 |  |
| $E_{ci}$      | Intact def. modulus         | 51.8  | GPa               | Laboratory work<br>Section 7.3           |
| $\nu$         | Poisson's ratio             | 0.27  | -                 | Laboratory work<br>Section 7.3           |
| $\gamma$      | Spesific weight             | 26.4  | kN/m <sup>3</sup> | Laboratory work<br>Section 7.2           |
| $I_a$         | Strength anisotropy index   | 2.64  | -                 | Laboratory work<br>Section 7.4           |
| $\sigma_t$    | Tensile strength            | 20.7  | MPa               | Laboratory work<br>Section 7.5           |

### 8.4.2 Post-peak behaviour

To be able to simulate failure of the rock mass in numerical modelling, the post-peak or post-failure characteristics are needed. Hoek (2007b) suggests the post-failure characteristics in Figure 8.5, which depend upon the quality of the rock mass. A massive brittle rock mass is best represented by an elastic-brittle-plastic material model, which loses almost all strength at failure (left). An average quality rock mass or a soft rock mass will be able to maintain some or all of its strength after failure (middle, right).



**Figure 8.5:** Post-failure characteristics for different quality rock masses. Very good quality rock mass (left), average quality rock mass (middle) and poor quality rock mass (right) (Hoek, 2007b).

Cai et al. (2007) have suggested another method of finding the residual strength of a rock mass by the use of the GSI system. A residual geological strength index  $GSI_r$  is found by reducing the the block volume and joint conditions. This method is based

upon experiments performed, which indicates that the post-failure strength of a rock mass depends upon the resistance of newly developed failure surfaces and interlocking between the blocks. The tests gave the following empirical relationship for calculating the  $GSI_r$ :

$$GSI_r = GSI \times e^{-0.0134GSI} \quad (8.3)$$

When using this method in a numerical analysis the intact rock properties  $\sigma_{ci}$  and  $m_i$  should not be changed. The residual strength parameters can then be found the same way as for the peak strength parameters by using a failure criteria, such as the generalized Hoek-Brown or the Mohr-Coulomb criterion.

### 8.4.3 Estimation of in-situ stress conditions

The total major and minor horizontal stress in an area can be assumed to be composed of the tectonic stress and by the gravity due to Poisson's effect of the rock mass. As there are only 24 km between Brattset HPP and Ulset HPP, the same tectonic stresses can be assumed for both locations. The tectonic stress at Brattset HPP can be found by the stress measurements presented in Section 6.2.4 and Equations 8.4 and 8.5 (Basnet and Panthi, 2019):

$$\sigma_H = \sigma_{T_{max}} + \frac{\nu}{1 - \nu} \sigma_v \quad (8.4)$$

$$\sigma_h = \sigma_{T_{min}} + \frac{\nu}{1 - \nu} \sigma_v \quad (8.5)$$

where  $\sigma_H$  and  $\sigma_h$  are the major and minor horizontal stresses,  $\nu$  is Poisson's ratio,  $\sigma_T$  is the tectonic stress and  $\sigma_v$  the vertical stress. Rock mass values and calculated stresses can be found in Table 8.3.

**Table 8.3:** Rock mass values, measured stresses at the air cushion chamber at Brattset HPP and calculated tectonic stresses are presented.

| Parameter                                   | Value | Unit | Source                     |
|---|-------|------|----------------------------|
| Depth, $z$                                  | 166   | m    | (Halseth, 2018)            |
| Vertical stress, $\sigma_v$                 | 5.7   | MPa  | (Halseth, 2018)            |
| Major horizontal stress, $\sigma_H$         | 15.6  | MPa  | (Hansen and Hanssen, 1988) |
| Minor horizontal stress, $\sigma_h$         | 6.1   | MPa  | (Hansen and Hanssen, 1988) |
| Poisson's ratio, $\nu$                      | 0.15  |      | (Halseth, 2018)            |
| Maximum tectonic stress, $\sigma_{t_{max}}$ | 14.6  | MPa  | Equation 8.4               |
| Minimum tectonic stress, $\sigma_{t_{min}}$ | 5.1   | MPa  | Equation 8.5               |

Equation 8.4 and 8.5 can then again be used to calculate the horizontal stresses at different depths at Ulset HPP.

Further analysis of the tunnel stability in 2D will be conducted in a cross section normal to the tunnel axis. As the in-situ horizontal stresses found do not strike the tunnel alignment normal and parallel, the equivalent in-plane and out-of-plane stresses have to be resolved. The method is described in (Basnet and Panthi, 2019). Figure 8.6 illustrates this method, and the following equations should be used to find the in-plane and out-of-plane stresses:

$$\sigma_{in-plane} = \sigma_H \cos^2 \alpha + \sigma_h \sin^2 \alpha \tag{8.6}$$

$$\sigma_{out-of-plane} = \sigma_H \sin^2 \alpha + \sigma_h \cos^2 \alpha \tag{8.7}$$

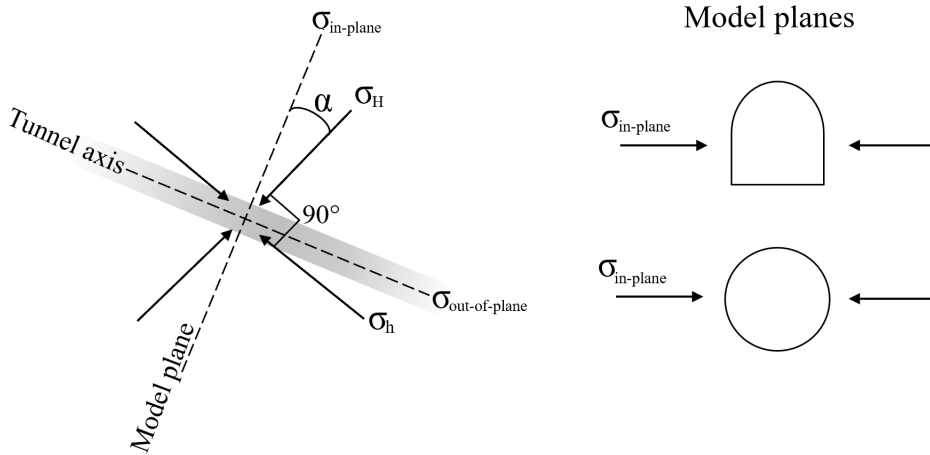


Figure 8.6: Illustration of how the horizontal stresses can be resolved into the model planes.

### 8.4.4 Joint parameters

#### Shear strength of joints

According to (Barton and Choubey, 1977) the JCS of newly developed joints is the same as the intact rock strength. If joints are water conducting JCS becomes less than the intact rock strength. If the joint walls are weathered or altered the JCS becomes a fraction of the intact rock strength. Ideally the JCS should be found in the field with a Schmidt hammer, but this test was not performed during field work. It will therefore be assumed that the decrease in joint wall strength is the same as for a rock mass. In the analysis of the different failures it is of interest to look at a reduction in the joint's shear strength. The shear strength is represented by the Barton-Bandis shear strength criterion and the values

are given in Table 8.4. The range of values represents the joint walls from first excavated and further weathering from the water in the tunnel system.

**Table 8.4:** Parameters used in the Barton-Bandis formula.

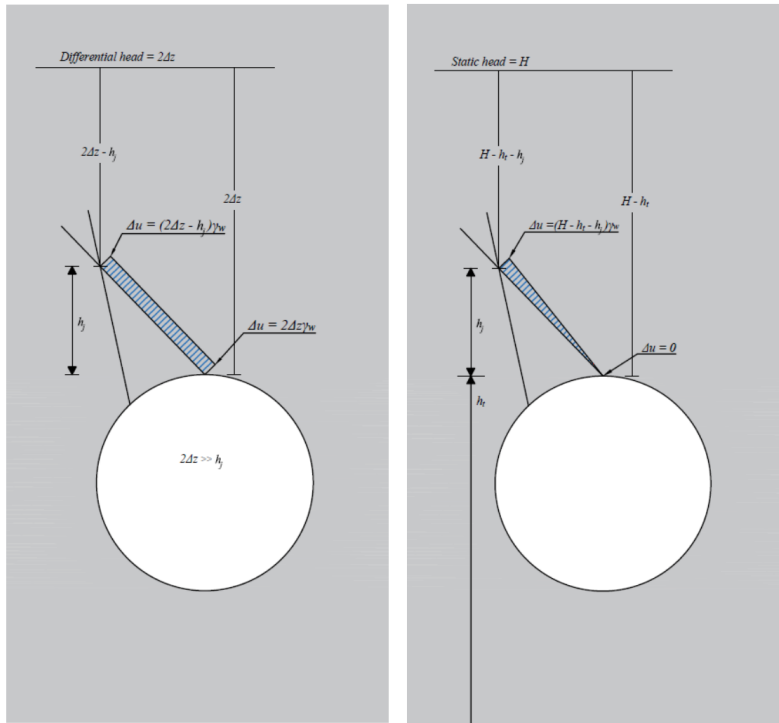
| Parameter | Description                       | Value     | Unit | Source     |
|-----------|-----------------------------------|-----------|------|------------|
| JCS       | $0.5 \times \text{UCS}$           | 90 - 40   | MPa  | Figure 3.5 |
| JRC       | Decrease in small scale roughness | 9 - 6     | -    | Figure 3.2 |
| $\phi_r$  | Same as basic friction angle      | 26.3 - 20 | °    | Table 7.5  |

### Water pressure in joints

To be able to simulate the water pressure on the joints, some simplifications have to be made. As discussed by Halseth (2018), during continuous operation of a hydropower station the water flow in a water tunnel is in a steady state, leading to an equal water pressure in the tunnel and rock mass. This equilibrium will be disturbed by start-and-stop cycles in the operation scheme, which lead to pressure fluctuations along the tunnel system. These pressure fluctuations should result in an increase in pressure on the joints. The second situation, which could lead to an increased pressure on the joints, are during dewatering or draining of the tunnel. Figure 8.7 illustrates both situations.

The situation left in Figure 8.7 illustrates the water pressure on a joint from mass oscillations. The water pressure is due to the upsurge and downsurge wave, which creates a pressure drop inside the tunnel. If there is a delay in the drop of the joint pressure, the worst case pressure the joint will experience is that of the mass oscillation. The water pressure at the end of the joint will be slightly lower than at the tunnel contour due to the height  $h_j$ . If this height is ignored, the pressure from mass oscillations can be regarded as an evenly distributed load in further analysis (Halseth, 2018) ( $\Delta u = 2\Delta z \gamma_y = 2 \cdot 34 \text{ m} \cdot 9.81 \text{ kN/m}^3 = 0.67 \text{ MPa}$ ).

Draining of the tunnel is illustrated right in Figure 8.7. Before draining the hydrostatic head at any location of the tunnel would be  $H$ , and the pressure at the tunnel contour would be  $H - h_t$ .  $h_j$  is the water head when the water level is at the tunnel crown. Draining of the tunnel will lower the water head inside the tunnel ( $H = h_t$ ). If the joint is partly drained the water pressure at the tunnel contour will be  $\Delta u = 0$ , and the water pressure can be regarded as a triangular distribution. The water pressure at the end of the joint will then be  $\Delta u = (H - h_t - h_j)\gamma_y$  (Halseth, 2018). Furthermore, should the tunnel system be drained too fast, the pressure acting on the joints could be a sum of contributions from both the static pressure and that of mass oscillations (Dr. Krishna Panthi, discussion with supervisor, 02.05.18).



**Figure 8.7:** Differential pressure in joints due to mass oscillations (left) and due to draining (right) (Halseth, 2018).

### Joint stiffness

RS<sup>2</sup> requires the normal and shear joint stiffness to describe joint properties. The joint's normal stiffness  $K_n$  can be found by the deformational properties of intact rock and the rock mass, together with joint spacing  $L$ . The joint normal stiffness can then be written as (Barton, 1972):

$$K_n = \frac{E_{ci} \times E_m}{L(E_{ci} - E_m)} \quad (8.8)$$

In the same way, the joint shear stiffness can be found by the use of shear modulus  $G$  of intact rock and the rock mass:

$$K_s = \frac{G_{ci} \times G_m}{L(G_{ci} - G_m)} \quad (8.9)$$

The shear modulus can be found from the following equation:

$$G = \frac{E}{2(1 + \nu)} \quad (8.10)$$

# Stability analysis

## 9.1 Spalling

In spalling rock mass, extension fractures may develop and result in thin slabs parallel to the tunnel periphery before the actual rock burst (Panthi, 2018). There exist several empirical methods for evaluating rock spalling/burst potential in tunnels and mines. Some of these methods were described in Section 8.1, and will now be used to analyse spalling in the headrace tunnel at Ulset HPP.

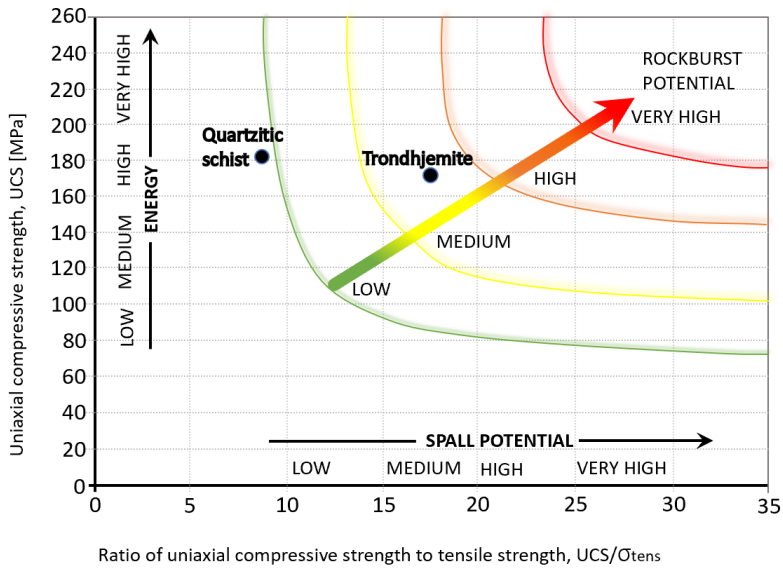
### 9.1.1 Potential for rock spalling

Diederichs (2007) gives a way to assess the spalling or rock burst potential in rocks based on the uniaxial compressive and tensile strength of intact rocks.

#### Results

The quartzitic schist and trondhemite have been plotted in Figure 9.1. The quartzitic schist shows little to no sign of spalling potential, while the trondhemite shows medium potential for spalling and rock burst. The diagram is however independent of stresses and structures in the rock mass. Weaker material might yield in shear before enough energy can be stored to cause a rock burst (Diederichs, 2014).





**Figure 9.1:** Potential for rock spalling/rock burst based on compressive and tensile strength of intact rock. Quartzitic schist and trondhjemite are plotted with red crosses (Re-produced after (Diederichs, 2007, 2014)).

### 9.1.2 Q-system approach and Spalling depth

Spalling is seen in the crown of the TBM-tunnel downstream of the Stor-Sverjesjøen shaft, and is believed to have developed after 1992. The compressive strength of the intact rock  $\sigma_{ci}$ , together with the major principal stress  $\sigma_1$  and the maximum tangential stress at the tunnel contour  $\sigma_{\theta_{max}}$  are needed to calculate the SRF parameter, which gives an indication of stress related problems that might occur. The spalling depth will also be calculated.

#### Stress situation

Table 9.1 shows the stress situation at 3100 m downstream of the CSS. The minor and major stresses are assumed horizontal and used as principal stresses.

**Table 9.1:** Stress situation at 3100 m downstream of the CSS

| Parameter           | Description                      | Value  | Unit              | Source                         |
|---------------------|----------------------------------|--------|-------------------|--------------------------------|
| $z$                 | Tunnel Depth                     | 260    | m                 | Appendix B                     |
| $\gamma_{qs}$       | Unit weight of quartzitic schist | 0.0264 | MN/m <sup>3</sup> | Table 7.2                      |
| $\sigma_v$          | Vertical stress                  | 6.7    | MPa               | Equation 4.1                   |
| $\sigma_H$          | Major horizontal stress          | 17.1   | MPa               | Equation 8.4                   |
| $\sigma_h$          | Minor horizontal stress          | 7.6    | MPa               | Equation 8.5                   |
| $\sigma_{ip}$       | In-plane horizontal stress       | 13.7   | MPa               | Equation 8.6 ( $\alpha = 37$ ) |
| $\sigma_{op}$       | Out-of-plane horizontal stress   | 11.0   | MPa               | Equation 8.7 ( $\alpha = 37$ ) |
| $\sigma_{\theta_r}$ | Tangential stress in roof        | 30.1   | MPa               | Equation 4.5                   |

## Results

The stress related instability according to the Q-system and the depth impact are analysed for two different values of uniaxial compressive strength for the quartzitic schist, mean and parallel. The spalling strength  $\sigma_{sm}$  is suggested by Panthi (2018) to be the same as the rock mass strength  $\sigma_{cm}$ , which can be calculated as described in Table 3.4 for a schistose rock mass.

**Table 9.2:** Results of stress related instability analysis by Q-system.

| Rock                                   | $\sigma_{ci}$ [MPa] | $\sigma_{ci}/\sigma_1$ | $\sigma_{\theta max}/\sigma_{ci}$ | Stress problems  |
|--|---------------------|------------------------|-----------------------------------|--|
| Quartzitic schist (Mean)               | 126                 | 7.3                    | (0.24)                            | (Medium stress, favourable stress condition)<br>High stress, very tight structure.<br>Usually favourable to stability.<br>May be unfavourable depending on orientation compared to jointing/weakness planes. |
| Quartzitic schist (Parallel foliation) | 69                  | 4                      | 0.44                              | Moderate spalling and/or slabbing after > 1 hour   |

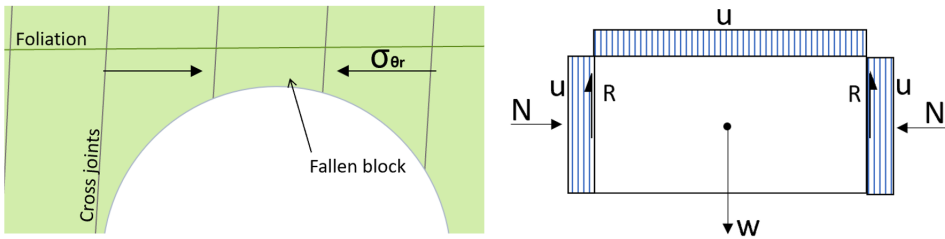
**Table 9.3:** Results from spalling depth impact in quartzitic schist

| Rock                                   | $\sigma_{ci}$ [MPa] | $\sigma_{sm}$ [MPa] | Depth impact $S_d$ [m] |
|--|---------------------|---------------------|------------------------|
| Quartzitic schist (Mean)               | 126                 | 23.6                | 0.3                    |
| Quartzitic schist (Parallel foliation) | 69                  | 9.6                 | 2.4                    |

## 9.2 Limit equilibrium analysis of block fall

The foliation joints together with NE and SE trending cross joints divide the rock mass into blocks, as seen in Figure 6.18. The block failed approximately between 1992 and 2017. Several smaller and larger blocks, with this shape, have fallen from the roof in the same period. An analysis of this block will therefore be conducted, to study how a reduction in the shear strength of joints affect stability.

A simplified situation of the block fall is illustrated in Figure 9.2 (left). The joint sets parallel and perpendicular to the tunnel alignment are assumed to be vertical, and the foliation joints are horizontal. The curvature of the tunnel roof is ignored, which gives a rectangular block. Block measurements are given in Table 9.4 together with the weight.



**Figure 9.2:** Illustration of a simplified situation of the block fall (left) and the forces acting on the block (right).

**Table 9.4:** Measurements of block

| Parameter     | Description     | Value | Unit              |
|---------------|-----------------|-------|-------------------|
| $l$           | Length          | 1     | m                 |
| $h$           | Height          | 0.5   | m                 |
| $w$           | Width           | 0.5   | m                 |
| $A_s$         | Area side       | 0.25  | m                 |
| $V$           | Volume of block | 0.25  | m                 |
| $\gamma_{qs}$ | Unit Weight     | 0.264 | kN/m <sup>3</sup> |
| $W$           | Weight of block | 6.6   | kN                |

The forces exerted on a wedge/block are the weight of the block,  $W$ , the normal force on the sliding plane,  $N$ , and the resistance force,  $R$ . The different forces on the block can be seen in Figure 9.2. These are again divided into driving and stabilising forces.

**Driving forces**

Seismic activity is not considered in the analysis. In addition, since the rock mass stresses are assumed to be perfectly horizontal, the normal force acting on the joints will be perpendicular to the direction of movement and hence not have a component in the vertical direction. The driving forces can be written as:

$$D = W + U, \tag{9.1}$$

where  $U$  is the water pressure acting on the foliation joints downwards. The block is assumed to have failed during operation of the power plant, when the water pressure within the rock mass and tunnel are equal. Therefore an increase in water pressure will only come from mass oscillations. The worst case water pressure from mass oscillations were found in Section 5.2.3 and are:

$$U = 2\Delta z\rho_w g \times A = 0.63\text{MPa} \times 0.5\text{m}^2 = 0.31\text{MPa} \tag{9.2}$$

**Resisting forces**

The resisting forces  $R$  are the shear strength of the joints over the area of sliding:

$$R = \tau \times A, \quad (9.3)$$

where  $\tau$  is the shear strength discussed in Section 8.4.4. Weakening of the joint will be represented by a reduction in JCS, JRC and  $\phi_r$ . According to Goodman (1989) the water pressure in a joint reduces the strengthening effect of the normal stress applied to the joint. The normal stress acting on the joint can therefore be written as:

$$\sigma_n = \sigma_{\theta r} - \sigma_{nu}, \quad (9.4)$$

where  $\sigma_{\theta r}$  is the tangential stress in the tunnel roof and  $\sigma_{nu}$  is the water pressure from both a static head of 80 m and mass oscillations. Note that the static head contribution cancels out in the y-direction as a driving force, but not in the x-direction, where it slightly expands the joints lowering the frictional force. The axial and radial stresses would be low and are assumed to not affect the block stability. The stress situation can be found in Table 9.5. However, due to a failure zone that develops around excavations the tangential stresses will be shifted to intact rock mass further from the opening (Li, 2017a). As a result the area of the block would be distressed, and a reduced tangential stress  $\sigma_{\theta re}$  is adopted.

**Table 9.5:** Stress situation at 229 m downstream of the CSS

| Parameter            | Description                      | Value  | Unit              | Source                          |
|----------------------|----------------------------------|--------|-------------------|---------------------------------|
| $z$                  | Tunnel depth                     | 100    | m                 | Appendix B                      |
| $\gamma_{qs}$        | Unit weight of quartzitic schist | 0.0264 | MN/m <sup>3</sup> | Table 7.2                       |
| $\sigma_v$           | Vertical stress                  | 2.64   | MPa               | Equation 4.1                    |
| $\sigma_H$           | Major horizontal stress          | 15.58  | MPa               | Equation 8.4                    |
| $\sigma_h$           | Minor horizontal stress          | 6.08   | MPa               | Equation 8.5                    |
| $\sigma_{ip}$        | In-plane horizontal stress       | 14.76  | MPa               | Equation 8.6                    |
| $\sigma_{\theta r}$  | Tangential stress in roof        | 15.95  | MPa               | Equation 4.7                    |
| $\sigma_{\theta re}$ | Reduced tangential stress        | 2.39   | MPa               | $0.15 \times \sigma_{\theta r}$ |

### 9.2.1 Results

A safety factor is calculated with a range of values for JCS, JRC and residual friction angle. The results are presented in Figure 9.3, where the colours represent a stable (green), close to failed (yellow) and failed (red) block. A reduction in both the JRC and the  $\phi_r$  is needed for the safety factor to fall below 1. The safety factor is not greatly affected by a reduction in JCS.

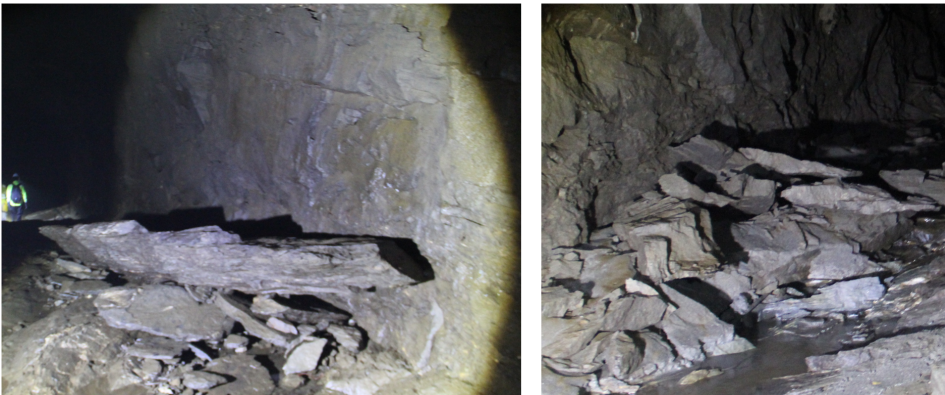
| JRC | $\phi_r$ | JCS [MPa] |      |      |      |      |      |
|-----|----------|-----------|------|------|------|------|------|
|     |          | 90        | 80   | 70   | 60   | 50   | 40   |
| 9   | 26.3°    | 1.47      | 1.44 | 1.42 | 1.39 | 1.36 | 1.32 |
| 9   | 23°      | 1.31      | 1.29 | 1.27 | 1.24 | 1.21 | 1.17 |
| 9   | 20°      | 1.18      | 1.16 | 1.14 | 1.11 | 1.08 | 1.05 |
| 8   | 26.3°    | 1.37      | 1.35 | 1.33 | 1.31 | 1.28 | 1.24 |
| 8   | 23°      | 1.22      | 1.20 | 1.18 | 1.16 | 1.13 | 1.10 |
| 8   | 20°      | 1.09      | 1.08 | 1.06 | 1.04 | 1.02 | 0.97 |
| 6   | 23°      | 1.06      | 1.05 | 1.03 | 1.02 | 1.00 | 0.98 |
| 6   | 20°      | 0.94      | 0.93 | 0.92 | 0.9  | 0.89 | 0.87 |

**Figure 9.3:** Results from the limit equilibrium analysis of block fall, with a range of JCS, JRC and  $\phi_r$ . The block is stable for the green values, close to failure for yellow and red have failed.

## 9.3 Unwedge analysis

### 9.3.1 Model geometry and input parameters

Several wedge failures can be found all along the headrace tunnel, where smaller and larger wedges have fallen or slid along almost vertical joints in the walls, as can be seen in Figure 9.4. The size of the wedge to the left is  $5 \times 1.5$  m (Neupane, 2017) and approximately 0.3 m thick, which gives it a total volume of  $1.13 \text{ m}^3$  as a perfect rectangle. The smaller wedges are roughly  $0.1 \text{ m}^3$ .



**Figure 9.4:** Wedge failure in right wall at approximately 350 m from the CSS (left) and wedge failure in left wall 900 m from CSS (right).

The tunnel is 4.5 m wide, with a 2.25 m wall height and 2.25 m arc (Forodden, 1992). The joint sets found during field mapping at location 1 will be used, as the larger wedge failed

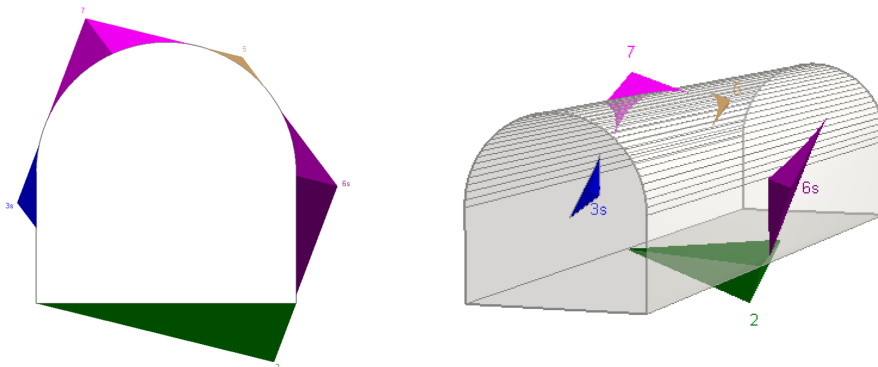
not too far from this area. The Barton-Bandis strength equation will be applied to calculate joint strength, and the parameters JRC, JCS and  $\phi_r$  will be given values as described in Section 8.4.4. Input parameters can be found in Table 9.6.

**Table 9.6:** Input parameters used in the Unwedge analysis.

| Parameters                             |             | Value            | Unit              | Source                          |
|--|-------------|------------------|-------------------|---------------------------------|
| Wedge shape                            | Length      | 5                | m                 | 2017                            |
|  | Width       | 1.5              | m                 | (Neupane, 2017)                 |
|  | Thickness   | 0.3              | m                 | notes                           |
| Tunnel geometry                        | Height      | 2.25             | m                 | 1992                            |
|  | Width       | 4.5              | m                 | report                          |
|  | Arc height  | 2.25             | m                 | (Forodden, 1992)                |
| Tunnel trend/<br>plunge                |             | N293E/<br>12.5NW | °                 | Appendix B                      |
| Density of<br>Quartzitic schist        |             | 0.0264           | MN/m <sup>3</sup> | Laboratory work,<br>section 7.2 |
| Joint system<br>(Dip/dip<br>direction) | Foliation   | 16/008           | °                 | Field                           |
|  | Joint set 1 | 70/195           | °                 | mapping,                        |
|  | Joint set 2 | 82/137           | °                 | Section 6.2.2                   |

### 9.3.2 Unwedge results

Unwedge forms five possible wedges, where the two in the walls fit the description of the wedges being analysed. These are wedge 3 and 6 in Figure 9.5, and are scaled to the size of the observed wedges. The safety factors without water pressure and reduced joint parameters are 16.3 (blue) and 1.23 (purple).



**Figure 9.5:** Five possible wedges from the Unwedge analysis, seen from the front of the tunnel (left) and in 3D from the side (right). The blue and purple wedges (3 and 6) will be used in the further analysis.

The safety factors were calculated for different values of JRC, JCS and  $\phi_r$ , and can be found in Figure 9.6. Different water pressures are added to the model, to simulate pressure increase due to mass oscillations (upsurge 0.31 and downsurge 0.63 MPa) or pressure increase in the joints due to draining of the tunnel with different heads.

| Wedge | JCS | JRC | $\phi_r$ | Water pressure [MPa] |      |       |      |      |      |
|-------|-----|-----|----------|----------------------|------|-------|------|------|------|
|       |     |     |          | 0                    | 0.2  | 0.31  | 0.5  | 0.64 | 1    |
| 6     | 90  | 9   | 26.3°    | 1.23                 | 1.16 | 0.913 | 0.61 | 0.49 | 0.38 |
|       | 60  | 8   | 26.3°    | 1.07                 | 1.02 | 0.80  | 0.54 | 0.43 | 0.34 |
|       | 60  | 6   | 26.3°    | 0.91                 | 0.88 | 0.70  | 0.50 | 0.40 | 0.30 |
| 3     | 90  | 9   | 26.3°    | 16.3                 | 0.71 | 0.66  | 0.46 | 0.40 | 0.38 |

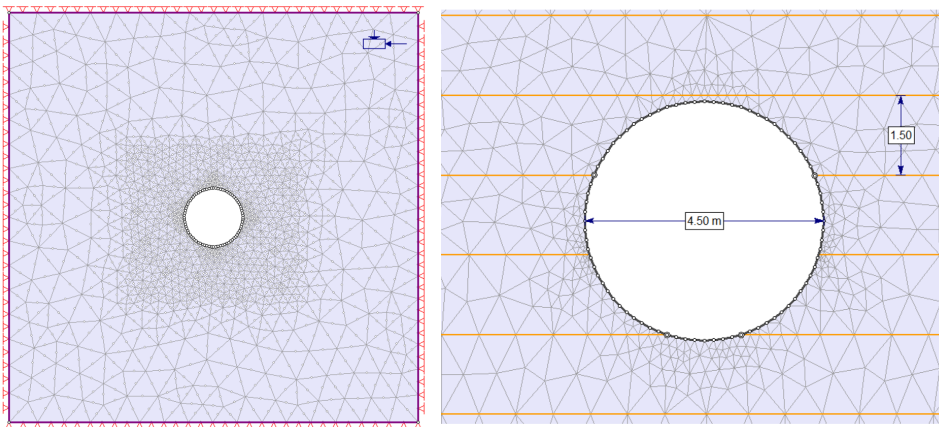
**Figure 9.6:** Result from Unwedge analysis with a range of JCS, JRC and  $\phi_r$ . The block is stable for the green values, close to failure for yellow and red have failed.

## 9.4 Stress induced rock fall

During the excavation and in the first year of operation of the TBM-tunnel, upstream of the Sverjesjøen shaft, many stress induced rock falls occurred. The high stresses left notches in the crown or chipped off sheets of rock due to the foliation. It is therefore of interest to analyse how the foliation joints might have affected the failures.

### 9.4.1 Model geometry

The model geometries are shown in Figure 9.7. The external boundaries are placed at a distance from the excavation to avoid end effects, and are restrained in both X and Y directions. The model is run with and without foliation joints to look at the effect these will have on the stability.



**Figure 9.7:** Model geometry for stress induced instability in the TBM-tunnel. Full model (left) and detail of model with foliation joints (right).

## 9.4.2 Input parameters

### Stress situation

An overview of the calculated stresses is given in Table 9.7. The type of failure is found all the way from the sand trap to the Sverjesjøen shaft, but will be analysed at approximately 2500 m downstream of the CSS.

**Table 9.7:** Stress situation at 2500 m downstream of the CSS

| Parameter     | Description                      | Value  | Unit              | Source                         |
|---------------|----------------------------------|--------|-------------------|--------------------------------|
| $z$           | Tunnel depth                     | 290    | m                 | Appendix B                     |
| $\gamma_{qs}$ | Unit weight of quartzitic schist | 0.0264 | MN/m <sup>3</sup> | Table 7.2                      |
| $\sigma_v$    | Vertical stress                  | 7.5    | MPa               | Equation 4.1                   |
| $\sigma_H$    | Major horizontal stress          | 17.4   | MPa               | Equation 8.4                   |
| $\sigma_h$    | Minor horizontal stress          | 7.9    | MPa               | Equation 8.5                   |
| $\sigma_{ip}$ | In-plane horizontal stress       | 16.6   | MPa               | Equation 8.6 ( $\alpha = 17$ ) |
| $\sigma_{op}$ | Out-of-plane horizontal stress   | 8.7    | MPa               | Equation 8.7 ( $\alpha = 17$ ) |

### Rock mass and joint properties

The effect of the foliation on the quartzitic schist is simulated by reducing the intact rock strength to the mean and parallel to the foliation planes. The model will be run with both values to see which best represents the failures, with both elastic and plastic material. The Barton-Bandis model is applied to the joints, and the Mohr-Coloumb criterion is used for the rock mass after suggestion from Figure 3.8. RocData is used to calculate the Mohr-Coloumb parameters cohesion  $c$ , friction angle  $\phi$  and rock mass modulus  $E_m$ . All values used for the rock mass and joints can be found in Table 9.8 and 9.9. Residual values are calculated according to the  $GSI_r$  method suggested by Cai et al. (2007).

**Table 9.8:** Input parameters for quartzitic schist. Low (parallel to foliation) values are given in brackets.

| Parameter     | Description               | Value       | Residual value | Unit              |
|---------------|---------------------------|-------------|----------------|-------------------|
| $\sigma_{ci}$ | Intact rock strength      | 126 (69)    | -              | MPa               |
| GSI           | Geological strength index | 70          | 27             | -                 |
| $m_i$         | Material constant         | 16          | -              | -                 |
| $E_{ci}$      | Intact def. modulus       | 51.8        | -              | GPa               |
| $\nu$         | Poisson's ratio           | 0.27        | -              | -                 |
| $\sigma_t$    | Tensile strength          | 14.3 (7.8)  | 0              | kN/m <sup>3</sup> |
| $\phi$        | Friction angle            | 55.8 (50.4) | 44.6 (40.0)    | °                 |
| $c$           | Cohesion of block         | 3.5 (2.4)   | 1.2 (0.9)      | MPa               |
| $E_m$         | Rock mass modulus         | 37.9        | -              | GPa               |
| D             | Dilation angle            | -           | 22 (20)        | -                 |

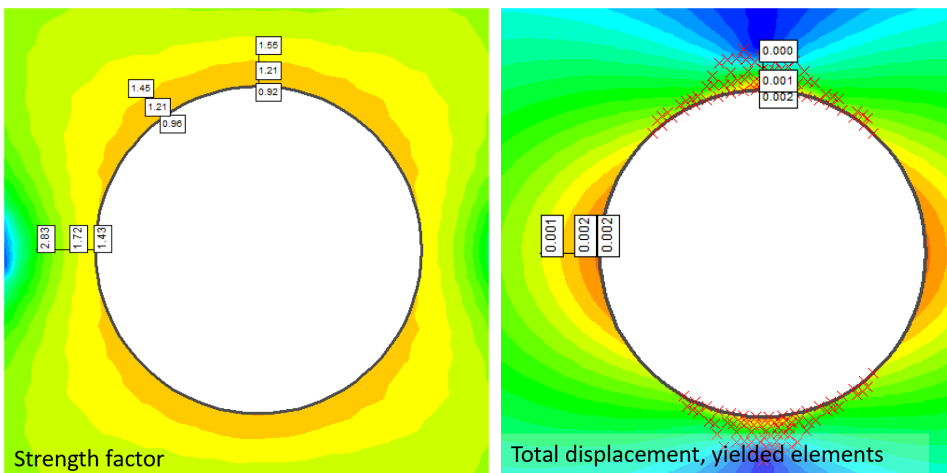


**Table 9.9:** Input parameters for foliation joints.

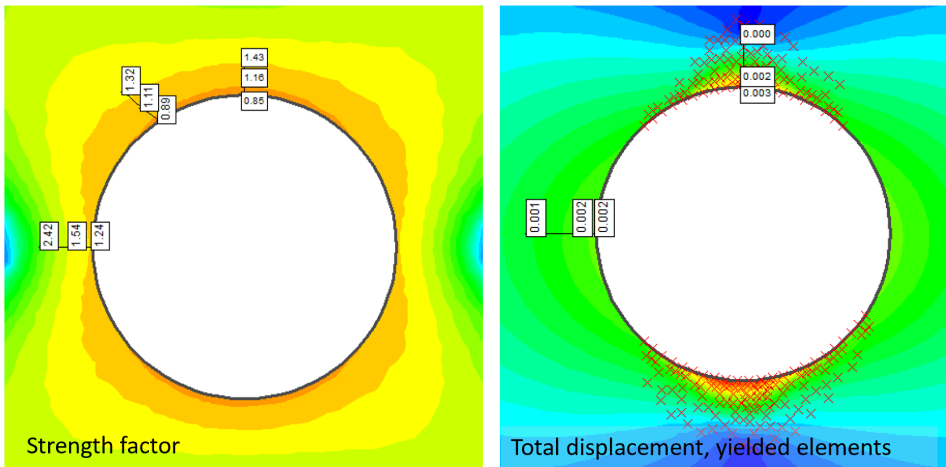
| Parameter | Description             | Value | Unit              | Source        |
|-----------|-------------------------|-------|-------------------|---------------|
| $G_i$     | Intact shear modulus    | 20.4  | GPa               | Equation 8.10 |
| $G_m$     | Rock mass shear modulus | 14.9  | GPa               | Equation 8.10 |
| L         | Mean joint spacing      | 1.5   | m                 | -             |
| $K_n$     | Joint normal stiffness  | 95.1  | GPa               | Equation 8.8  |
| $K_s$     | Joint shear stiffness   | 47.9  | GPa               | Equation 8.9  |
| JCS       | Joint wall strength     | 90    | kN/m <sup>3</sup> | Section 8.4.4 |
| JRC       | Joint roughness         | 9     | -                 | Section 8.4.4 |
| $\phi$    | Residual friction angle | 26.3  | °                 | Section 8.4.4 |

### 9.4.3 Results

The model was run with elastic material to find the strength factor and plastic material to find the total displacement and yielded elements. The results from the analysis with mean intact strength are given in Figure 9.8. The strength factor in the crown and left crown are 0.92 and 0.96, respectively. Figure 9.9 shows the results with the low (parallel with foliation) intact rock strength, where the strength factor is reduced to 0.85 and 0.89 in the crown. Further, both models have yielded elements in the crown and invert. This indicates that localised intact rock failure may occur near the tunnel boundary.

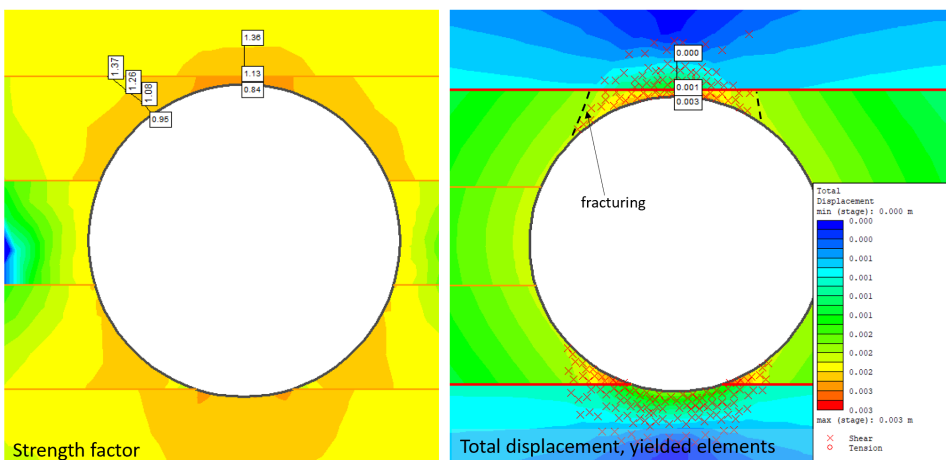


**Figure 9.8:** Strength factor (left), total displacement and 90 yielded elements (right). The yielded elements reach 0.6 m into the rock mass from the crown.



**Figure 9.9:** Strength factor (left), total displacement and 138 yielded elements (right).

Clear failure planes in the crown can be seen at the locations of stress induced failure. Foliation joints were added to the model to simulate these weak planes, and the low rock mass properties were chosen to simulate the worst case scenario. The results are shown in Figure 9.10. The strength factor is reduced to 0.84 in the crown, and this area (dark orange) extends to the joint. The total displacement stays the same, but the number of yielded elements increases from 138 to 204. The joints which have been highlighted with red in Figure 9.10 (right) have yielded. The black striped lines indicate the location of possible joints or stress induced fracturing, which have resulted in the fall of the material under the foliation joint.



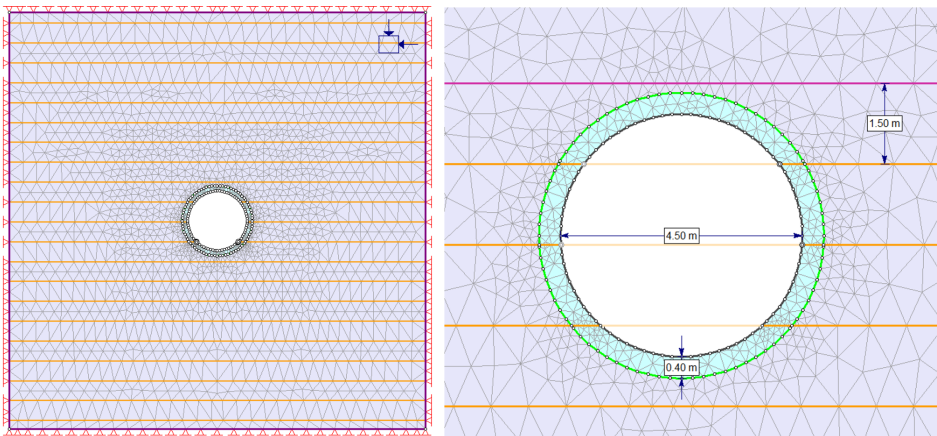
**Figure 9.10:** Strength factor (left), total displacement and 204 yielded elements (right).

## 9.5 Time dependent stress induced rock fall

According to Bardal and Bruland (1986) there were only three new notches (stress induced failures) in the TBM-tunnel after the Sverjesjøen shaft. The failures are located approximately 150 m downstream of the shaft. In 1992 one new minor rock fall was registered at the end of the bored tunnel. The tunnel inspection in 2017 revealed that even more new failures in this part of the tunnel had occurred since the last inspection. This leads to the belief that a reduction in rock mass strength has happened over the past decades for the failures to develop. An attempt at simulating this failure development will be conducted in this analysis.

### 9.5.1 Model geometry

The model geometries can be seen in Figure 9.11. The external boundaries are placed at a distance from the excavation and restrained in both X and Y directions. To simulate the reduction in rock mass strength around the tunnel a material boundary is installed, similar to the damage zone around a blasted tunnel. The last model will be run with a joint system for the foliation.



**Figure 9.11:** Model geometry for analysis of failure development due to rock mass and joint strength reduction.

### 9.5.2 Input parameters

#### Stress situation

The absence of failures (notches) after the Sverjesjøen shaft, led to the belief that the stresses, which induce the instabilities, decrease towards the valley side. However, a high tectonic stress axis dipping towards N060W has been suggested in the powerhouse area, based on observations of spalling in the powerhouse cavern (Dahlø et al., 1988). With the lack of stress measurements, the same stresses as in the other analysis will be used, but the alternative orientation will be adopted. The calculated stresses can be found in Table 9.10.

**Table 9.10:** Stress situation 6000 m downstream of the CSS.

| Parameter     | Description                      | Value  | Unit              | Source                         |
|---------------|----------------------------------|--------|-------------------|--------------------------------|
| $z$           | Tunnel depth                     | 350    | m                 | Appendix B                     |
| $\gamma_{qs}$ | Unit weight of quartzitic schist | 0.0264 | MN/m <sup>3</sup> | Table 7.2                      |
| $\sigma_v$    | Vertical stress                  | 9.1    | MPa               | Equation 4.1                   |
| $\sigma_H$    | Major horizontal stress          | 18.0   | MPa               | Equation 8.4                   |
| $\sigma_h$    | Minor horizontal stress          | 8.5    | MPa               | Equation 8.5                   |
| $\sigma_{ip}$ | In-plane horizontal stress       | 10.5   | MPa               | Equation 8.6 ( $\alpha = 63$ ) |
| $\sigma_{op}$ | Out-of-plane horizontal stress   | 16.0   | MPa               | Equation 8.7 ( $\alpha = 63$ ) |

### Input parameters

The rock mass in this area is less schistose, therefore the mean value for intact rock strength will be used. This value will then be reduced to simulate the reduction in rock mass strength over time, due to the effect of water and pressure fluctuations. The zone reaches 0.4 m into the rock mass. The input parameters used for the rock mass are listed in Table 9.11. The reduced values for the zone are in brackets.

**Table 9.11:** Input parameters for quartzitic schist, reduced values are shown in brackets.

| Parameter     | Description               | Value       | Residual value | Unit              |
|---------------|---------------------------|-------------|----------------|-------------------|
| $\sigma_{ci}$ | Intact rock strength      | 126 (60)    | -              | MPa               |
| GSI           | Geological strength index | 70          | 27             | -                 |
| $m_i$         | Material constant         | 16          | -              | -                 |
| $E_{ci}$      | Intact def. modulus       | 51.8        | -              | GPa               |
| $\nu$         | Poisson's ratio           | 0.27        | -              | -                 |
| $\sigma_t$    | Tensile strength          | 14.3 (7.8)  | 0              | kN/m <sup>3</sup> |
| $\phi$        | Friction angle            | 55.8 (50.0) | 44.6 (37.5)    | °                 |
| $c$           | Cohesion of block         | 3.5 (2.4)   | 1.2 (1.0)      | MPa               |
| $E_m$         | Rock mass modulus         | 37.9        | -              | GPa               |
| D             | Dilation angle            | -           | 22 (18)        |                   |

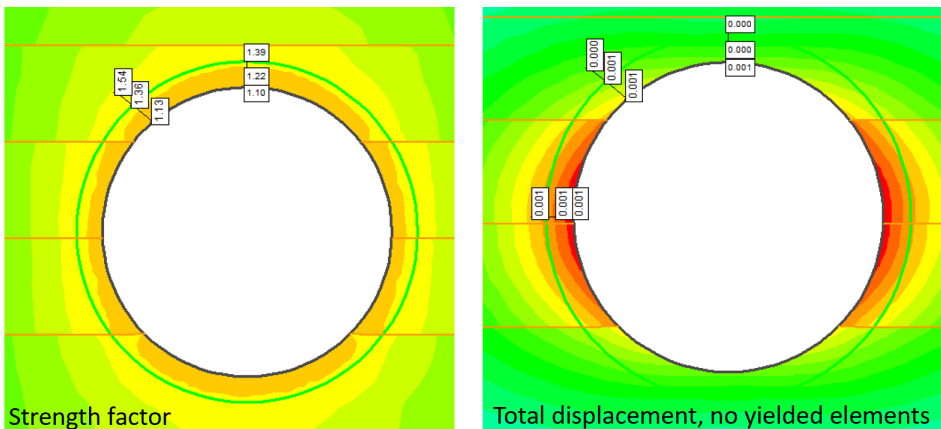
The model will have a joint system to simulate the foliation joints. The joint parameters will also be reduced and a water pressure will be added. The foliation joint above the excavation does not intersect the excavation boundary, but it is assumed that water can reach this joint through cross-joints. For simplicity, the cross-joints are not added to the model. Joint parameters can be found in Table 9.12.

**Table 9.12:** Input parameters for foliation joints, values for weak joints are shown in brackets.

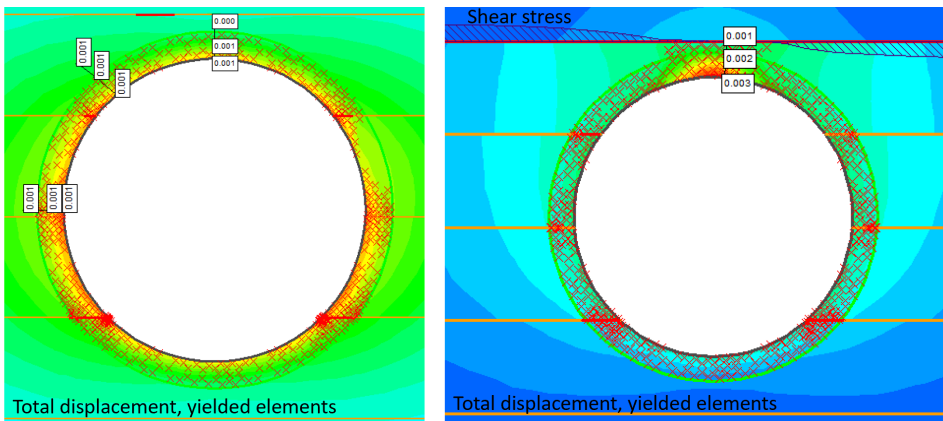
| Parameter | Description             | Value       | Unit              | Source        |
|-----------|-------------------------|-------------|-------------------|---------------|
| $G_i$     | Intact shear modulus    | 20.4        | GPa               | Equation 8.10 |
| $G_m$     | Rock mass shear modulus | 14.9 (7.9)  | GPa               | Equation 8.10 |
| L         | Mean joint spacing      | 1.5         | m                 | -             |
| $K_n$     | Joint normal stiffness  | 95.1 (21.7) | GPa               | Equation 8.8  |
| $K_s$     | Joint shear stiffness   | 47.9 (8.4)  | GPa               | Equation 8.9  |
| JCS       | Joint wall strength     | 90 (60)     | KN/m <sup>3</sup> | Section 8.4.4 |
| JRC       | Joint roughness         | 9 (6)       | -                 | Section 8.4.4 |
| $\phi$    | Residual friction angle | 26.3 (20)   | °                 | Section 8.4.4 |
| u         | Water pressure          | 0.63        | MPa               | -             |

### 9.5.3 Results

Figure 9.12 shows the situation shortly after excavation. The safety factor is 1.10 and 1.13 at the tunnel boundary and there are no yielded elements, which indicates that the tunnel is stable and no failure of the rock material should occur. The total displacement is minimal.

**Figure 9.12:** Strength factor (left), total displacement and no yielded elements (right).

Simulating the impact of water and possible mass oscillations, the rock mass strength close to the tunnel periphery has been reduced in Figure 9.13 (left), resulting in yielded elements and some yielded joints shown with bold red colour. The yielded elements are contained within the zone. By reducing the joint parameters and adding a water pressure, the yielded elements now extend out of the weak zone and intersect the joint above the excavation, Figure 9.13 (right).



**Figure 9.13:** Total displacement and yielded elements for reduced rock mass strength around boundary (left) and added water pressure and joint strength reduction (right).

The total displacement is increased slightly from 0.001 to 0.003 m. The shift in shear stress above the tunnel indicates a slip, which indicates the inward displacement of rock underneath the joint. This joint has yielded along the hole length.



# Chapter 10

## Discussions

### 10.1 Norwegian hydropower and hydraulic transients

Norwegian hydropower is an underground industry with 100 years of experience, and today more than 4000 km of hydropower tunnels have been excavated. The development of hydropower design and construction has led to two Norwegian specialities, unlined tunnels and high pressure shaft and air cushion chambers. This was possible due to a support philosophy that allowed some fallen rocks during the operation time of the hydro power station. Support was only applied in areas with very poor rock mass conditions, and as a result construction cost and time were reduced. The experience has also resulted in today's design criteria, namely the *criteria of confinement*, which says that nowhere along a water tunnel should the hydrostatic water pressure exceed the minor principal stress.

Most of the unlined tunnels in Norway were built when the operation scheme of hydropower plants were continuous (constant water pressure), with a limited number of start-and-stop cycles. However, due to a de-regulation in the power market in 1991 the operation scheme changed from supply to demand driven. This change resulted in an increase in start-and-stop cycles, as power is produced based on energy prices and demand. Start-and-stop of the operation leads to unsteady flow in the waterway system in the form of hydraulic transients. Tunnels with this operation scheme are said to be subjected to *hydropreaking*. Hydraulic transients, water hammers and mass oscillations, all develop when there is a change in load in the system. This causes pressure fluctuations in the water way system, which is not accounted for in the confinement criteria.

Water hammers are pressure waves that develop between the turbine and the the first free water surface. Surge shaft and air cushions were implemented in the water system of hydropower stations close to the turbine, to minimise the pressure increase from the water hammer. As a result water hammers only last for a short period of time (seconds), but this introduces the problem of mass oscillations. Mass oscillations arise between the surge or



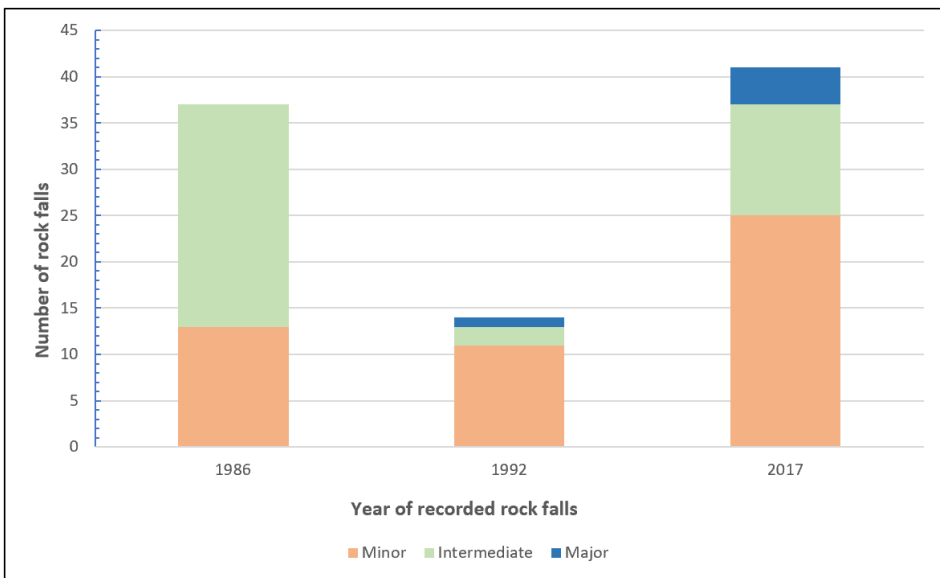
air cushion chamber and the reservoir, and the magnitude of the pressure wave depends on the distance between the two. Mass oscillations are dampened out by frictional losses on the walls in the water system, but last for a longer period than water hammers. The effect mass oscillations have on the rock mass has not been studied, but could, due to the long lifetime, affect the stability of the rock mass.

## 10.2 Stability assessments

The instabilities found during the Project work have in this thesis been systematised into four categories. The presence of high stresses and discontinuities in the rock mass are the major factors affecting the stability. In addition the new operation scheme of hydropower plants seems to further aggravate these instabilities. The stability analysis can be looked at as back analyses, since the failures analysed have already taken place.

### 10.2.1 Timeline

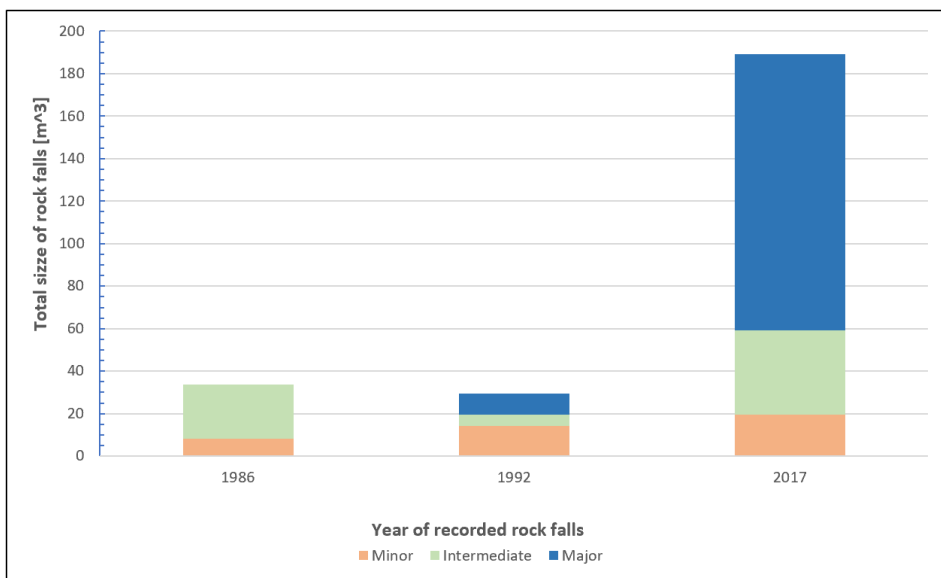
The timeline presented in Figure 6.14 shows only failures visible in the inspection pictures. It was limited to these as the mechanisms behind the failures were of most interest. However, it is also of interest to look at all rock falls to see if they increase or decrease, in both number and size, after the de-regulation of the power market in 1991. The number of rock falls from the inspection reports from 1986, 1992 and 2017 are plotted in Figure 10.1. The rock falls are divided into minor ( $< 0.25 \text{ m}^3$ ), intermediate ( $0.25 \leq I < 10 \text{ m}^3$ ) and major ( $> 10 \text{ m}^3$ ) falls, and the total size of each group can be seen in Figure 10.2. If several rocks have fallen in the same location they are counted as one.



**Figure 10.1:** Number of rock falls recorded in 1986, 1992 and 2017. The rock falls are divided into minor, intermediate and major rock falls.

In 1986 there was reported a total of 37 rock falls. These are most likely a result of the adjustment of the rock mass around the newly excavated tunnels. Redistribution of stresses around an excavation takes some time. In addition, the first watering of the tunnel system would have saturated the rock mass and reduced the strength of the rock material and joints. Both factors could have lead to the failure of "almost failed instabilities". The number of rock falls decreases to 14 in 1992, as the tunnel stability stabilises. The number of minor rock falls stays the same, but the intermediate falls decreases. One major rock fall is reported.

The number of rock falls then rise to 41 in 2017, which is an increase in both minor, intermediate and major rock falls. It has to be noted that the time period between the last two dewaterings is 25 years, in comparison to the six years between 1986 and 1992. This trend corresponds to the findings of Bråtveit et al. (2016), who found that the frequency of rock falls in tunnels subjected to hydropeaking had increased. The approximate size of the rock falls can be seen in Figure 10.2.



**Figure 10.2:** Total size of rock falls recorded in 1986, 1992 and 2017. The rock falls are divided into minor, intermediate and major rock falls.

In 1986 and 1992 the total size of the rock falls are relatively small compared to the fallen rocks in 2017. This is the result of four small to medium scale collapses in the D&B part of the tunnel. These collapses have mostly occurred in parts of the tunnel with poor rock conditions (highly schistose), which were supported during the excavation. The rock conditions have worsened since the commissioning in 1985 and finally lead to failure of the support. There has also then been a buildup of sediment and debris over the fallen rocks, which have lead to narrowing of the tunnel. In some places there are only 2 m left from the buildup to the roof of the tunnel. Further, only a small portion of the sandtrap is

still empty, and the opening of the tunnel is restricted to approximately 6 m<sup>3</sup> reaching over 50 m behind the sandtrap.

### **10.2.2 Spalling potential**

The potential for spalling in the tunnel was analysed through empirical and semi-analytical methods.

According to the method given by Diederichs (2007), evaluation of spalling based on the uniaxial compressive and tensile strength of the intact rock, the quartzitic schist had little to no spalling potential. This does not coincide with the observations from the tunnel and could be a result of that the method does not consider discontinuities and stresses in the rock mass. The trondhjemite had a medium spall potential. This corresponds with Bardal and Bruland (1986), who report that many of the notches in the TBM part of the tunnel occurred in short sections of trondhjemite. The exact location of the trondhjemite is difficult to determine from the inspection pictures, and further analysis was kept to the quartzitic schist.

The Q-system approach is a qualitative method which is based on empirical studies. Since the quartzitic schist is highly foliated and the stresses are parallel with the foliation plane, the mean strength of the intact rock and the lowest strength parallel with the foliation plane were used. With the mean rock strength the method suggested that spalling should not occur unless there is unfavourable orientation of jointing or weakness planes. Moderate spalling might occur in the rock with the reduced strength. The reduction in strength could also represent the weakening from water over time, which then would explain the development of minor spalling over time in the crown of the TBM-tunnel after the Sverjesjøen shaft. The reduction in strength also leads to a large increase in the spalling depth, from 0.3 m with the mean value to 2.4 m with the low. The method used to calculate the spalling depth is a semi-analytical method, based on the spalling strength of the material and maximum tangential stress from case studies.

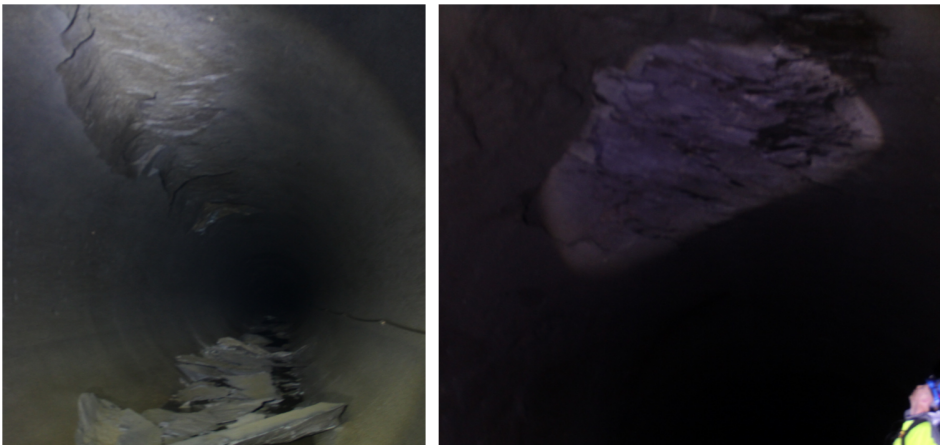
### **10.2.3 Stress induced rock fall**

According to Diederichs (2007) spalling is the development of visible extension fractures under compressive loading, and spalling in hard rock excavation doesn't need to be violent. Spalling can form notch geometries which are often confused with wedge fallout in unsupported conditions and/or under anisotropic conditions. This kind of failure occurred along the headrace tunnel both during and after excavation. The foliation together with the high horizontal stresses are believed to be the major causes of most of the failures in the headrace tunnel. The notches are mostly found in connection with the NE trending joint set.

The effect of the foliation was analysed by a 2D plain strain analysis in RS<sup>2</sup>. In the first model the foliation was included in the intact rock strength by dividing the measured intact rock strength normal to the foliation by the anisotropy index. The second model had the mean intact rock strength with a joint system, to simulate the foliation joints in the quartzitic schist. The first model gave approximately the same results as for the spalling analysis. At the tunnel boundary the strength factor was below 1 and the yielded elements reached 0.6 m into the rock mass, which could indicate localised intact rock failure. When

the foliation joints were inserted, the zone, with a strength factor below 1, intersected the joint. In addition, the joint above the excavation yielded, see Figure 9.10. A cross-joint or induced fracturing would then have caused the fall of the material under the joint.

The results from the analysis show similarities to the stress induced failures that occurred during the excavation. The reduction in rock strength from the first watering of the tunnel system could then have caused the new similar failures from the inspection report in 1986. Examples of the failures can be seen in Figures 6.16 and 10.3 (left). These notches were mostly found in the tunnel upstream of the Sverjesjøen shaft, and the stresses which caused the rock falls were believed to decrease towards the powerhouse area.



**Figure 10.3:** Stress induced rock fall just after the first watering (left) and instability which has developed over time causing inward movement of crown and rock falls (right).

The inspection reports from 1992 and 2017 revealed new stress induced rock falls in the TBM tunnel after the Sverjesjøen shaft. These failures were modelled in the second RS<sup>2</sup> analysis. The model was run with an alternative stress orientation, based on observations of spalling in the powerhouse cavern which suggested that the trend of the major principal stress in the area is N060W. This stress orientation gave no yielded elements and a strength factor above 1 with the same input parameters for the rock mass as in the previous analysis. This indicates a stable tunnel, and the alternative stress orientation could be the reason for the lack of stress induced rock fall in the TBM tunnel after the Sverjesjøen shaft (Uiset HPP is most likely situated in an anti- or syncline from the Caledonian orogeny).

The development of failure over time has been simulated by adding a zone around the tunnel boundary with reduced rock strength, reducing the joint parameters and introducing a water pressure to the joints equal to that of mass oscillations. The water pressure could act as both a pressure increase due to mass oscillations and during a draining situation. The reduction of only the rock mass strength in the zone around the tunnel resulted in yielded elements, which can represent the first sign of spalling. By reducing the joint parameters and adding a water pressure the yielded elements intersected the joint. In addition

it caused the yielding of the joint, where the shear stress changed direction right above the excavation. This change indicates an inward movement of the material underneath the joint, which fits the failure in Figure 10.3 (right).

#### 10.2.4 Structurally controlled rock fall

Block and wedge falls, where high stresses are not a contributor, are only found in the D&B part of the tunnel. As explained in Section 4.2, blasting of the tunnel will induce cracks and fractures and leave the rock mass damaged. It will then be easier for water to enter and weaken the rock mass further. A limit equilibrium analysis of a block fall was conducted to see how weakened the joints had to be, before failing due to a pressure increase from mass oscillations.

Both the stress situation and water pressure in the joints were considered constant. The shear strength of the joints were estimated by the Barton-Bandis joint model. A reduction in JCS would simulate a reduction in the joint wall strength due to alteration by the water and a reduction in JRC and  $\phi_r$  would act as a reduction of the frictional resistance along the joint. The safety factor was affected the most by a reduction in JRC and  $\phi_r$ , and fell below 1 when JRC was reduced from 9 to 6 and the  $\phi_R$  from 26.3 to 20. The stability of the block was not greatly affected by the reduction in JCS. It has to be noted that the results highly depend on the tangential stress.

A similar analysis was conducted in Unwedge to evaluate the effect a pressure increase on the joints would have on the stability of wedges. Unwedge created two wedges which resembled wedge failures that had occurred in the tunnel. The Barton-Bandis joint model was again used to estimate the shear strength of the joints. One wedge failed at once when a pressure was applied. The second wedge was still stable with a pressure of 0.2 MPa, but failed once this pressure was increased to 0.31. A pressure of 0.31 MPa equals the pressure from one upsurge wave due to mass oscillations.

The wedges analysed are not believed to have failed before 1992 or 2017, but the results show that a pressure increase from either the stop of the turbines or dewatering should have led to the failure and recording of the wedges in the 1986 report. The possible explanation could be that the wedges were not fully disjointed from the wall. The effect of the water during mass oscillations could have washed out joint filling and caused the opening of joints. Further pressure changes from mass oscillations may then have caused breaking of rock bridges, destabilisation of the wedges and blocks and finally failure.

#### 10.2.5 Weakness zone

The case study of Svandalsflona HPP shows that the degree of fracturing of a weakness zone is important to the stability of the zone. Water will move more easily in highly fractured zones, wetting infilling or gouge material and possibly lead to washouts. The flow of water through the zone over time could cause weakening of cohesive and frictional properties. The stability is especially in peril if the zone contains swelling clay, which if saturated can swell and generate swelling pressure within the zone.

The weakness zone in the headrace tunnel at Ulset HPP consists of jointed crushed material, but is not highly fractured or altered. There is some new fallen rock from the zone,

but not more than what would be expected. According to Bardal and Bruland (1986) the zone did not show any signs of stability problems, and the stability does not seem to have worsened. Consequently, no further analysis of the stability was conducted in this thesis.

### **10.3 Long-term stability**

The failures experienced during the excavation are a result of high horizontal stresses, which caused spalling and stress induced rock fall in the crown of the headrace tunnel. The failures occurred in connection with weak foliation planes and left the characteristic notches in the crown. The same kind of stress induced failures are described by Bardal and Bruland (1986) in new areas of the tunnel, as a result of saturation of the rock mass from the first watering of the tunnel system. They are especially found in the TBM section between the sand trap and the Sverjesjøen shaft, in connection with a joint system with a trend perpendicular to the tunnel alignment.

Over time this kind of failure, together with spalling and structurally controlled rock falls, developed further and in new areas of the headrace tunnel. The number of structurally controlled rock falls from the D&B tunnel increased in 1992 and further in 2017. The effect of water on the rock mass is mainly concentrated to discontinuities, and water will more easily be able to enter the damaged and fractured rock mass here due to the blasting. The effects of water, which caused the first rock and block falls, are reduction of the normal force on the discontinuity planes, reduction of the rock strength, wetting and erosion of filling material and an increased water pressure on joints during start-and-stop cycles and dewaterings. With an increase in start-and-stop cycles after 1991, the effect of water due to mass oscillations would further aggravate the stability of rocks and blocks by erosion and washing of filling material, increased water pressure and breaking of rock bridges. In addition to the reported rock falls, smaller rocks can be seen in the inspection pictures from 2017 along the entire D&B tunnel (Neupane, 2017). As these rocks are not mentioned in the earlier reports, it can be assumed that an increase in smaller rocks from the detail stability of the tunnel have fallen after the change in production pattern.

New stress induced failures have developed over time in both the TBM and D&B part of the tunnel. The induced fracturing in the crown of the D&B tunnel have after excavation been restrained, but the reduction in strength of the rock mass over time has finally led to the collapse of the roof through the release of rock. Support was installed in some of these areas during construction to avoid spalling, but failed due to the increased load. See Figure 6.17. The development of failures over time is also apparent in the last part of the TBM tunnel. Except for three stress induced notches in the crown within 200 m of the Sverjesjøen shaft, no stress induced failures were reported by Bardal and Bruland (1986) downstream of the shaft. After 6 years of operation Forodden (1992) describes one new case of rock fall in this section of the tunnel. Midtlyng (2017) reports four new rock falls 26 years after the first. This indicates that there has been a slow reduction in strength of the rock mass along the tunnel alignment, which may have accelerated or worsened due to mass oscillations.

The fresh spalling from the inspection notes in 2017 is also an indication of the reduction

in strength of the rock mass. Minor spalling could be the first stage in the development of stress induced rock fall, as have been described above for the last part of the TBM tunnel. It is possible that this instability will evolve into a larger rock fall as seen in Figure 10.4. The fallen rocks are from stress induced failure in the crown in Figure 10.3 (right).



**Figure 10.4:** Rock fall due to stress induced failure in the crown 6230 m downstream of the CSS.

# Conclusions and Recommendations

## 11.1 Conclusion

The major contributors to the instabilities at Ulset HPP is the foliation of the quartzitic schist and the high horizontal stresses. The registered instabilities were systematised into four categories. These categories are spalling, stress induced rock fall, structurally controlled rock fall and weakness zones. The weakness zones were determined to be stable and no further analysis was conducted.

A timeline of the failure- and instability categories was made based on three inspection reports. It can be summarised as follows:

- **1986**  
Rock falls during the excavation and in the first year of operation was due to high horizontal stresses, which induced fractures along the foliation plane and left notches in the crown. These failures can be categorised as stress induced rock falls, and were mostly triggered by joints with trend perpendicular to the tunnel alignment.
- **1992, 2017**  
The reduction in rock mass strength caused the stress induced failure to develop in new parts of the tunnel. It has caused small scale collapses in the D&B tunnel in connection with failure of installed support, and small to medium rock falls in the TBM tunnel.
- **1992, 2017**  
The number of structurally controlled rock falls increases with time, but found only in the D&B tunnel. This is likely as a result of the blasting of the tunnel. The effect of water will easier take a hold on the damaged and fractured rock mass.



- **2017**

Minor spalling has developed in new parts of the tunnel. The spalling could be the first stage in the development of stress induced rock fall, which have occurred in other parts of the tunnel.

Even though there are newly developed failures in 1992, the stability of the tunnel seems to stabilise with a decrease in the number and size of the rock falls. Then the recorded number and size of the rock falls increases in 2017. The increase in rock falls is after the change in power production method, which leads to the belief that mass oscillations can and have influenced the long-term stability of the tunnel. The effects water and mass oscillations may have on the tunnel stability are listed below:

- Reduction of the rock strength
- Reduction of the normal force on discontinuities
- Saturation of filling and gouge material
- Erosion and washout of filling and gouge material
- Increased load on the rock support
- Breaking of rock bridges, connecting joints
- Fluctuating pore pressure, destabilisation of rock blocks

These effects will slowly result in the weakening of the rock mass and affect the long-term stability of the headrace tunnel. The frequency of start-and-stop cycles is here of great importance, as high frequent pressure fluctuations may accelerate the development of instabilities.

## **11.2 Recommendations**

There are many limitations in this thesis, which can be improved with an effort. Improvements of the long-term stability assessment and recommendations for further work are presented below:

- The inspection report from the dewatering in 1987 should be found and incorporated into the timeline, to remove any misinterpretation of the year of recorded failure for the fallen rocks.
- The stability assessment in this thesis have been restricted to failures in unsupported parts of the tunnel. However, many of the larger failures have occurred in connection with support. An analysis of the failed support should be conducted to better evaluate the long-term stability of the headrace tunnel.
- This thesis concluded with that mass oscillations may have an impact on the long-term stability of the tunnel. However, the effect of mass oscillations is not well studied, and further research is necessary to understand the interaction between pressure fluctuations and the rock mass.

# Bibliography

- Alejano, L. R., Muralha, J., Ulusay, R., Li, C. C., Pérez-Rey, I., Karakul, H., Chryssanthakis, P. and Aydan, O. (2018), ISRM suggested method for determining the basic friction angle of planar rock surfaces by means of tilt test, *Rock Mechanics and Rock Engineering* 51(12), pp. 3853–3859. Springer–Verlag.
- Anthony, J. W. (1990), *Handbook of mineralogy : 1 :Elements, sulfides, sulfosalts*, Vol. 1. Tucson, Ariz: Mineral Data Publication. URL: <http://www.handbookofmineralogy.com/pdfs/lepidocrocite.pdf> [Accessed: 12.03.2019].
- Bardal, R. and Bruland, A. (1986), *Tunnelbefaring i tilløpstunnel Ulset kraftverk 20.06.86. (Tunnel inspection in headrace tunnel Ulset Hydropower Station 20.06.2018)*, Part of research project on "Rock support of Water Tunnels" for the Norwegian Hydropower Owners Association. Unpublished.
- Barton, N. (1972), A model study of rock-joint deformation, *International Journal of Rock Mechanics and Mining Sciences and Geomechanics Abstracts* 9(5), pp. 579–582.
- Barton, N. (1988), *Predicting the Behaviour of Underground Openings in Rock*, Norwegian Geotechnical Institute. Publication No 172.
- Barton, N. (2002), Some new Q-value correlations to assist in site characterisation and tunnel design, *International Journal of Rock Mechanics and Mining Sciences* 39(2), pp. 185–216.
- Barton, N. and Choubey, V. (1977), The shear strength of rock joints in theory and practice, *Rock mechanics* 10(1), pp. 1–54.
- Barton, N., Lien, R. and Lunde, J. (1974a), Engineering classification of rock masses for the design of tunnel support, *Rock Mechanics and Rock Engineering* 6(4), pp. 189–263.
- Barton, N., Lien, R. and Lunde, J. (1974b), Engineering classification of rock masses for the design of tunnel support, *Rock Mechanics and Rock Engineering* 6(4), pp. 189–263.

- 
- Basnet, C. B. and Panthi, K. K. (2019), Evaluation on the minimum principal stress state and potential hydraulic jacking from the shotcrete-lined pressure tunnel: A case from nepal, *Rock Mechanics and Rock Engineering* .
- Bieniawski, Z. T. (1993), Classification of rock masses for engineering: The RMR-system and future trends, *Comprehensive rock engineering* Vol. 3, ed. J.A. Hudson, pp. 553–573.
- Bieniawski, Z. T. (1978), Determining rock mass deformability: experience from case histories, *International Journal of Rock Mechanics and Mining Sciences and Geomechanics Abstracts* 15(5), pp. 237–247.
- Bjerkegård, T. and Bjørlykke, A. (1994), Geology of the folldal area, southern trondheim region caledonides, *Nor. geol. unders. Bull.* 426 pp. pp. 53–75.
- Broch, E. (1979), Changes in rock strength caused by water, *Proceedings of the 4th Congress of the International Society for Rock Mechanics, Montreux* 4, pp. 71–75.
- Broch, E. (1982), Designing and excavating underground powerplants, *Water Power & Dam Construction* pp. 19–25. Norwegian Institute of Technology, University of Trondheim, NTH, Norway.
- Broch, E. (1985), Development of unlined pressure shafts and tunnels in norway, *Norwegian Hydropower Tunnelling, Publication No.3* . Trondheim: Norwegian Soil and Rock Engineering Association. Tapir.
- Broch, E. (2006), Why did the hydropower industry go underground?, *Sustainable underground concepts, Publication No. 15* . Oslo: Norwegian Tunnelling Society.
- Broch, E. (2013), Underground hydropower projects – lessons learned in home country and from projects abroad, *Norwegian Hydropower Tunnelling II, Publication No. 22*. Ed. by E. Broch, E. Grاسبakken and W. Stefanussen. Oslo: Norwegian Tunnelling Society, pp. 11–19.
- Bruland, A. and Thidemann, A. (1991), *Sikring av vanntunneler (Support of watertunnels)*, Vassdragsregulantenenes forening (VR).SINTEF report. 88 p.
- Bråtveit, K., Bruland, A. and Brevik, O. (2016), Rock falls in selected norwegian hydropower tunnels subjected to hydropeaking, *Tunneling and Underground Space Technology* 52, pp. 202–207.
- Cai, M., Kaiser, P. K., Tasaka, Y. and Minami, M. (2007), Determination of residual strength parameters of jointed rock masses using the gsi system, *International Journal of Rock Mechanics and Mining Sciences* 44(2), pp. 247–265.
- Dahlø, T. S., Goodall, D. C. and Kjørholt, H. (1988), *Air and gas tightness of unlined rock caverns - Ulset air cushion surge chamber*, Unpublished. SINTEF, Rock and Mineral Engineering.

- 
- Diederichs, M. (2007), The 2003 canadian geotechnical colloquium: Mechanistic interpretation and practical application of damage and spalling prediction criteria for deep tunnelling, *Canadian Geotechnical Journal* 44(9), pp. 1082–1116.
- Diederichs, M. (2014), When does brittle failure become violent? spalling and rockburst characterization for deep tunneling projects, *Proceedings of the World Tunnel Congress 2014 – Tunnels for a better Life* . Foz do Iguazu, Brazil.
- Edelbro, C. (2010), Different approaches for simulating brittle failure in two hard rock mass cases: A parametric study, *Rock Mechanics and Rock Engineering* 43(2), pp. 151–165.
- Eiken, A., Berge, B. H. and Bredeveien, J. (1986), *Orkla utbyggingen - en oversikt over utbyggingen og kostnadene*, Booklet. Kraftverkene i Orkla.
- Forodden, H. (1992), *Tunnelinspeksjon - Tilløpstunnel Ulset - 19/8-92 (Tunnel inspection - Headrace tunnel Ulset Hydropower Station 19/8-92)*, Unpublished, for Sør-Trøndelag kraftselskap, KVO.
- Goodall, D. C., Kjørholt, H., Tekle, T. and Broch, E. (1988), Air cushion surge chambers for underground power plants, *International Water Power and Dam Construction* 40(11), pp. 29–34.
- Goodman, R. E. (1989), *Introduction to rock mechanics.*, Wiley, New York.
- Guttormsen, O. (2006), *TVM4165 Vannkraftverk og Vassdragsteknikk GK - Vassdragsteknikk II*, Course compendium. Trondheim: Tapir, Kompendieforlaget.
- Halseth, R. T. (2018), *Stability assesment of the headrace tunnel system at Brattset Hydropower Project*, Master thesis. Trondheim: Norwegian University of Science and Technology.
- Hammett, R. D. and Hoek, E. (1981), *Design of large underground caverns for hydroelectric projects with particular reference to structurally controlled failure mechanisms*, New York: ASCE Spring Convention, Session on Rock Mechanics of Large Hydro Projects.
- Hansen, S. E. and Hanssen, T. H. (1988), Hydraulisk splitting (eng: Hydraulic fracturing), *Fjellsprengningskonferansen - Bergmekanikkdagen - Geoteknikkdagen 1988* pp. Ed. by K. R. Berg et al. Norsk Jord- og Fjellteknisk Forbund. Oslo: Tapir, pp. 26.1–26.15.
- Helwig, P. C. (1987), A theoretical investigation into the effects of water hammer pressure surges on rock stability of unlined tunnels, *Underground hydropower plants. Proceedings of the Int. Conference on Hydropower (Hydropower '87)* pp. Ed. by E. Broch and D.K. Lysne. pp. 811–828.
- Hoek, E. (2007a), Structurally controlled instability in tunnels. RocScience. *Practical rock engineering*, URL: <https://www.rocscience.com/assets/resources/learning/hoek/Practical-Rock-Engineering-Full-Text.pdf>.
-

- 
- Hoek, E. (2007b), *Practical rock engineering*, URL: <https://www.rocscience.com/assets/resources/learning/hoek/Practical-Rock-Engineering-Full-Text.pdf>.
- Hoek, E. and Brown, E. T. (1980), *Underground Excavations in Rock*, London: Institution of mining and metallurgy.
- Hoek, E. and Brown, E. T. (1997), Practical estimates of rock mass strength, *International Journal of Rock Mechanics and Mining Sciences* 34(8), pp. 1165–1186.
- Hoek, E., Carranza-Torres, C. and Corkum, B. (2002), Hoek-brown failure criterion – 2002 edition, *Proc. NARMS-TAC Conference*. pp. Ed. by Hammah et al. Toronto: University of Toronto. pp. 267–273.
- Hudson, J. A. and Harrison, J. P. (1997), *Engineering rock mechanics: an introduction to the principles*, Oxford: Elsevier Ltd.
- ISMR (1978), Suggested methods for the quantitative description of discontinuities in rock masses, *International Journal of Rock Mechanics and Mining Sciences & Geomechanics Abstracts* 15(6), pp. 319–368.
- ISRM (1977), Suggested methods for the quantitative description of discontinuities in rock masses, *International Journal of Rock Mechanics and Mining Sciences and Geomechanics Abstracts* 15(6), pp. 319–368.
- ISRM (1978), Suggested method for determining tensile strength of rock materials, *International Journal of Rock Mechanics and Mining Sciences and Geomechanics Abstracts* 15, pp. 99–103.
- ISRM (1979), Suggested methods for determining the uniaxial compressive strength and deformability of rock materials, *International Journal of Rock Mechanics and Mining Sciences and Geomechanics Abstracts* 16(2), pp. 137–140.
- ISRM (1985), Suggested method for determining point load strength, *International Journal of Rock Mechanics and Mining Sciences and Geomechanics Abstracts* 22(2), pp. 51–60.
- Jaeger, J. C. (1977), *Fluid transients in hydro-electric engineering practice*, Glasgow and London:Blackie. p.413.
- Jaeger, J. C., Cook, N. G. W. and Zimmerman, R. (2007), *Fundamentals of Rock Mechanics*, (4th ed.). Malden, MA: Blackwell Pub.
- Jing, L. (2003), A review of techniques, advances and outstanding issues in numerical modelling for rock mechanics and rock engineering, *International Journal of Rock Mechanics and Mining Sciences* 40(3), pp. 283–353.
- Kartverket (n.d.), *Norge i bilder.*, Topographical map in 3D. URL: <https://www.norgeibilder.no/> [Accessed: 11.11.2018].
-

- 
- Kjøllberg, R. S. (1985), Experience after 14 years in use of the headrace tunnel at rendalen hydro power plant, *Fjellsprengningskonferansen - Bergmekanikkdagen - Geoteknikkdagen 1985* pp. pp. 39.1–11.
- Lajtai, E. Z., Schmidtke, R. H. and Bielus, L. P. (1987), The effect of water on the time-dependent deformation and fracture of a granite, *International Journal of Rock Mechanics and Mining Sciences and Geomechanics Abstracts* 24(4), pp. 247–255.
- Lavina, B., Dera, P. and Downs, R. T. (2014), Modern x-ray diffraction methods in mineralogy and geosciences, *Reviews in Mineralogy and Geochemistry* 78, pp. 1–31.
- Li, C. C. (2017a), Principles of rockbolting design, *Journal of Rock Mechanics and Geotechnical Engineering* 9(3), pp. 396–414.
- Li, C. C. (2017b), *Rock Mechanics*, Compendium in TGB4210 - Rock Mechanics. Trondheim: Norwegian University of Science and Technology.
- Martin, C. D. and Christiansson, R. (2009), Estimating the potential for spalling around a deep nuclear waste repository in crystalline rock, *International Journal of Rock Mechanics and Mining Sciences* 46(2), pp. 219–228.
- Midtlyng, A. (2017), *Notes from tunnel inspection 17-10-2017.*, Unpublished.
- Myrset, O. (1980), *Underground Hydro-Electric Power Stations In Norway*, Stockholm, Sweden: International Society for Rock Mechanics and Rock Engineering(ISRM). Rockstore 80.
- Myrvang, A. M. (2001), *Bergmekanikk (Rock mechanics)*.
- Neupane, B. (2017), *Notes and pictures from tunnel inspection 17-10-2017.*, Unpublished.
- Neupane, B. and Panthi, K. K. (2018), Effect of pressure fluctuations in long-term stability of unlined pressure shaft at svandalsflona hydropower project, norway., *The 2018 ISRM International Symposium 2018 ISRM & SRMEG* pp. Singapor. pp. 923–932.
- NGI (2015), *Using the Q-system. Rock mass classification and support design*, Handbook. Oslo.
- NGU (2013), Geological map of norway, URL: <https://www.ngu.no/nyheter/berggrunn>, [Accessed 02.12.2018].
- NGU (2019), *Quaternary map. (Kvartærgeologisk kart)*, URL: <http://geo.ngu.no/kart/losmasse/> [Accessed: 07.03.2019].
- Nilsen, B. (2016), *Ingeniørgeologi - berg, grunnkurskompendium*, Trondheim: Institute for geology and rock mechanics. Norwegian University of Science and Technology.
- Nilsen, B. and Palmström, A. (2000), *Engineering geology and Rock Engineering; Handbook No. 2*, Oslo: Norweegian group of rock mechanics.
-

- 
- Nilsen, B. and Thidemann, A. (1993), *Rock Engineering.*, Vol. 9. Hydropower development. Trondheim: Norwegian Institute of Technology, Department of Hydraulic Engineering.
- Nilsen, O. (1988), The tectonostratigraphic setting Of stratabound sulphide deposits in the southern trondheim region, central norwegian caledonides, *Nor. geol. unders. Bull.* 426 pp. pp. 53–75.
- Nilsen, O. and Wolff, F. C. (1989), *Røros og Sveg*, Berggrunnskart Røros og Sveg M 1:250 000: trykt i farger. URL: <https://www.ngu.no/publikasjon/r-ros-og-sveg-berggrunnskart-r-ros-og-sveg-1250-000-trykt-i-farger>.
- NVE (2019), *Vannkraftpotensialet*, URL: <https://www.nve.no/energiforsyning/vannkraftpotensialet/>, [Accessed 30.4.2019].
- Palmstrøm, A. and Broch, E. (2017), The design of unlined hydropower tunnels and shafts: 100 years of norwegian experience, *Hydropower & Dams Issue Three* .
- Palmstrøm, A. and Schance, K. (1987), Design features at tjodan save time and money, *Int. Water Power and Dam Construction* 39(6), pp. 19–24.
- Palmstrøm, A. and Stille, H. (2010), *Rock engineering*, ICE Publishing.
- Panthi, K. K. (2006), *Analysis of engineering geological uncertainties related to tunnelling in Himalayan rock mass conditions*, Doctoral thesis. Trondheim: Norwegian Institute of Technology.
- Panthi, K. K. (2014a), Analysis on the dynamics of burst debris flood at the inclined pressure-shaft of svandalsflona hydropower project, norway., *Rock Mechanics and Rock Engineering* 47(3), pp. 923–932.
- Panthi, K. K. (2014b), Norwegian design principle for high pressure tunnels and shafts: Its applicability in the himalaya, *Hydro Nepal: Journal of Water, Energy and Environment* 14 .
- Panthi, K. K. (2018), Rockburst prediction methods and their applicability, in Feng, X.-T. (Ed.), *Rockburst - Mechanisms, Monitoring, Warning, and Mitigation*. Elsevier. pp. 381-385.
- Popescu, M., Arsenie, D. and Vlase, P. (2003), *Applied Hydraulic Transients*, Lisse: A.A. Balkema Publishers.
- Rahmani, N., Nikbakhtan, B., Ahangari, K. and Apel, D. (2012), Comparison of empirical and numerical methods in tunnel stability analysis, *International Journal of Mining, Reclamation and Environment* 26(3), pp. 261–270.
- Rasten, B. (2014), *Virkning av hydrauliske transienter på inntaksluker på Tonstad kraftverk*, Master thesis. Trondheim: Norwegian University of Science and Technology.

- 
- Rocscience (n.d.a), Rs2 v9.0 webhelp, URL: <https://www.rocscience.com/help/rs2/>, [Accessed 1.4.2019].
- Rocscience (n.d.b), Unwedge helppage at rocscience.com, URL: <https://www.rocscience.com/help/unwedge/>, [Accessed: 18.05.2019].
- Selmer-Olsen, R. (1974), Underground openings filled with high-pressure water or air, *Bulletin of the International Association of Engineering Geology*, Issue 9 pp. 91–95.
- Sinha, R. S. (1989), *Underground Structures design and implementation*. (ed. Sinha, R S), Amsterdam: Elsevier.
- Siren, T., Kantina, P. and Rinne, M. (2015), Considerations and observations of stress-induced and construction-induced excavation damage zone in crystalline rock, *International Journal of Rock Mechanics and Mining Sciences* 73, pp.165–174.
- Trinh, Q. N. and Holmøy, K. H. (2012), Numerical modeling in rock engineering: what it can do, advantages and disadvantages, and software limitations, *Fjellsprengningsdagen - Bergmekanikkdagen - Geoteknikkdagen 2012* p. Norwegian Tunneling society.
- Trønderenergi (2018), Ulset HPP, Information page about Ulset Hydropower Project. URL: <https://tronderenergi.no/produksjon/kraftverk/ulset>, [Accessed 15.10.2018].
- Trønderenergi (2019), Rendalen HPP, Information page about Rendalen hydropower project. URL: <http://www.opplandenergi.no/Kraftverksoversikt/Rendalen/>, [Accessed 23.05.2019].



---

## Appendix A - Field work

### Field observations

**Table A.1:** List of locations with coordinates, measurements and rock types, quartzitic schist (QS) and Trondhjemite.

| Location | Coordinates            | Rock type           | Strike/dip                                       |                                     |  |
|----------|------------------------|---------------------|--|-------------------------------------|--|
|          |                        |                     | Foliation joints                                 | Joints                              |  |
| 1        | E 0571557<br>N 6942778 | QS                  | N090E/20N<br>N092E/18N<br>N110E/12N<br>N098E/16N | N112E/72S<br>N110E/70S<br>N094E/70S | N050E/84SE<br>N048E/80SE<br>N045E/82SE |
| 2        | E 0571416<br>N 6942643 | QS                  | N140E/24SW*                                      | N022E/90                            |  |
| 3        | E 0571490<br>N 6942524 | QS                  | N070E/12N<br>N088E/13N                           | N130E/86NE<br>N132E/84NE            | N046E/88NW<br>N040E//90                |
| 4        | E 0571493<br>N 6942216 | QS                  |  |                                     | N040E/82NW<br>N050E/76NW               |
| 5        | E 0568600<br>N 6943729 | Trondhjemite        |  | N120E/71SW                          |  |
| 6        | E 0568412<br>N 6943915 | Trondhjemite        |  |                                     |  |
| 7        | E 0568342<br>N 6943983 | Trondhjemite/<br>QS | N195E/12E  |                                     |  |
| 8        | E 0568519<br>N 6943898 | QS                  | N200E/12E<br>N210/14E                            |                                     |  |
| 9        | E 0568597<br>N 6943911 | QS                  | N155E/15NE<br>N145E/14NE<br>N065E/15SE*          |                                     |  |
| 10       | E 0568580<br>N 6943958 | QS                  |  | N130E/80NE                          | N030E/72SE<br>N030E/70SE               |
| 11       | E 0568696<br>N 6943315 | QS                  | N030E/16E<br>N020E/15E                           |                                     |  |
| 12       | E 0568701<br>N 6942325 | Trondhjemite/<br>QS | N170E/30E<br>N180E/30E                           |                                     |  |
| 13       | E 0568775<br>N 6941672 | QS                  | N010E/20E  | N032E/84SE                          |  |
| 14       | E 0564357<br>N 6943928 | Trondhjemite/<br>QS | N170E/10E<br>N178E/12E                           | N170E/70E<br>N130E/42SW             |  |

## Engineering geological map

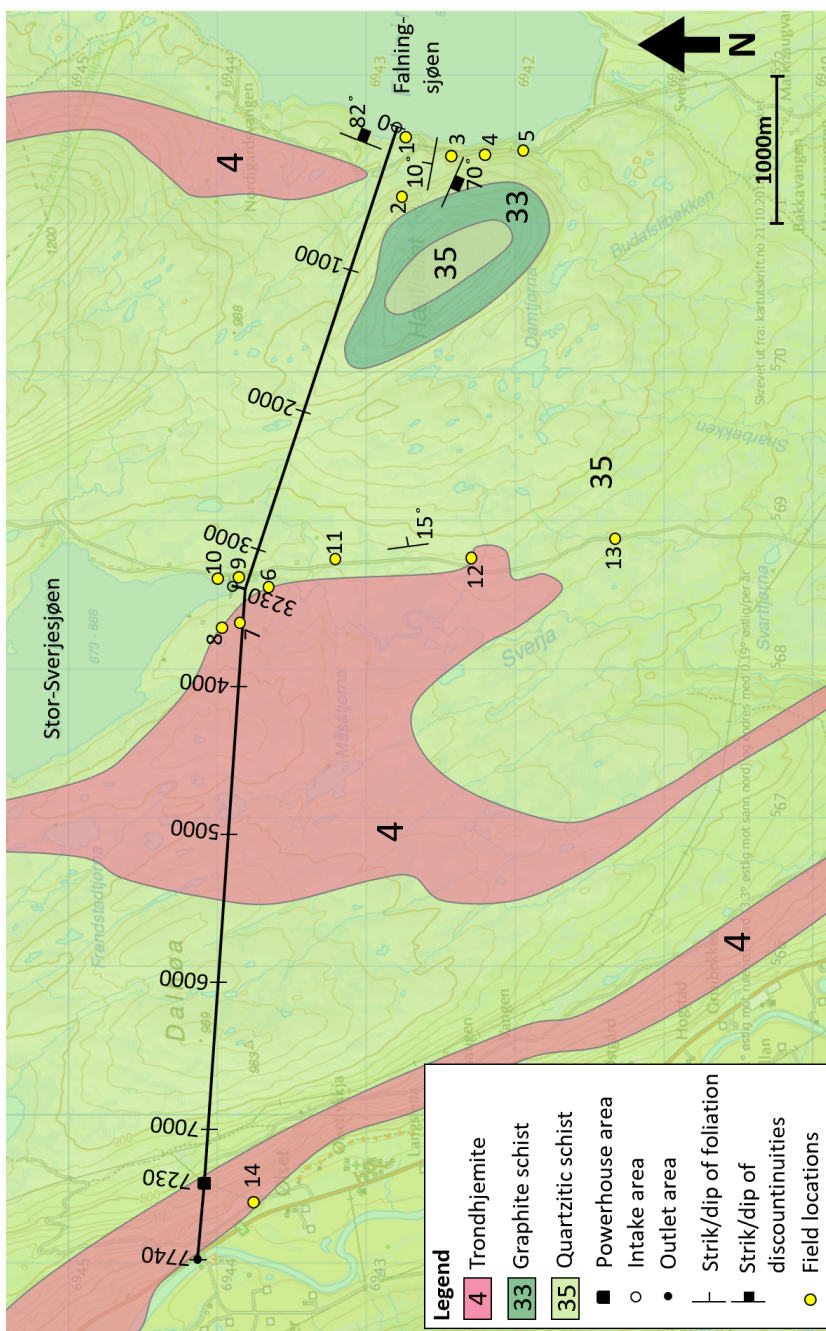
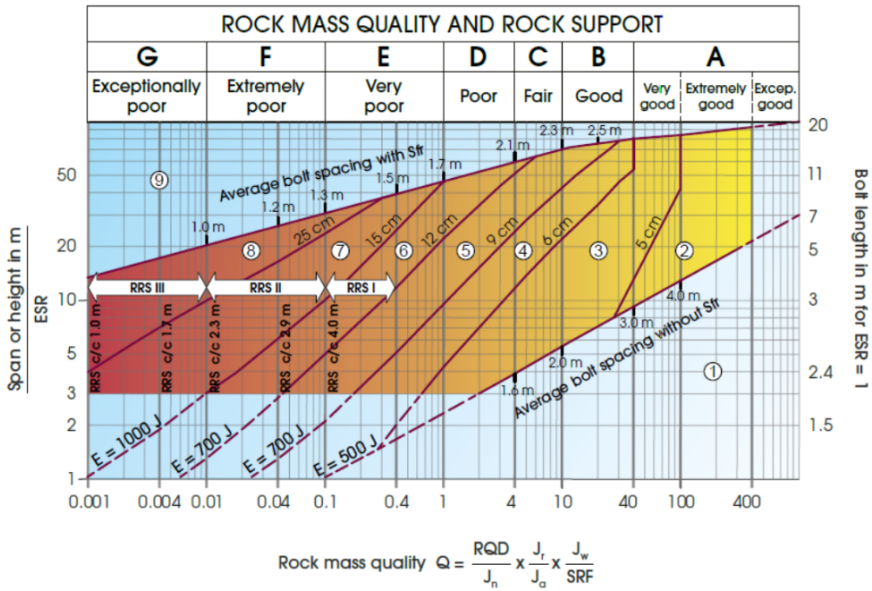


Figure A.1: Engineering geological map of project area with field locations

## Q-system classification and input values



### Support categories

- ① Unsupported or spot bolting
- ② Spot bolting, **SB**
- ③ Systematic bolting, fibre reinforced sprayed concrete, 5-6 cm, **B+Sfr**
- ④ Fibre reinforced sprayed concrete and bolting, 6-9 cm, **Sfr (E500)+B**
- ⑤ Fibre reinforced sprayed concrete and bolting, 9-12 cm, **Sfr (E700)+B**
- ⑥ Fibre reinforced sprayed concrete and bolting, 12-15 cm + reinforced ribs of sprayed concrete and bolting, **Sfr (E700)+RRS I +B**
- ⑦ Fibre reinforced sprayed concrete >15 cm + reinforced ribs of sprayed concrete and bolting, **Sfr (E1000)+RRS II+B**
- ⑧ Cast concrete lining, **CCA** or **Sfr (E1000)+RRS III+B**
- ⑨ Special evaluation

Bolts spacing is mainly based on Ø20 mm

E = Energy absorption in fibre reinforced sprayed concrete

ESR = Excavation Support Ratio

Areas with dashed lines have no empirical data

RRS - spacing related to Q-value

- |     |  |
|-----|--|
| I   | <b>S130/6 Ø16 - Ø20 (span 10m)</b><br>D40/6+2 Ø16-20 (span 20m)                              |
| II  | <b>S135/6 Ø16-20 (span 5m)</b><br><b>D45/6+2 Ø16-20 (span 10m)</b><br>D55/6+4 Ø20 (span 20m) |
| III | D40/6+4 Ø16-20 (span 5m)<br><b>D55/6+4 Ø20 (span 10m)</b><br>Special evaluation (span 20m)   |

S130/6 = Single layer of 6 rebars, 30 cm thickness of sprayed concrete

D = Double layer of rebars

Ø16 = Rebar diameter is 16 mm

c/c = RSS spacing, centre - centre

**Figure A.2:** Rock mass quality and rock support categories (NGI, 2015).

**Rock quality designation (RQD)**

|  |               |
|--|---------------|
| Very poor  | RQD = 0 - 25% |
| Poor   | 25 - 50       |
| Fair   | 50 - 75       |
| Good   | 75 - 90       |
| Excellent  | 90 - 100      |
| <b>Notes:</b>  |               |
| (i) Where RQD is reported or measured as < 10 (including 0), a nominal value of 10 is used to evaluate Q |               |
| (ii) RQD intervals of 5, i.e. 100, 95, 90, etc. are sufficiently accurate                                |               |

**Joint set number (Jn)**

|  |              |
|--|--------------|
| Massive, no or few joints  | Jn = 0.5 - 1 |
| One joint set  | 2            |
| One joint set plus random  | 3            |
| Two joint sets   | 4            |
| Two joint sets plus random   | 6            |
| Three joint sets   | 9            |
| Three joint sets plus random   | 12           |
| Four or more joint sets, heavily jointed, "sugar-cube", etc.                                 | 15           |
| Crushed rock, earthlike  | 20           |
| <b>Notes:</b> (i) For tunnel intersections, use (3.0 x Jn); (ii) For portals, use (2.0 x Jn) |              |

**Description and ratings for the parameter Jr (joint roughness number)**

|  |        |   |          |
|--|--------|---|----------|
| <b>a) Rock-wall contact,</b>   |        | <b>c) No rock-wall contact when sheared</b>   |          |
| <b>b) rock-wall contact before 10 cm shear</b>   |        |   |          |
| Discontinuous joints   | Jr = 4 | Zone containing clay minerals thick enough to prevent rock-wall contact   | Jr = 1.0 |
| Rough or irregular, undulating   | 3      |   |          |
| Smooth, undulating   | 2      |   |          |
| Slickensided, undulating   | 1.5    |   |          |
| Rough or irregular, planar   | 1.5    |   |          |
| Smooth, planar   | 1.0    | Sandy, gravelly or crushed zone thick enough to prevent rock-wall contact   | 1.0      |
| Slickensided, planar   | 0.5    |   |          |
| <b>Note:</b> i) Descriptions refer to small scale features, and intermediate scale features, in that order |        | <b>Notes:</b>   |          |
|  |        | i) Add 1.0 if the mean spacing of the relevant joint set is greater than 3 m  |          |
|  |        | ii) Jr = 0.5 can be used for planar, slickensided joints having lineations, provided the lineations are orientated for minimum strength |          |

**Descriptions and ratings for the parameter Ja (joint alteration number)**

| Contact between joint walls   | JOINT WALL CHARACTER    |   | Condition                                | Wall contact                                 |                                  |
|-------------------------------|-------------------------|---|--|--|----------------------------------|
|                               | CLEAN JOINTS            | Healed or welded joints:                                  | filling of quartz, epidote, etc.         |  | Ja = 0,75                        |
| Fresh joint walls:            |                         | no coating or filling, except from staining (rust)        |  | 1  |                                  |
| Slightly altered joint walls: |                         | non-softening mineral coatings, clay-free particles, etc. |  | 2  |                                  |
| COATING OR THIN FILLING       |                         | Friction materials:                                       | sand, silt calcite, etc. (non-softening) |  | 3                                |
|                               | Cohesive materials:     | clay, chlorite, talc, etc. (softening)                    |  | 4  |                                  |
| Partly or no wall contact     | FILLING OF:             |   | Type                                     | Partly wall contact<br>Thin filling (< 5 mm) | No wall contact<br>Thick filling |
|                               | Friction materials      | sand, silt calcite, etc. (non-softening)                  |  | Ja = 4                                       | Ja = 8                           |
|                               | Hard cohesive materials | compacted filling of clay, chlorite, talc, etc.           |  | 6  | 5 - 10                           |
|                               | Soft cohesive materials | medium to low overconsolidated clay, chlorite, talc, etc. |  | 8  | 12                               |
|                               | Swelling clay materials | filling material exhibits swelling properties             |  | 8 - 12                                       | 13 - 20                          |

**Description and ratings for the parameter Jw (joint water reduction factor)**

|  |  |                           |            |
|--|--|---------------------------|------------|
| Dry excavations or minor inflow, i.e. < 5 l/min locally  |  | $p_w < 1 \text{ kg/cm}^2$ | Jw = 1     |
| Medium inflow or pressure, occasional outwash of joint fillings  |  | 1 - 2.5                   | 0.66       |
| Large inflow or high pressure in competent rock with unfilled joints                                       |  | 2.5 - 10                  | 0.5        |
| Large inflow or high pressure, considerable outwash of joint fillings                                      |  | 2.5 - 10                  | 0.3        |
| Exceptionally high inflow or water pressure at blasting, decaying with time                                |  | > 10                      | 0.2 - 0.1  |
| Exceptionally high inflow or water pressure continuing without noticeable decay                            |  | > 10                      | 0.1 - 0.05 |
| <b>Note:</b> (i) The last four factors are crude estimates. Increase Jw if drainage measures are installed |  |                           |            |
| (ii) Special problems caused by ice formation are not considered   |  |                           |            |

**Description and ratings for parameter SRF (stress reduction factor)**

|   |   |                               |                              |           |
|---|---|-------------------------------|------------------------------|-----------|
| A. Weakness zones intersecting excavation   | Multiple weakness zones with clay or chemically disintegrated rock, very loose surrounding rock (any depth) | SRF = 10                      |                              |           |
|   | Single weakness zones containing clay or chemically disintegrated rock (depth of excavation < 50 m)         | 5                             |                              |           |
|   | Single weakness zones containing clay or chemically disintegrated rock (depth of excavation > 50 m)         | 2.5                           |                              |           |
|   | Multiple shear zones in competent rock (clay-free), loose surrounding rock (any depth)                      | 7.5                           |                              |           |
|   | Single shear zones in competent rock (clay-free), loose surrounding rock (depth of excavation < 50 m)       | 5                             |                              |           |
|   | Single shear zones in competent rock (clay-free), loose surrounding rock (depth of excavation > 50 m)       | 2.5                           |                              |           |
|   | Loose, open joints, heavily jointed or "sugar-cube", etc. (any depth)                                       | 5                             |                              |           |
| <b>Note:</b> (i) Reduce these values of SRF by 25 - 50% if the relevant shear zones only influence, but do not intersect the excavation   |   |                               |                              |           |
| B. Competent rock, rock stress problems   | Low stress, near surface, open joints   | $\sigma_c / \sigma_1 > 200$   | $\sigma_0 / \sigma_c < 0.01$ | 2.5       |
|   | Medium stress, favourable stress condition  | 200 - 10                      | 0.01 - 0.3                   | 1         |
|   | High stress, very tight structure. Usually favourable to stability, may be except for walls                 | 10 - 5                        | 0.3 - 0.4                    | 0.5 - 2   |
|   | Moderate slabbing after > 1 hour in massive rock  | 5 - 3                         | 0.5 - 0.65                   | 5 - 50    |
|   | Slabbing and rock burst after a few minutes in massive rock   | 3 - 2                         | 0.65 - 1                     | 50 - 200  |
|   | Heavy rock burst (strain burst) and immediate dynamic deformation in massive rock                           | < 2                           | > 1                          | 200 - 400 |
| <b>Notes:</b> (ii) For strongly anisotropic stress field (if measured): when $5 < \sigma_1 / \sigma_3 < 10$ , reduce $\sigma_c$ to 0.75 $\sigma_c$ .<br>(iii) When $\sigma_1 / \sigma_3 > 10$ , reduce $\sigma_c$ to 0.5 $\sigma_c$ .<br>(iii) Few case records available where depth of crown below surface is less than span width. Suggest SRF increase from 2.5 to 5 for low stress cases |   |                               |                              |           |
| C. Squeezing rock   | Plastic flow of incompetent rock under the influence of high pressure                                       | Mild squeezing rock pressure  | 1 - 5                        | 5 - 10    |
|   |   | Heavy squeezing rock pressure | > 5                          | 10 - 20   |
| D. Swelling rock  | Chemical swelling activity depending on presence of water   | Mild swelling rock pressure   |                              | 5 - 10    |
|   |   | Heavy swelling rock pressure  |                              | 10 - 15   |

**Figure A.3:** Input values used in the estimation of q-value.

# Appendix B - Longitudinal profile

## Longitudinal profile

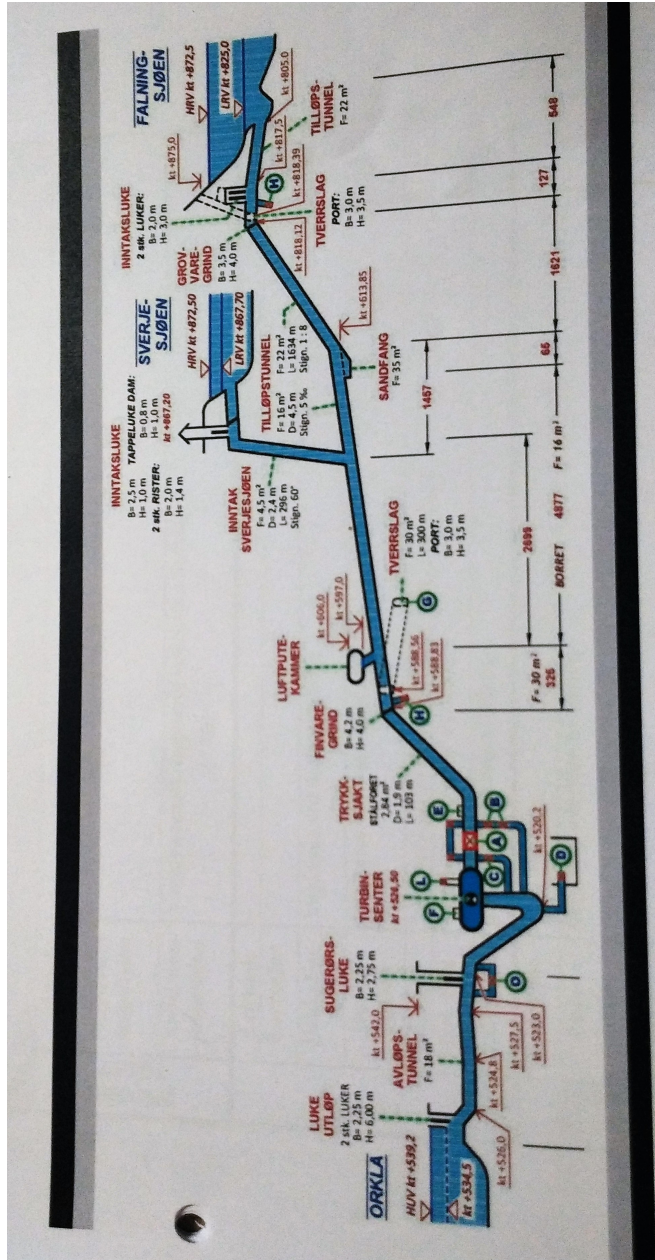


Figure B.1: Longitudinal profile of the water system at Ulset HPP.



## Geological cross-section

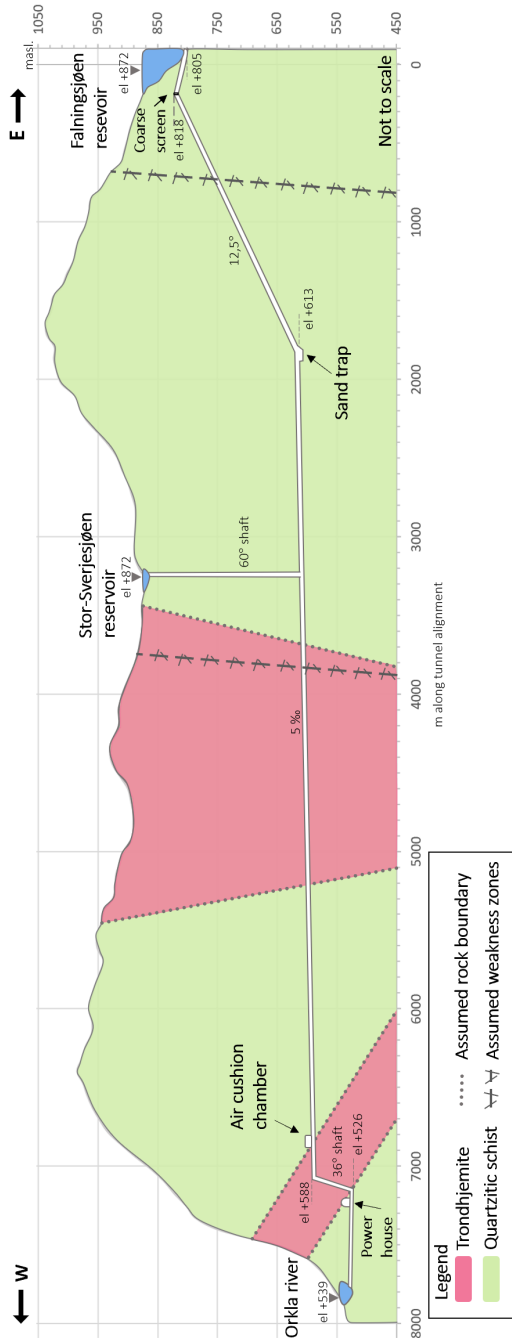


Figure B.2: Cross-section of Ulset HPP, from the coarse sediment screen to the outlet area.

## Appendix C - Instabilities and failures in the tunnel

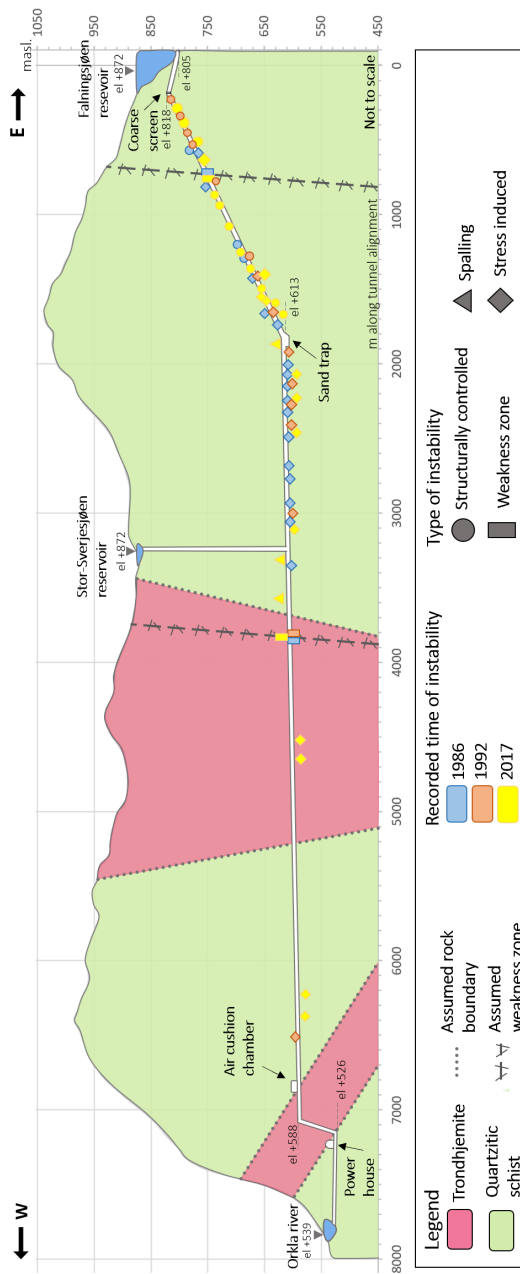


Figure C.1: Location of failures and instabilities in the waterway system at Ulset HPP.



## List of observed failures

| Chainage from coarse screen [m] | Year of recorded instability/failure | Type of instability | Size [m <sup>3</sup> ] | Comment  |
|---------------------------------|--------------------------------------|---------------------|------------------------|--|
| 46                              | 1992                                 | SC                  | 2                      | Rock fall from left wall. 0.2 m thick.   |
| 229                             | 2017                                 | SC                  | 3                      | Block fall from roof. Thick rectangular blocks, together with smaller rocks.               |
| 275                             | 2017                                 | SC                  | 0.5                    | Rock fall from left wall. (0.2x3x1 m)  |
| 320                             | 2017                                 | SC                  | 1                      | Rock fall from roof  |
| 350                             | 1992                                 | SC                  | 2-3                    | Rock fall left wall  |
| 398                             | 1992                                 | SC                  | 2-3                    | Rock fall  |
| 400                             | 1986                                 | SC                  | 0.5                    | Small rock fall.   |
| 450                             | 1986, 2017                           | SI                  | 5, 55                  | 4-5 rock falls from high stresses, major horizontal stress is parallel with the foliation. |
| 470-520                         | 2017                                 | SI                  | 240                    | Notch in roof. Large collection of debris from rock falls and gravel road.                 |
| 535                             | 1986,2017                            | WZ                  | -                      | 20 m cast-concrete, wash-out from behind concrete.   |
| 600                             | 1992                                 | SC                  | -                      | Rock fall over cable.  |
| 620                             | 1986                                 | SI                  |                        | Small rock falls caused by high stresses.  |
| 680-780                         | 2017                                 | SC                  | 0.5                    | Smaller rock falls from walls.   |
| 850                             | 1986,2017                            | -                   |                        | Leakage, sulfuric smell.   |
| 902                             | 2017                                 | SC                  | 0.01-0.1               | Small rock falls   |
| 994                             | 1986                                 | SC                  |                        | Two small rocks from roof.   |
| 1039                            | 2017                                 | SC                  |                        | Thin long sheets.  |
| 1100                            | 1986,1992                            | SC                  |                        | Rock fall during dewatering, less schistosity. (1.5x1x0.2 m)                               |
| 1150                            | 2017                                 | SC                  | 3                      | Large block fall from roof/hanging wall.   |
| 1192                            | 1986,1992,2017                       | SI                  | 1,10,30                | Large rock falls, highly schistose. (sheets peeled of)                                     |
| 1284                            | 2017                                 | SC                  | 6                      | Thin sheets peeled of right wall, (1.5x1.5x0.1m).  |

**Figure C.2:** Overview of failures from the coarse sediment screen to 1284 m, together with year of recorded failure and approximately size. Structurally controlled (SC), Stress induced (SI), weakness zone (WZ) and spalling (SP).

|           |                |    |     |  |
|-----------|----------------|----|-----|--|
|           |                |    |     | Smaller rocks from roof.   |
| 1315      | 2017           | SI | 10  | Notch in roof.   |
| 1345      | 2017           | SI | 5   | Notch in roof. Sharp edges and flakey rocks.                                 |
| 1361      | 2017           | SC | 2-3 | Rock fall from right wall (1x1x0.2).   |
| 1452      | 1986,1992      | SI |     |  |
| 1468      | 2017           | SC |     | Large sheet in right wall (2x1.5x0.1).                                       |
| 1520      | 1986           | SI |     | Middle size rock from high stresses in roof.                                 |
| 1621      | 2017           | SP |     | Slight spalling in roof above the sand trap have caused some fallout.        |
| 1715      | 1992,2017      | SI | 10  | Long thin block, some are newer.   |
| 1860-3000 | 1986           | SI | 70  | A total of 19(110m) notches in left hanging wall. Forming thin sharp sheets. |
| 1860-3000 | 1992           | SI | 4-5 | Five new notches.  |
| 1860-3000 | 2017           | SI | 4   | Some newer sheets.   |
| 3100      | 2017           | SP |     | New thin sheets forming on surface.  |
| 3150      | 1986           | SI |     | Three notches (total 15m) close to the Sverjesjøen intake.                   |
| 3489      | 2017           | SP |     | Spalling damage in roof.   |
| 3888      | 1986,1992,2017 | WZ | 8   | Some leakage and rock fall.  |
| 4293      | 2017           | SI | 6   | Fresh sheet/flake  |
| 4473      | 2017           | SI | 1   | Fresh sheet/flake  |
| 6093      | 2017           | SI | 8   | Sheet/flakes   |
| 6228      | 2017           | SI | 3   | Sheet/flakes   |
| 6368      | 1992           | SI |     | Sheet/flakes   |

**Figure C.3:** Overview of failures from 1284 m to the air cushion chamber, together with year of recorded failure and approximately size. Structurally controlled (SC), Stress induced (SI), weakness zone (WZ) and spalling (SP).

## Appendix D - Laboratory work

### Density and Sound velocity

**Table D.1:** Average diameter, length, weight, calculated density, traveltime and velocity for the quartzitic schist. The same specimen are used for the uniaxial compressive strength test.

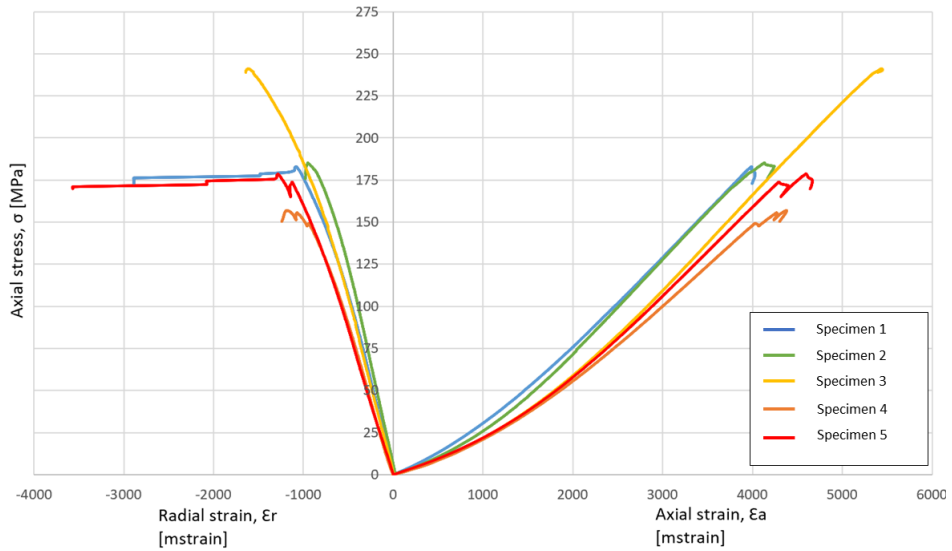
| Specimen number | Average Diameter [mm] | Length [mm] | Weight [g] | Density [g/cm <sup>3</sup> ] | Traveltime [ $\mu$ s] | Velocity [m/s] |
|-----------------|-----------------------|-------------|------------|------------------------------|-----------------------|----------------|
| Unsaturated     |                       |             |            |                              |                       |                |
| 1               | 40.56                 | 105.45      | 365.72     | 2.68                         | 23.9                  | 4412           |
| 2               | 40.52                 | 105.36      | 366.65     | 2.70                         | 26.8                  | 3931           |
| 3               | 40.52                 | 105.11      | 363.37     | 2.68                         | 22.9                  | 4590           |
| 4               | 40.52                 | 105.38      | 365.09     | 2.69                         | 25.4                  | 4149           |
| 5               | 40.47                 | 105.64      | 364.55     | 2.68                         | 24.9                  | 4243           |
| Water saturated |                       |             |            |                              |                       |                |
| 1               | 40.56                 | 105.45      | 366.20     | 2.69                         | 19.9                  | 5299           |
| 2               | 40.52                 | 105.36      | 367.12     | 2.70                         | 20.4                  | 5165           |
| 3               | 40.52                 | 105.11      | 363.78     | 2.68                         | 19.9                  | 5282           |
| 4               | 40.52                 | 105.38      | 365.62     | 2.69                         | 20.9                  | 5042           |
| 5               | 40.47                 | 105.64      | 365.01     | 2.69                         | 20.4                  | 5178           |

**Table D.2:** Average diameter, length, weight, calculated density, traveltime and velocity for the trondhjemite. The same specimen are used for the uniaxial compressive strength test.

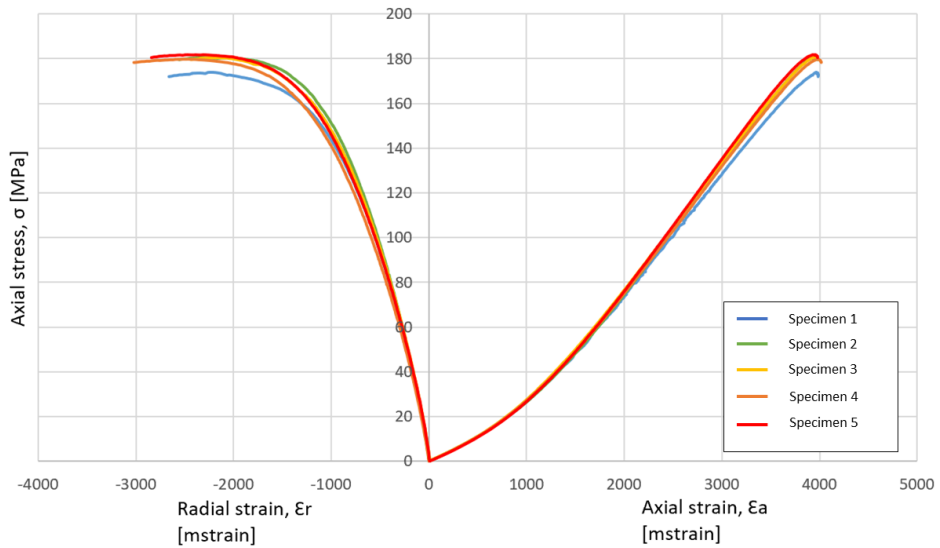
| Specimen number | Average Diameter [mm] | Length [mm] | Weight [g] | Density [g/cm <sup>3</sup> ] | Traveltime [ $\mu$ s] | Velocity [m/s] |
|-----------------|-----------------------|-------------|------------|------------------------------|-----------------------|----------------|
| Unsaturated     |                       |             |            |                              |                       |                |
| 1               | 40.55                 | 105.69      | 356.74     | 2.61                         | 29.9                  | 3535           |
| 2               | 40.55                 | 105.68      | 357.33     | 2.62                         | 30.3                  | 3488           |
| 3               | 40.57                 | 105.66      | 357.98     | 2.62                         | 29.9                  | 3534           |
| 4               | 40.53                 | 105.00      | 354.15     | 2.61                         | 29.4                  | 3571           |
| 5               | 40.57                 | 105.08      | 355.11     | 2.61                         | 30.3                  | 3468           |
| Water saturated |                       |             |            |                              |                       |                |
| 1               | 40.55                 | 105.69      | 357.77     | 2.62                         | 20.4                  | 5181           |
| 2               | 40.55                 | 105.68      | 358.35     | 2.63                         | 19.9                  | 5311           |
| 3               | 40.57                 | 105.66      | 358.99     | 2.63                         | 19.9                  | 5310           |
| 4               | 40.53                 | 105.00      | 355.21     | 2.62                         | 19.9                  | 5276           |
| 5               | 40.57                 | 105.08      | 356.09     | 2.62                         | 19.9                  | 5280           |

---

## Uniaxial compression test



**Figure D.1:** Stress-strain curves from uniaxial compression test for quartzitic schist.



**Figure D.2:** Stress-strain curves from uniaxial compression test for rondhjemite

---

**Table D.3:** Results from Uniaxial compression test performed on quartzitic schist 09.11.2018. At Rock Mechanics Laboratory, NTNU, Trondheim.

| <b>Specimen</b> | <b>UCS<br/>[MPa]</b> | <b>Young's modulus<br/>[GPa]</b> | <b>Poisson's ratio</b> | <b>Tagent Point<br/>[MPa]</b> |
|-----------------|----------------------|----------------------------------|------------------------|-------------------------------|
| 1               | 182.9                | 52.2                             | 0.27                   | 91.7                          |
| 2               | 185.3                | 55.8                             | 0.24                   | 93.4                          |
| 3               | 240.9                | 56.2                             | 0.31                   | 120.9                         |
| 4               | 156.8                | 44.7                             | 0.25                   | 78.8                          |
| 5               | 178.6                | 49.8                             | 0.25                   | 90.2                          |

**Table D.4:** Results from Uniaxial compression test performed on trondhemite 26.11.2018. At Rock Mechanics Laboratory, NTNU, Trondheim. Specimen 1 was tested 09.11.2018 together with the quartzitic schist.

| <b>Specimen</b> | <b>UCS<br/>[MPa]</b> | <b>Young's modulus<br/>[GPa]</b> | <b>Poisson's ratio</b> | <b>Tagent Point<br/>[MPa]</b> |
|-----------------|----------------------|----------------------------------|------------------------|-------------------------------|
| 1               | 174.0                | 56.2                             | 0.40                   | 87.2                          |
| 2               | 180.4                | 58.0                             | 0.39                   | 90.3                          |
| 3               | 180.5                | 56.8                             | 0.4                    | 90.4                          |
| 4               | 179.8                | 56.1                             | 0.44                   | 90.3                          |
| 5               | 181.7                | 58.6                             | 0.43                   | 91.5                          |

## Point load test

**Table D.5:** Results from Point Load Test performed on quartzitic schist 16.11.2018. At Rock Mechanics Laboratory, NTNU, Trondheim.

| SpecimenID | Diametral or axial | Width [mm] | Diameter [mm] | Load, P [kN] | $D_e^2$ [mm <sup>2</sup> ] | $I_s$ | F    | $I_s(50)$ | Comment   |
|------------|--------------------|------------|---------------|--------------|----------------------------|-------|------|-----------|-----------|
| 1          | D                  |            | 40.5          | 5,79         | 1640,25                    | 3,53  | 0,91 | 3,21      |           |
| 2          | D                  |            | 40.5          | 11,64        | 1640,25                    | 7,10  | 0,91 | 6,45      |           |
| 3          | D                  |            | 40.5          | 6,22         | 1640,25                    | 3,79  | 0,91 | 3,45      |           |
| 4          | D                  |            | 40.5          | 9,34         | 1640,25                    | 5,69  | 0,91 | 5,18      |           |
| 5          | D                  |            | 40.5          | 6,12         | 1640,25                    | 3,73  | 0,91 | 3,39      |           |
| 6          | D                  |            | 40.5          | 6,38         | 1640,25                    | 3,89  | 0,91 | 3,54      |           |
| 7          | D                  |            | 40.5          | 8,41         | 1640,25                    | 5,13  | 0,91 | 4,66      |           |
| 8          | D                  |            | 40.5          | 7,83         | 1640,25                    | 4,77  | 0,91 | 4,34      |           |
| 9          | D                  |            | 40.5          | 8,18         | 1640,25                    | 4,99  | 0,91 | 4,54      |           |
| 10         | D                  |            | 40.5          | 8,04         | 1640,25                    | 4,90  | 0,91 | 4,46      |           |
| 11         | D                  |            | 40.5          | 8,18         | 1640,25                    | 4,99  | 0,91 | 4,54      |           |
| 12         | D                  |            | 40.5          | 9,11         | 1640,25                    | 5,55  | 0,91 | 5,05      |           |
| 13         | D                  |            | 40.5          | 7,12         | 1640,25                    | 4,34  | 0,91 | 3,95      |           |
| 14         | D                  |            | 40.5          | 7,79         | 1640,25                    | 4,75  | 0,91 | 4,32      |           |
| 15         | D                  |            | 40.5          | 9,5          | 1640,25                    | 5,79  | 0,91 | 5,27      |           |
| 16         | D                  |            | 40.5          | 12,33        | 1640,25                    | 7,52  | 0,91 | 6,84      |           |
| 17         | D                  |            | 40.5          | 7,06         | 1640,25                    | 4,30  | 0,91 | 3,91      |           |
| 18         | D                  |            | 40.5          | 6,21         | 1640,25                    | 3,79  | 0,91 | 3,44      |           |
| 19         | A                  | 40.5       | 27.79         | 10.26        | 1433.02                    | 7.16  | 0.88 | 6.32      |           |
| 20         | A                  | 40.5       | 20.57         | 13.18        | 1060.72                    | 12.43 | 0.82 | 10.25     |           |
| 21         | A                  | 40.5       | 23.94         | 13.45        | 1234.49                    | 10.90 | 0.85 | 9.30      |           |
| 22         | A                  | 40.5       | 31.6          | 22.37        | 1629.49                    | 13.73 | 0.91 | 12.47     |           |
| 23         | A                  | 40.5       | 20.38         | 15.12        | 1050.92                    | 14.39 | 0.82 | 11.84     |           |
| 24         | A                  | 40.5       | 24.66         | 14.82        | 1271.62                    | 11.65 | 0.86 | 10.01     |           |
| 25         | A                  | 40.5       | 24.05         | 16.72        | 1240.17                    | 13.48 | 0.85 | 11.51     |           |
| 26         | A                  | 40.5       | 23.77         | 19.21        | 1225.73                    | 15.67 | 0.85 | 13.35     |           |
| 27         | A                  | 40.5       | 28.43         | 19.76        | 1466.03                    | 13.48 | 0.89 | 11.95     |           |
| 28         | A                  | 40.5       | 24.82         | 22.02        | 1279.87                    | 17.20 | 0.86 | 14.80     |           |
| 29         | A                  | 40.5       | 21.15         | 16.03        | 1090.63                    | 14.70 | 0.83 | 12.20     |           |
| 30         | A                  | 40.5       | 25.1          | 17.36        | 1294.31                    | 13.41 | 0.86 | 11.57     |           |
| 31         | A                  | 40.5       | 24.52         | 17.38        | 1264.40                    | 13.75 | 0.86 | 11.79     |           |
| 32         | A                  | 40.5       | 27.38         | 18.77        | 1411.88                    | 13.29 | 0.88 | 11.69     |           |
| 33         | A                  | 40.5       | 22.07         | 15.19        | 1138.07                    | 13.35 | 0.84 | 11.18     |           |
| 34         | A                  | 40.5       | 27.19         | 14.84        | 1402.09                    | 10.58 | 0.88 | 9.29      |           |
| 35         | A                  | 40.5       | 29.43         | 12.12        | 1517.59                    | 7.99  | 0.89 | 7.14      |           |
| 36         | A                  | 40.5       | 25.13         | 19.71        | 1295.86                    | 15.21 | 0.86 | 13.12     |           |
| 37         | A                  | 40.5       | 24.55         | 16.49        | 1265.95                    | 13.03 | 0.86 | 11.18     |           |
| 38         | A                  | 40.5       | 29.96         | 13.9         | 1544.92                    | 9.00  | 0.90 | 8.07      |           |
| 39         | A                  | 40.5       | 23.82         | 19.92        | 1228.31                    | 16.22 | 0.85 | 13.82     |           |
| 40         | A                  | 40.5       | 22.69         | 18.99        | 1170.04                    | 16,23 | 0.84 | 13.68     |           |
| 41         | A                  | 40.5       | 26.01         | 21.8         | 1344.85                    | 16,21 | 0.87 | 14.10     | not valid |
| 42         | A                  | 40.5       | 21.91         | 16.42        | 1129.82                    | 14,53 | 0.84 | 12.16     | not valid |
| 43         | A                  | 40.5       | 25.65         | 19.64        | 1322.67                    | 14,85 | 0.87 | 12.87     |           |
| 44         | A                  | 40.5       | 27.12         | 18.44        | 1398.48                    | 13,19 | 0.88 | 11.57     | not valid |

---

## Brazil test

**Table D.6:** Results from Brazil test performed on quartzitic schist 16.11.2018. Rock Mechanics Laboratory, NTNU, Trondheim. specimen 7 was not valid due to shear failure.

| Sample nr. | Diameter [mm] | Thickness [kN] | Load, P [kN] | $\sigma_t$ [MPa] |
|------------|---------------|----------------|--------------|------------------|
| 1          | 50.61         | 25.17          | 28.44        | 14.2             |
| 2          | 50.51         | 25.44          | 37.9         | 18.8             |
| 3          | 50.53         | 25.54          | 52.57        | 25.9             |
| 4          | 50.6          | 23.86          | 45.02        | 23.7             |
| 5          | 50.48         | 25.31          | 29.65        | 14.8             |
| 6          | 50.5          | 25.2           | 45.2         | 22.6             |
| 7          | 50.42         | 25.03          | 30.42        | 15.3             |
| 8          | 50.55         | 24.53          | 33.22        | 17.0             |
| 9          | 50.63         | 25.32          | 35.05        | 17.4             |
| 10         | 50.61         | 25.57          | 35.73        | 17.6             |
| 11         | 50.51         | 24.31          | 40.89        | 21.2             |
| 12         | 50.46         | 25.12          | 48.19        | 24.2             |
| 13         | 50.49         | 24.73          | 52.04        | 26.5             |
| 14         | 50.55         | 24.61          | 38.14        | 19.5             |
| 15         | 50.56         | 25.48          | 47.59        | 23.5             |
| 16         | 50.64         | 24.34          | 42.17        | 21.8             |

**Table D.7:** Results from Brazil test performed on trondhjemite 19.11.2018. Rock Mechanics Laboratory, NTNU, Trondheim. specimen 2 was not valid due to shear failure.

| Sample nr. | Diameter [mm] | Thickness [mm] | Load, P [kN] | $\sigma_t$ [MPa] |
|------------|---------------|----------------|--------------|------------------|
| 1          | 50,73         | 25,07          | 19,65        | 9,8              |
| 2          | 50.8          | 25.44          | 20.85        | 10.3             |
| 3          | 50.76         | 25.40          | 22.38        | 11.0             |
| 4          | 50.77         | 25.14          | 19.79        | 9.9              |
| 5          | 50.66         | 24.55          | 22.23        | 11.4             |
| 6          | 50.73         | 25.22          | 18.63        | 9.3              |
| 7          | 50.77         | 25.33          | 18.71        | 9.3              |
| 8          | 50.72         | 25.14          | 16.72        | 8.3              |
| 9          | 50.84         | 25.34          | 19.83        | 9.8              |
| 10         | 50.69         | 25.4           | 21.77        | 10.8             |
| 11         | 50.77         | 25.51          | 14.58        | 7.2              |
| 12         | 50.76         | 25.42          | 20.05        | 9.9              |
| 13         | 50.75         | 25.00          | 21.59        | 10.8             |
| 14         | 50.77         | 25.68          | 19.62        | 9.6              |
| 15         | 50.8          | 24.98          | 21.98        | 11.0             |

## Tilt test

**Table D.8:** Results from tilt testing performed on quartzitic schist, 9.11.2018 at Rock Mechanics Laboratory, NTNU, Trondheim. Repetitions with the sign - was not performed. Moisture content W, 37,7 and temperature T, 21 degrees.

| Specimen        |            | 3                |                 | 4                |                 | 5                |                 |
|-----------------|------------|------------------|-----------------|------------------|-----------------|------------------|-----------------|
| Repetition<br>i | side/plane | $\beta_i$<br>[°] | $\phi_b$<br>[°] | $\beta_i$<br>[°] | $\phi_b$<br>[°] | $\beta_i$<br>[°] | $\phi_b$<br>[°] |
| 1               | 1          | 31.0             | 27.5            | 29.5             | 26.1            | 31.3             | 27.8            |
| 2               | 1          | 30.9             | 27.4            | 27.9             | 24.6            | 31.0             | 27.5            |
| 3               | 1          | 28.6             | 25.3            | 26.8             | 23.6            | 31.3             | 27.8            |
| 4               | 1          | 28.8             | 25.5            | -                | -               | -                | -               |
| 5               | 2          | 29.6             | 26.2            | 31.9             | 28.3            | 30.1             | 26.7            |
| 6               | 2          | 27.6             | 24.4            | 29.2             | 25.8            | 29.3             | 25.9            |
| 7               | 2          | 29.1             | 25.7            | 31.2             | 27.7            | 29.6             | 26.2            |
| 8               | 3          | 29.8             | 26.4            | 32.3             | 28.7            | 32.4             | 28.8            |
| 9               | 3          | 30.3             | 26.8            | 30.7             | 27.2            | 29.9             | 26.5            |
| 10              | 3          | 28.6             | 25.3            | 30.6             | 27.1            | 29.6             | 26.2            |
| 11              | 3          | -                | 29.7            | 26.3             | 28.8            | 25.5             | -               |
| 12              | 4          | 28,4             | 25,1            | 33.0             | 29.4            | 30.1             | 26.7            |
| 13              | 4          | 28,9             | 25,6            | 33.6             | 29.9            | 29.6             | 26.2            |
| 14              | 4          | 29,1             | 25,7            | 33.0             | 27.5            | 28.3             | 25.0            |
| 15              | 4          | -                | -               | 32.4             | 28.8            | 27.5             | 24.3            |

**Table D.9:** Results from tilt testing performed on trondhjemite, 9.11.2018 at Rock Mechanics Laboratory, NTNU, Trondheim. Repetitions with the sign - was not performed. Moisture content W, 37,7 and temperature T, 21 degrees.

| Specimen        |            | 3                |                 | 4                |                 | 5                |                 |
|-----------------|------------|------------------|-----------------|------------------|-----------------|------------------|-----------------|
| Repetition<br>i | side/plane | $\beta_i$<br>[°] | $\phi_b$<br>[°] | $\beta_i$<br>[°] | $\phi_b$<br>[°] | $\beta_i$<br>[°] | $\phi_b$<br>[°] |
| 1               | 1          | 31.5             | 28.0            | 34.5             | 30.8            | 34.9             | 31.1            |
| 2               | 1          | 34.2             | 30.5            | 33.2             | 29.5            | 32.3             | 28.7            |
| 3               | 1          | 33.9             | 30.2            | 32.4             | 28.8            | 32               | 28.4            |
| 4               | 1          | 33.4             | 29.7            | -                | -               | -                | -               |
| 5               | 2          | 33.3             | 29.6            | 34.2             | 30.5            | 33.2             | 29.5            |
| 6               | 2          | 32.5             | 28.9            | 32.9             | 29.3            | 30.5             | 27.0            |
| 7               | 2          | 33.2             | 29.5            | 33.9             | 30.2            | 32.5             | 28.9            |
| 8               | 3          | 32.6             | 29.0            | 32.2             | 28.6            | 32.2             | 28.6            |
| 9               | 3          | 32.9             | 29.3            | 32.9             | 29.3            | 32.6             | 29.0            |
| 10              | 3          | 33.6             | 29.9            | 33.1             | 29.4            | 31.3             | 27.8            |
| 11              | 4          | 31.3             | 27.8            | 32.3             | 28.7            | 31.4             | 27.9            |
| 12              | 4          | 32.4             | 28.8            | 32.7             | 29.1            | 31.9             | 28.3            |
| 13              | 4          | 33.7             | 30.0            | 31.2             | 27.7            | 31.7             | 28.1            |



XRD

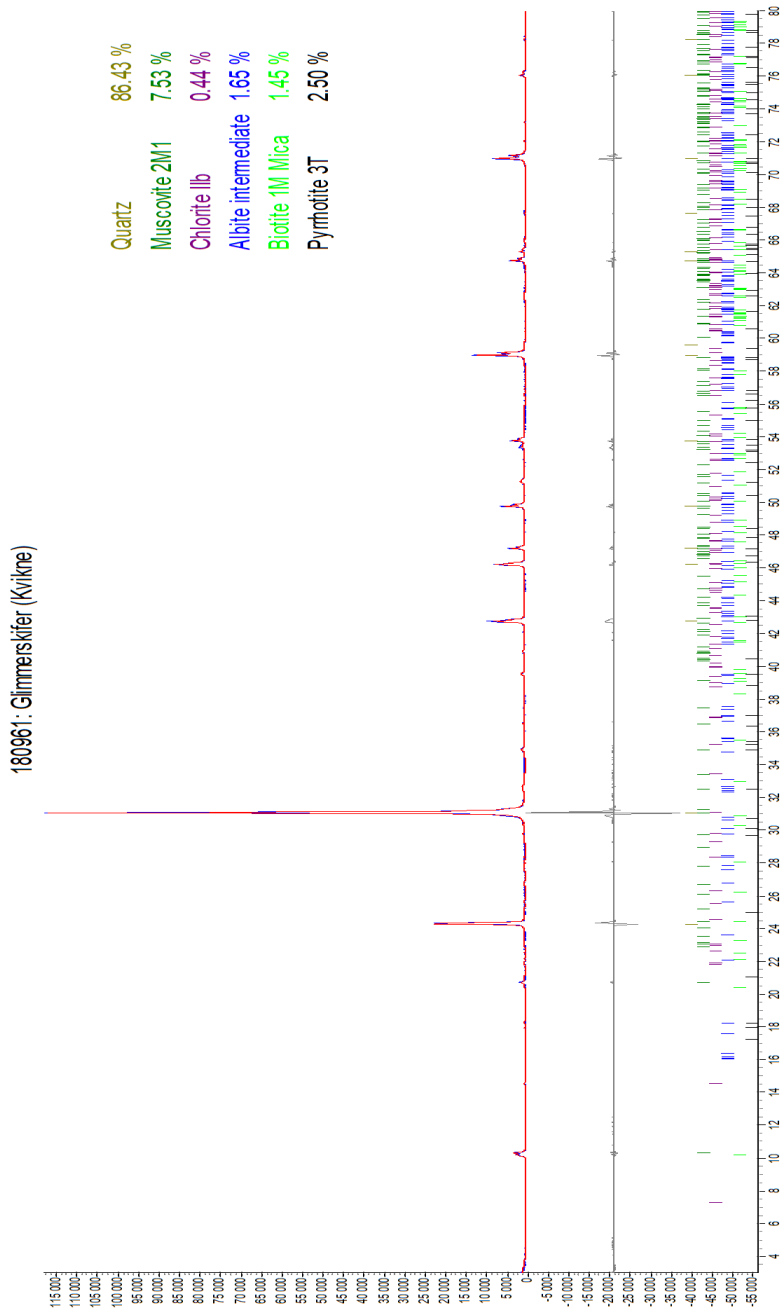


Figure D.3: X-ray diffraction results for quartzitic schist, performed 27.11.2018

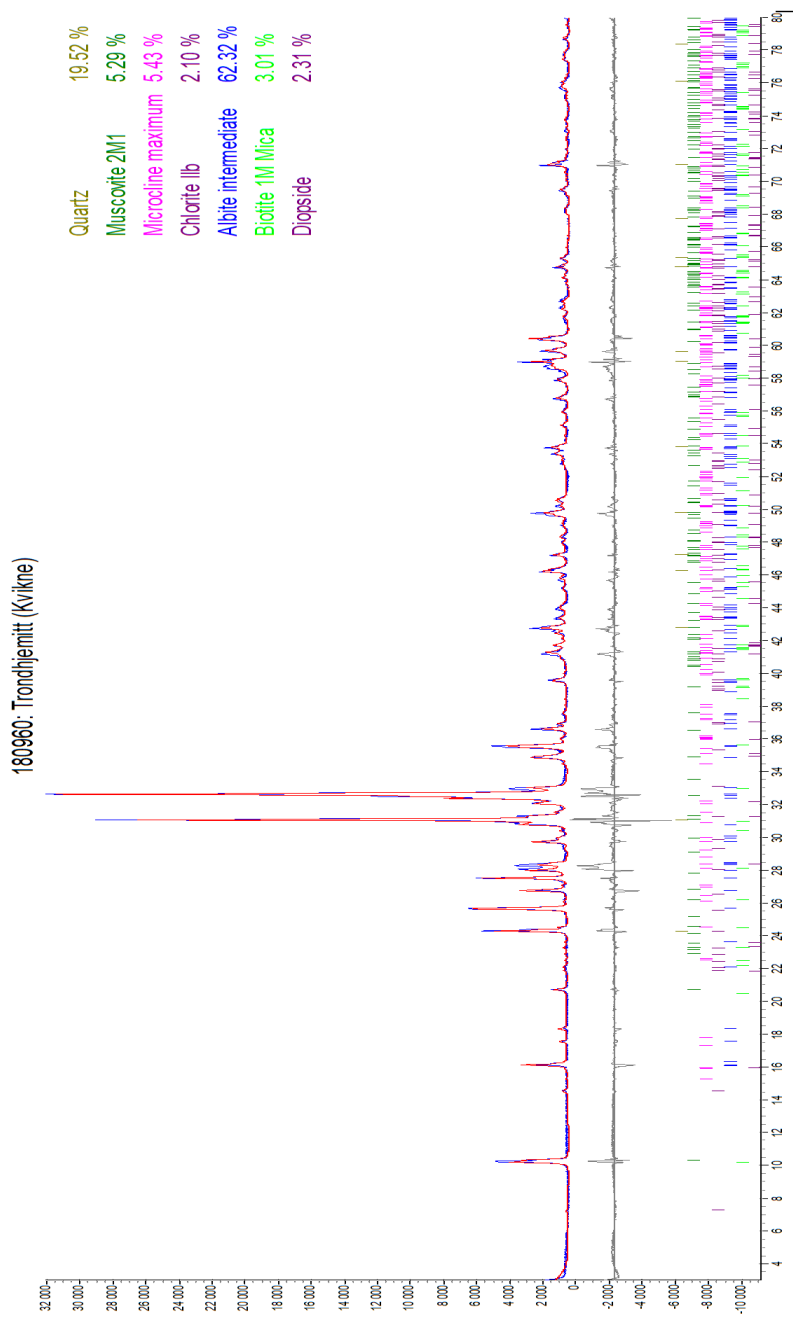
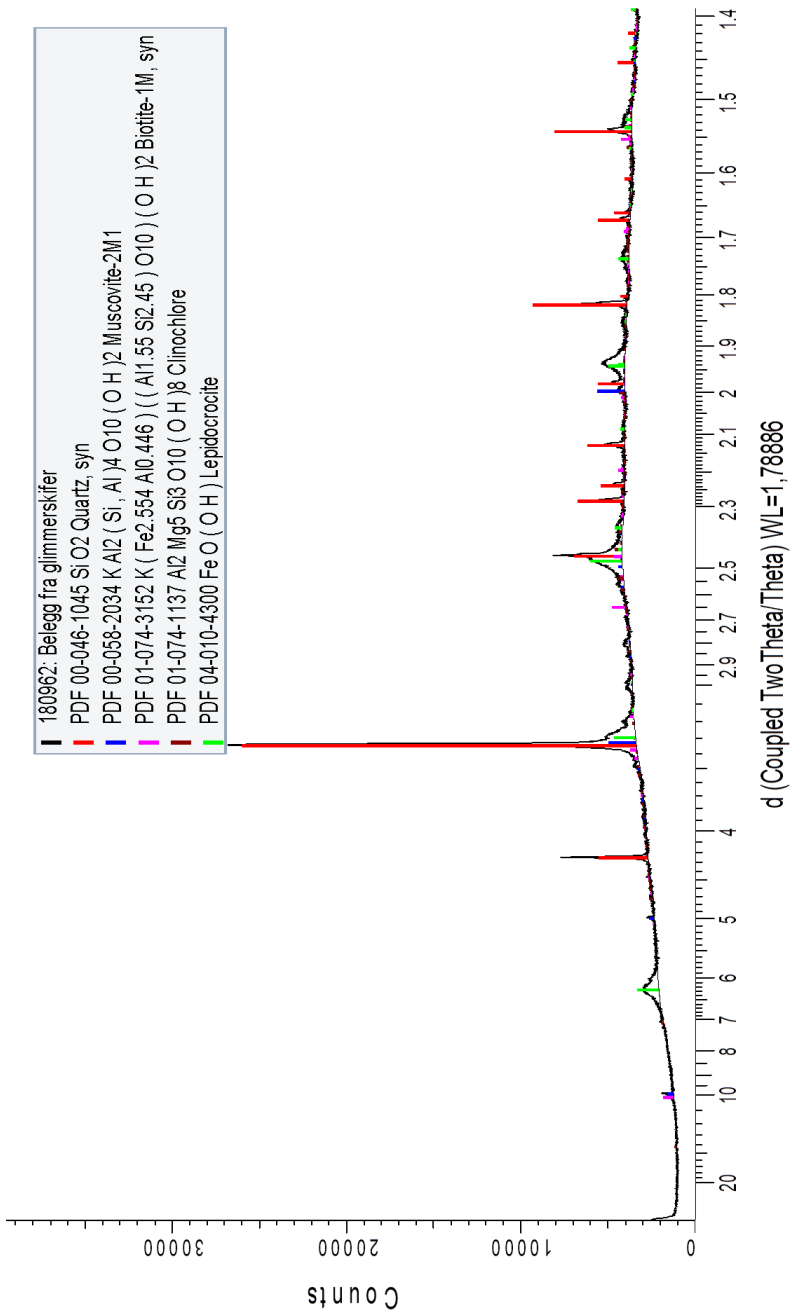


Figure D.4: X-ray diffraction results for Trondhemite, preformed 27.11.2018



**Figure D.5:** X-ray diffraction results for substance found in water after saturation of quartzitic schist, preformed 27.11.2018. The substance is believed to be the same coating/joint filling in the quartzitic schist.

